

Quantum Correlation Experiments with Resonance Fluorescence Photons of single Barium Ions

Dissertation

zur Erlangung des Doktorgrades an der
naturwissenschaftlichen Fakultät
der Leopold-Franzens-Universität Innsbruck

vorgelegt von

Mag. Sebastian Gerber

durchgeführt am Institut für Experimentalphysik
unter der Leitung von
Univ.-Prof. Dr. Rainer Blatt

Innsbruck
Juli 2010

Abstract

This thesis discusses a variety of fundamental quantum optics experiments characterizing a system of individually trapped barium ions interacting with continuous laser light. Such a system, as one of the basic conceptual models in physics in describing the interaction processes between light and matter, is perfectly suited to investigate the governing atomic dynamics. This task is performed by systematically analyze the intensity of the emitted resonance fluorescence and also by using correlation functions to infer the properties of the time-dependent field and intensity.

Paul traps are used to confine single $^{138}\text{Ba}^+$ ions, which are continuously laser cooled by two narrow-band light fields at 493 nm and 650 nm exciting the $S_{1/2} \leftrightarrow P_{1/2}$ and $P_{1/2} \leftrightarrow D_{3/2}$ dipole transitions, respectively. At the Doppler limit single ions are localized to a region of ~ 40 nm at the trap center. Scattered 493 nm photons are observed perpendicular to the laser excitation direction and investigated with either a single-photon counter, a Hanbury-Brown and Twiss setup or a CCD camera. The scattered fluorescence from the ion contains all of the information about the governing atom-light interaction dynamics. This information can be extracted via statistical analysis of the detected photocounts using correlation functions.

The thesis presented starts with an overview of the relevant level scheme of $^{138}\text{Ba}^+$ and discusses the interaction processes between a single ion and a coherent light field, using optical Bloch equations. This is followed by introducing the mathematical concepts of the different applied correlation functions. Starting with the properties and applications of the first- and second-order correlations, the concept of an intensity-field correlation function is established, which combines the techniques of a homodyne detector and an intensity correlator.

Subsequently, a series of experiments is described starting with a Hong-Ou-Mandel type experiment. Here the fluorescence of two ions, situated in two spatially separated traps, is superimposed on a 50:50 beam splitter and the degree of the photons indistinguishability is determined to be 89(2)%. This feature of the emitted photons constitutes an essential part for the implementation of entanglement protocols using atom-photon interfaces. Their indistinguishability demonstrates the setup's suitability for future processing of quantum information.

In a subsequent experiment an intensity-field correlation function is measured for the first time on a single-atom single-photon basis. With this correlation function it is possible to directly observe the time evolution of the source-field corresponding to a single resonance fluorescence photon following the initialization of the atom in its ground state.

In the final experiment a system consisting of an ion in front of a distant mirror equivalent to a half-cavity is investigated. Employing this Michelson-type interferometer the first order correlation of the emitted light field is recorded up to a delay

time of ~ 30 ns, revealing the temporal coherence of the fluorescence. Additionally, by adopting this half-cavity system for two trapped ions the fraction of the coherently scattered intensity in the atomic fluorescence is determined.

Zusammenfassung

In der vorliegenden Arbeit werden verschiedene fundamentale Quantenoptikexperimente vorgestellt und diskutiert, welche die Wechselwirkung zwischen einzelnen gefangenen Bariumionen und kontinuierlichem Laserlicht charakterisieren. Dieses System stellt eines der grundlegenden konzeptuellen Modelle in der Physik um das Zusammenspiel von Materie mit Licht zu beschreiben dar und eignet sich daher hervorragend zur Untersuchung der vorherrschenden atomaren Dynamik. Im Experiment wird diese Aufgabenstellung durch die systematische Analyse der beobachteten Intensität der Resonanzfluoreszenz durchgeführt, sowie durch die Bestimmung ihrer zeitabhängigen Eigenschaften mittels Korrelationsfunktionen.

Die Speicherung der $^{138}\text{Ba}^+$ Ionen erfolgt hierbei durch elektrodynamische Potentiale in Paul-Fallen. Lokalisiert auf eine Region von ~ 40 nm im Fallenzentrum werden die Ionen auf den beiden Dipolübergängen $S_{1/2} \leftrightarrow P_{1/2}$ und $P_{1/2} \leftrightarrow D_{3/2}$ durch zwei schmalbandige Lichtfelder bei 493 nm und 650 nm angeregt und kontinuierlich optisch gekühlt. Gestreute Photonen bei 493 nm werden im rechten Winkel zur Laserausbreitungsrichtung und parallel zur Quantisierungsachse, definiert durch ein angelegtes, schwaches Magnetfeld am Ort des Ions, aufgesammelt und auf eine CCD Kamera fokussiert. Alternativ hierzu kann das Fluoreszenzlicht in einem Hanbury-Brown und Twiss Detektor analysiert werden. Die gestreute Fluoreszenz beinhaltet dabei sämtliche Information über die vorherrschende Dynamik der Atom-Licht Wechselwirkung. Diese Information kann nun mittels einer statistischen Analyse des detektierten Photonenflusses extrahiert werden unter Anwendung von Korrelationsfunktionen.

Die dargelegte Arbeit beginnt mit einem Überblick des relevanten Termschemas von $^{138}\text{Ba}^+$ sowie mit einer Diskussion der vorliegenden Wechselwirkungsprozesse zwischen einem einzelnen Ion und einem kohärenten Laserfeld unter Verwendung optischer Bloch-Gleichungen. Diesem Teil folgt eine Einführung in die mathematischen Konzepte der verschiedenen verwendeten Korrelationsfunktionen. Beginnend mit den Eigenschaften und Anwendungen der in der Quantenoptik wichtigen Korrelationsfunktionen erster und zweiter Ordnung wird das Konzept der Intensitäts-Feld Korrelationsfunktion eingeführt, welche die Methoden eines Homodyndetektors mit dem eines Intensitätskorrelators kombiniert.

Eine Korrelationsfunktion zweiter Ordnung wird anschließend für die Charakterisierung eines Hong-Ou-Mandel Experimentes verwendet, in welchem die Fluoreszenz von zwei in unterschiedlichen Fallen befindlichen Ionen auf einen 50:50 Strahlteiler überlagert wird und ein Grad der Photonenununterscheidbarkeit von 89(2)% erreicht wird. Da diese Eigenschaft der emittierten Photonen eine wesentliche Grundlage für die Realisierung der meisten auf Atom-Photon Kopplung basierenden Verschränkungsprotokolle darstellt, demonstriert dieses Resultat die erfolgre-

iche Eignung des verwendeten Aufbaus hinsichtlich zukünftiger Verarbeitungen von Quanteninformation.

In einem weiteren Experiment wird die Realisierung der Intensitäts-Feld Korrelationsfunktion für den ersten gemessenen Fall einer Einzelphoton-Einzelatom Wechselwirkung präsentiert. Diese Korrelation liefert den direkten Aufschluss über die zeitliche Entwicklung des Quellfeldes eines einzelnen Resonanfluoreszenzphotons nach der Initialisierung des Atoms in seinem Grundzustand.

Die Verwendung eines "Halb-Resonatorsystems", bestehend aus einem gespeicherten Ion vor einem entfernten Spiegel, erlaubt im Weiteren die Messung der Korrelationsfunktion erster Ordnung bis zu einer Verzögerungszeit des gestreuten Lichtfeldes von ~ 30 ns. Mit diesem Michelson-Typ Interferometer lassen sich anschließend die Kohärenzeigenschaften der emittierten Fluoreszenz ableiten. Die Anpassung dieses Aufbaus für zwei gespeicherte Ionen ermöglicht es zudem den kohärent gestreuten Anteil der Intensität der atomaren Fluoreszenz zu bestimmen.

Contents

1	Introduction	3
2	Light-matter interaction	7
2.1	The Ba ⁺ ion	7
2.1.1	The level scheme	7
2.1.2	The Zeeman splitting	8
2.2	The Bloch equations	10
2.2.1	The three-level system	10
2.2.2	The eight-level system	16
3	Correlation functions	21
3.1	First-order correlation function	22
3.1.1	First order coherence and spectrum of a two-level system	23
3.1.2	Elastic and inelastic scattering	26
3.1.3	$g^{(1)}(\tau)$ -function of an ion	28
3.2	Second-order correlation function	30
3.2.1	Second-order coherence of a two-level system	32
3.2.2	$g^{(2)}(\tau)$ -function of an ion	32
3.3	Intensity-field correlation function	34
4	Trapping of single atoms	39
4.1	The Paul-trap	39
4.1.1	The linear Paul trap	41
4.1.2	The ring Paul trap	42
5	Experimental setup and operation	45
5.1	Vacuum setup	45
5.1.1	The linear trap	46
5.1.2	The ring trap	50
5.2	Laser setup	53
5.2.1	Laser system	53

5.2.2	Light detection methods	54
5.3	Experimental routines	57
5.3.1	Trap loading	58
5.3.2	Compensation of micromotion	58
5.3.3	Laser cooling	60
5.3.4	Spectra of a trapped ion	62
5.3.5	Calibration of the setup	64
6	Two photon interference	67
6.1	Interference at a beam splitter	68
6.1.1	Classical and quantum description of a beam splitter	68
6.1.2	Quantum interference and HOM-dip	71
6.2	Two photon interference between two remotely trapped ions	73
6.2.1	Experimental setup	74
6.2.2	Theoretical model	75
6.2.3	Experimental results	77
7	Intensity-field correlation	83
7.1	Experimental setup	84
7.2	The model	85
7.3	Experimental results	89
8	Interference of fluorescence in a half cavity	95
8.1	Half cavity setup	96
8.2	Visualization of sidebands	100
8.3	First order correlation measurement	102
8.4	Two ions in front of a mirror	109
9	Summary and Outlook	115
	Bibliography	119

Chapter 1

Introduction

The interaction between light and matter is fundamental for many phenomena in our environment from the light emitted by the sun to the application of modern TFT displays. Hence, its study constitutes one of the core interests for investigations of natural science since its beginnings. Throughout the last century the understanding of the involved mechanisms received a great enrichment with the revealing of the electronic structure of atoms and the nature of light as a quantum mechanical light field. Hereby, the developed theoretical frameworks describing the interaction processes and their verification in experiments forms the area of quantum optics.

The starting point of systematic studies of atomic interactions with light was initialized nearly two centuries ago with the discovery of dark lines in the solar spectrum by Fraunhofer in 1817 [1] and their interpretation by Bunsen and Kirchhoff in 1863 [2] leading to the new field of spectroscopy of atoms and molecules. The investigation of light absorbed or emitted by atoms herewith provided and still provides an essential source of information on the dynamics of the involved systems. In an interplay of experiment and theory the physical picture of matter and light then solidified with a substantial progress throughout the beginning of the last century.

For light the fundamental concept of a propagating electromagnetic wave without the need of a carrier medium was already paved by Maxwell in 1873 [3] and can be observed inter alia in the famous double-slit experiment. In the late 19th century however contradictions arose between the wave theory of light and measurements of the electromagnetic spectrum emitted by thermal radiators. The theoretical solution describing this black-body radiation was then found by Planck in 1900 [4] introducing a quantized model of the emitted light energy. Later, the notion of the wave-particle duality was established, observable in the photoelectric effect described by Einstein in 1905 and in scattering effects like Compton scattering. This was theoretically formulated by Dirac by applying a field quantization to light in the 1920s and later by Feynman in the 1940s.

For the case of matter its wave aspect was first proposed by de Broglie in 1924. The quantum mechanical picture then formed with Pauli asserting the exclusion and uncertainty principle in 1925 and with Schrödinger developing the wave equation for

matter in 1926, and in 1928 Dirac extended the formalism for to treat relativistic particles.

The quantum description of the atom in the form of a shell model led then to a first understanding of line spectra investigated by Bohr in 1913 [5] on sodium vapor. He first postulated based on Planck's work, that the spectral lines originate from quantum jumps between the atomic energy states with the energy differences being emitted as packets of light. Einstein then implied in a rate-equation model of the energy exchange between light and a black-body, that these light packets, which were later called photons, can be absorbed and spontaneously or stimulated emitted by atoms. It was then the use of the stimulated emission process of light from a ruby crystal implemented by Maiman et al. [6] in 1960 that founded the laser, being today the most frequently used device in quantum optics experiments.

Since that time resonance fluorescence of laser excited atoms is routinely used as a tool to simply detect atoms, for spectroscopical applications, and its quadrature components have been used to create squeezed states and nonclassical states of light. In short, the observation of resonance fluorescence has become a technology ubiquitous in quantum physics.

To study these interaction phenomena between light and matter one of the most fundamental system comprises of a single atom isolated from the environment at rest interacting with a single photon. Experimentalists' attempts to realize such a model have succeeded in 1980 with the work of Neuhauser et al. [7] by confining single barium ions inside a Paul trap [8]. This experiment was then followed by one of Wineland and Itano [9] reporting on magnesium ions trapped in a Penning trap. Addressed with laser light the ions could be optically cooled to the ground state of the harmonic trap and thus localized within a few nanometers, which method was first proposed by Wineland et al. [10]. Since then, the fluorescence of single-ions has progressed to be an ideal system to investigate fundamental concepts in quantum optics.

With the rapid advance in quantum mechanics and computational science the new field of quantum computation and quantum information science arose contributed by Feynman [11] and Benioff [12] in the 1980s. To perform quantum computation with trapped ions was then proposed by Cirac and Zoller [13] in 1995. In this concept ions form static quantum bits that can interact with each other via phonons or as later proposed in [14] using a photonic channel for transmitting quantum states. Since then single trapped ions are considered as one of the most promising candidates for processing of quantum information due to the accessible control of both the internal atomic states and the external motional states of the ion. Trapped ions offer long coherence times for information storage [15], are easily manipulated coherently, and their Coulomb interaction can be utilized to realize quantum logic gates [16, 17]. Furthermore, single photons are well suited for transmitting quantum information

over long distances [18, 19]. Recently, several experiments have addressed the realization of a probabilistic entanglement [20–22] and of an atom-photon interface with single atoms [23–25].

It is hence the complete understanding and control of the internal dynamics of a trapped ion that permits one to characterize the interaction between matter and light on a quantum level. Especially, the time-evolution of the electronic states of a laser-excited atom imply all the information of the present interaction processes. This information is then encoded in the statistics of the scattered light field from the atom and can be accessed by a statistical analysis of the photocurrent. This method was first realized in 1956 by Hanbury Brown and Twiss by statistical measurements of photons emitted by spatially coherent light [26] and star light [27] marking the beginning of systematic studies of fluctuations of light. In these experiments they recorded correlation functions of light intensities and could retrieve in the case of star light its spatial coherence and thus determine the angular diameter of the star. Later in 1977 Kimble et al. [28] showed the first intensity correlation function from the fluorescence radiated by distinct atoms followed by an experiment performed by Short et al. in 1983 [29]. Here, Short et al. reported the first nonclassical photon statistics indicating the radiation of a single atom. Since that time, the intensity correlation function, or second-order correlation function $g^{(2)}(\tau)$, from an atom still proves to be a valuable tool to reveal its dynamics of light interaction. In particular, the $g^{(2)}(\tau)$ describes the probability of detecting a photon at time τ , given that a second photon was detected at time $\tau = 0$, and thus directly maps the temporal evolution of the excited state population of the monitored atom. Another basic type of correlation function is the field or first-order correlation function $g^{(1)}(\tau)$. It enables one to measure the temporal coherence of the light ray and was first observed with an interferometer by Michelson and Morley in an experiment to show the constancy of the speed of light in 1887 [30]. Based on this idea of combining a light field with a copy of itself, being delayed by a time τ , in 2001, Eschner et al. [31] used a setup constituting of a single trapped ion under laser excitation in front a distant mirror to record the shape of the first order autocorrelation of the emitted fluorescence for nanometer changes of the ion’s position in front the mirror. With an ion being part of the light interferometer they could further retrieve the motional information of the ion wave packet oscillating inside the trapping potential.

Combining the techniques of an intensity correlation with a homodyne detector gave then access to another type of correlation function, which is able to directly reveal the time evolution of the polarization of a laser-excited atom, starting from the ground state. As this method constitutes a correlation between an intensity and a field measurement it was named $g^{(1.5)}(\tau)$. This quantity was first investigated by Orozco along with Carmichael et al. in 2000 [32, 33] with optically pumped rubidium atoms traversing through a high-finesse cavity, where the field emitted out of the

cavity corresponded to only a fraction of a photon excitation on average.

In this thesis several fundamental quantum optics experiments described the system of single trapped ions under continuous laser excitation. The experimental methods discussed in this manuscript are based on the analysis of intensity and field correlation functions extracted from the resonance fluorescence of single Ba^+ ions. Additionally, the fundamental quest of recording the first intensity-field correlation function at the single-atom single-photon level was approached. Further, investigations towards the realization of entanglement protocols in quantum networks were performed, where the photon indistinguishability between two independently trapped ions was measured using a Hong-Ou-Mandel type quantum interference at a beam splitter [34].

The thesis is organized as follows: In chapter 2 the atomic structure of $^{138}\text{Ba}^+$ is introduced as well as the relevant interaction processes between a single ion and a coherent light field. The mathematical description of this interaction is formulated in terms of optical Bloch equations. In chapter 3 the theoretical concepts of the employed correlation functions of different orders are first discussed for distinct types of light sources and then presented for an atomic two-level system together with the extension to the realistic atomic level structure of Ba^+ . Chapter 4 discusses the operation principle of a Paul trap for the laboratory situations of a linear and a ring trap design. In chapter 5 the experimental laboratory equipment, i.e. the laser systems and the trap apparatuses, are described and their basic methodologies for daily operation are discussed with a detailed description of the loading process, the compensation of micromotion and the laser cooling technique. In chapter 6 the two-photon interference at a beam splitter from two remotely trapped ions is presented. Chapter 7 describes the measurement of the intensity-field correlation of the resonance fluorescence of a single ion, where the real and imaginary contributions of the correlation function are extracted. Chapter 8 investigates the system of single ions located in front of a distant mirror introduced in [31]. The first-order correlation of the resonance fluorescence is measured for large mirror distances deducing the coherence properties of the fluorescence light. Furthermore, the experiment is repeated for two ions situated in one trap interacting over the mirror channel. Finally, in chapter 9 the results are summarized and an outlook for future experiments is given.

Chapter 2

Light-matter interaction

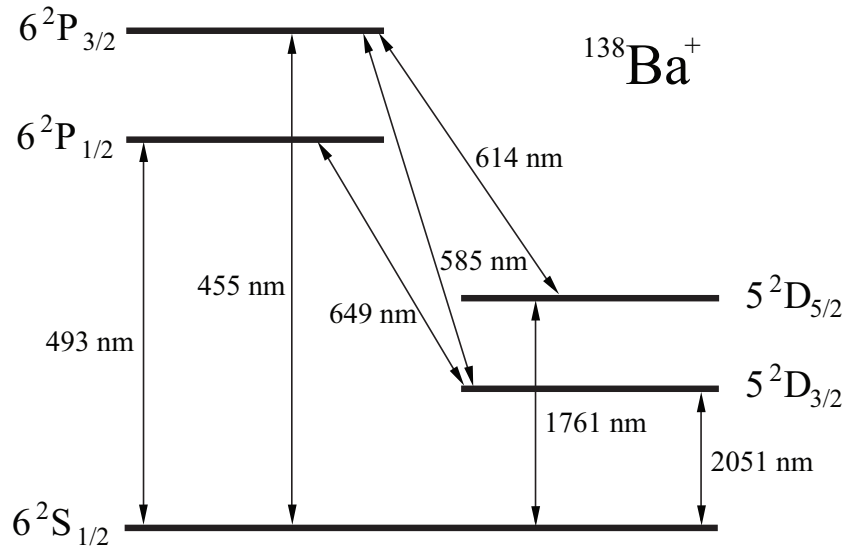
Collecting and recording resonance fluorescence of a laser-excited ion forms the basis for all presented experiments. In particular we use barium ions, for which level scheme and principle physical characteristics are introduced in the beginning of this chapter. This section is followed by a discussion of the interaction process of a single ion with a coherent laser field. Here we apply optical Bloch equations first with a simplified three level system and finally with an extended and more realistic eight-level model. A similar analysis of this problem can be found in [35].

2.1 The Ba^+ ion

For all performed measurements single ionized barium atoms are utilized. In the following we introduce the relevant electronic level scheme of Ba^+ and discuss the Zeeman effect that splits the degeneracy of the associated levels in the experiment.

2.1.1 The level scheme

The element barium is a silvery metal and belongs to the earth-alkaline group. In nature barium's natural occurrence constitutes of a mixture of seven stable isotopes indicated in Table 2.1.1, where the most common isotope, ^{138}Ba , is employed in the experiments. Since this isotope has a nuclear spin of zero we observe no hyperfine splitting in the spectra. When barium is singly ionized, the electron configuration yields an alkaline-like structure with a single s -valence electron with an electronic configuration $[\text{Xe}]6s^1\ ^2S_{1/2}$. The lowest electronic states are shown in Fig. 2.1, where for laser cooling the transition $S_{1/2} \leftrightarrow P_{1/2}$ is used. Since the $P_{1/2}$ level can additionally decay in one out of four cases into the metastable $D_{3/2}$ state, a second re-pumping laser is required. Hence, we are left with two dipole transitions lying both in the visible range, which form a Λ -system. Their exact wavelengths and the natural linewidths are presented in Table 2.1.1.

Figure 2.1: Lowest electronic levels of a $^{138}\text{Ba}^+$ -ion [36].

Element		^{130}Ba	^{132}Ba	^{134}Ba	^{135}Ba	^{136}Ba	^{137}Ba	^{138}Ba
abundance	%	0.1	0.1	2.4	6.6	7.3	11.3	71.7
nuclear spin I	\hbar	0	0	0	3/2	0	3/2	0

Table 2.1: Barium isotopes, their nuclear spin and natural abundance [36, 37].

2.1.2 The Zeeman splitting

To describe the experimental results we have to consider the Zeeman effect. In all experiments a weak magnetic field is applied at the position of the ion that splits up the degeneracy of the atomic levels. This is necessary to define a quantization axis and to prevent optical pumping into the outer $m_j = \pm 3/2$ states of the $|5^2D_{3/2}\rangle$ level.

In the regime of a weak magnetic field \vec{B} the spin-orbit interaction dominates over the applied magnetic field (LS -coupling), where the total angular momentum $\vec{J} = \vec{L} + \vec{S}$ is conserved and the atomic levels have multiplicity $(2J + 1)$. The Zeeman substates are described by the magnetic quantum number m_J taking the values $m_J = -J, \dots, +J$. The three fine structure terms of the $^{138}\text{Ba}^+$ level scheme are thus split into an eight level system as indicated in Fig. 2.2. The shifts of the energy levels of the atom are then expected to be

$$E_j = \mu_B m_j g_j |\vec{B}|, \quad (2.1)$$

Transition	λ_{air} (nm)	Γ_{nat} (MHz)
$6^2P_{1/2} \Leftrightarrow 6^2S_{1/2}$	493.408	15.1
$6^2P_{1/2} \Leftrightarrow 5^2D_{3/2}$	649.690	5.3
$6^2P_{3/2} \Leftrightarrow 6^2S_{1/2}$	455.412	18.8
$6^2P_{3/2} \Leftrightarrow 5^2D_{3/2}$	614.171	5.9
$6^2P_{3/2} \Leftrightarrow 5^2D_{5/2}$	585.367	0.7
$5^2D_{3/2} \Leftrightarrow 6^2S_{1/2}$	1761.693	$0.5 \cdot 10^{-8}$
$5^2D_{5/2} \Leftrightarrow 6^2S_{1/2}$	2051.2	$0.4 \cdot 10^{-8}$

Table 2.2: Lowest level transitions in $^{138}\text{Ba}^+$ with the corresponding wavelength in air and the decay rates on the respective transitions [36].

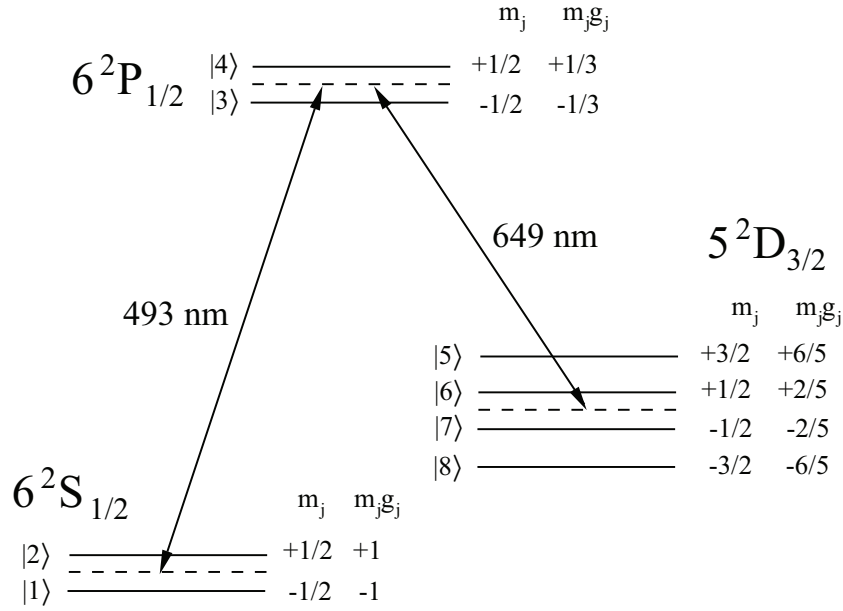


Figure 2.2: Zeeman split 8-level scheme of $^{138}\text{Ba}^+$, relevant for the experiments.

where μ_B is the magnetic moment of the atom and g_j is the Landé factor given by

$$g_j = g_L \frac{J(J+1) + L(L+1) - S(S+1)}{2J(J+1)} + g_S \frac{J(J+1) + L(L+1) - S(S+1)}{2J(J+1)} \quad (2.2)$$

with $g_L \approx 1$ and $g_S \approx 2$, the electron orbital and electron spin gyromagnetic factors. The Landé factors of the relevant levels hence yield

$$g_{|D_{3/2}\rangle} = \frac{4}{5}, \quad g_{|P_{1/2}\rangle} = \frac{2}{3}, \quad g_{|S_{1/2}\rangle} = 2 \quad (2.3)$$

and the associated frequency shifts enter the optical Bloch equations through the quantities:

$$\delta\omega_j = m_j g_j u \quad \text{with} \quad u = \frac{\mu_B}{\hbar} |\vec{B}|. \quad (2.4)$$

2.2 The Bloch equations

To describe the interaction between a single atom and a monochromatic light field an elegant approach is to formulate and solve the problem in terms of Bloch equations. The current section starts out by describing the atom as a three level system (Λ -system) as pictured in Fig. 2.3 and continues in extending this simplified model to an eight level system, which represents the actual term-scheme of a single Barium trapped ion.

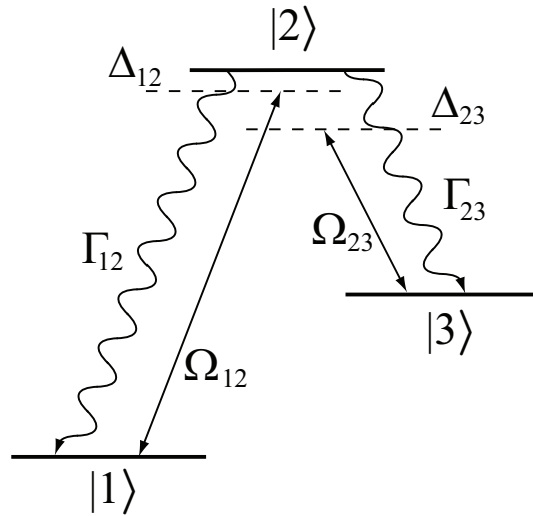


Figure 2.3: Level scheme and the transitions in a Λ -system. The solid arrows represent coherent transitions due to laser excitation and the curvy the lines spontaneous decays.

2.2.1 The three-level system

The complete Hamiltonian for the Λ -system interacting with a laser field can be separated into three parts describing the atom, the light field and the interaction between them given as

$$\hat{H} = \hat{H}_{\text{atom}} + \hat{H}_{\text{field}} + \hat{H}_{\text{int}}. \quad (2.5)$$

for the involved atomic states $|s\rangle$ fulfil Schrödinger equation reads

$$\hat{H}_{\text{atom}}|s\rangle = \hbar\omega_s|s\rangle, \quad (2.6)$$

where the states $|s\rangle$ can be written in the basis

$$|s\rangle, \quad s = 1, 2, 3 \implies \begin{bmatrix} 1 \\ 0 \\ 0 \end{bmatrix}, \begin{bmatrix} 0 \\ 1 \\ 0 \end{bmatrix}, \begin{bmatrix} 0 \\ 0 \\ 1 \end{bmatrix}, \quad (2.7)$$

denoting the eigenvectors of \hat{H}_{atom} corresponding to the electronic levels $|6S\rangle$, $|6P\rangle$, $|5D\rangle$ of a barium ion as shown in Fig. 2.1, respectively.

The atomic Hamiltonian can then be written in a matrix representation with the zero point energy chosen at level $|2\rangle$

$$\hat{H}_{\text{atom}} = \hbar \begin{bmatrix} \omega_1 - \omega_2 & 0 & 0 \\ 0 & 0 & 0 \\ 0 & 0 & \omega_3 - \omega_2 \end{bmatrix}. \quad (2.8)$$

The quantized free-field Hamiltonian of the light modes in the representation of plane waves with wave vectors \vec{k} is expressed with the quantum mechanical Hamiltonian of harmonic oscillators as

$$\hat{H}_{\text{field}} = \sum_{\vec{k}} \hbar\omega_{\vec{k}} \left[\hat{a}_{\vec{k}}^\dagger \hat{a}_{\vec{k}} + \frac{1}{2} \right]. \quad (2.9)$$

Here, $\hat{a}_{\vec{k}}$ and $\hat{a}_{\vec{k}}^\dagger$ are the photon annihilation and creation operators, respectively. The eigenvectors of \hat{H}_{field} are then the number states $|n\rangle$ containing n photons with each carrying the energy $\hbar\omega_{\vec{k}}$. In the case of a coherent light field the occupation of the energy number states in the basis of Fock states is then given by a linear superposition as

$$|\alpha\rangle = e^{-\frac{1}{2}|\alpha|^2} \sum_{n=0}^{\infty} \frac{\alpha^n}{\sqrt{n!}} |n\rangle, \quad (2.10)$$

where α can be a complex number.

For a single mode \vec{k} the corresponding field operator as a function of position and time then reads [38]

$$\hat{E}_{\text{field}}(\vec{x}, t) = i\sqrt{\frac{\hbar\omega_{\vec{k}}}{2\epsilon_0 V}} \left[\hat{a}_{\vec{k}} e^{-i\omega_{\vec{k}}t + i\vec{k}\cdot\vec{x}} - \hat{a}_{\vec{k}}^\dagger e^{i\omega_{\vec{k}}t - i\vec{k}\cdot\vec{x}} \right] \vec{\epsilon}_{\vec{k}} \quad (2.11)$$

with the wave vector \vec{k} and frequency $\omega_{\vec{k}}$ of one mode of the field, satisfying the vacuum dispersion relation $\omega_{\vec{k}} = c|\vec{k}|$. V denotes the quantization volume, $\vec{\epsilon}_{\vec{k}}$ is the

unit vector indicating the polarization direction and ϵ_0 is the vacuum permittivity. To address all levels in the Λ -system two laser fields are required as $\widehat{E}_{\text{field}} = \widehat{E}_{12} + \widehat{E}_{23}$.

Since the scattering rate of the atom is negligible compared to the photon number in the laser beam we can assume that the light field is defined by the same coherent state before and after the interaction. Furthermore, the spatial dependence $\vec{k} \cdot \vec{x}$ of the light field over the atom is on the order of $a_{\text{Bohr}}/\lambda \sim 10^{-4}$ and can be omitted.

We can now rewrite the expectation value of the combined electric field operators for a coherent state $|\alpha_{12}, \alpha_{23}\rangle$ as

$$\langle \alpha_{12}, \alpha_{23} | \widehat{E}_{\text{field}} | \alpha_{12}, \alpha_{23} \rangle = [\vec{\epsilon}_{12} E_{12}^0 \cos(\omega_{12}t + \phi_{12}) + \vec{\epsilon}_{23} E_{23}^0 \cos(\omega_{23}t + \phi_{23})] \quad (2.12)$$

with the electric field amplitudes E_l^0 , $l = \{12, 23\}$ of the respective lasers given by

$$E_l^0 = 2\sqrt{\frac{\hbar\omega_l}{2\epsilon_0 V}} |\alpha_l|. \quad (2.13)$$

To describe the interaction between the atom and the light field the charge density of the atomic system can be expanded into a multipolar series. Then, in the electric dipole approximation of the atom, where we discard higher order electric and magnetic terms, the interaction Hamiltonian takes the form

$$\widehat{H}_{\text{int}} = -\vec{d} \cdot \widehat{E}_{\text{field}}, \quad (2.14)$$

where \vec{d} represents the atomic dipole operator between two levels. In the expression of the atomic eigenstates \vec{d} reads

$$\vec{d} = \sum_{ab=1,2,3} \vec{d}_{ab} |a\rangle \langle b|, \quad \vec{d}_{ab} = \langle a | \vec{d} | b \rangle. \quad (2.15)$$

For this assumption to remain valid the laser fields must be near resonance with their respective transitions. Thus, in this picture off-resonant oscillating terms, e.g. $\omega_{12} \pm \omega_{23}$, in the exponents will average to zero on an appreciable time scale and can be neglected. In this rotating-wave approximation \widehat{H}_{int} can be rewritten as

$$\widehat{H}_{\text{int}} = \hbar \begin{bmatrix} 0 & \frac{\Omega_{12}}{2} e^{+i\omega_{12}t} & 0 \\ \frac{\Omega_{12}}{2} e^{-i\omega_{12}t} & 0 & \frac{\Omega_{23}}{2} e^{-i\omega_{23}t} \\ 0 & \frac{\Omega_{23}}{2} e^{+i\omega_{23}t} & 0 \end{bmatrix} \quad (2.16)$$

with

$$\Omega_{12} = \frac{\vec{\epsilon}_{12}}{\hbar} \cdot \vec{d}_{12} E_{12}^0 \quad (2.17)$$

$$\Omega_{23} = \frac{\vec{\epsilon}_{23}}{\hbar} \cdot \vec{d}_{23} E_{23}^0 \quad (2.18)$$

being the Rabi frequencies, which describe the coupling strengths between the light field and the atom.

Combining all contributions from above the complete Hamiltonian is expressed in a matrix form as

$$\hat{H} = \hbar \begin{bmatrix} \omega_1 - \omega_2 & \frac{\Omega_{12}}{2} e^{+i\omega_{12}t} & 0 \\ \frac{\Omega_{12}}{2} e^{-i\omega_{12}t} & 0 & \frac{\Omega_{23}}{2} e^{-i\omega_{23}t} \\ 0 & \frac{\Omega_{23}}{2} e^{+i\omega_{23}t} & \omega_2 - \omega_3 \end{bmatrix}. \quad (2.19)$$

Density operator formalism

Until this point we did not include the spontaneous decay of the excited atomic states in the Hamiltonian. This dissipative process arises due to the coupling of the electronic states in the atom to the electromagnetic modes of the environment. Together with other decoherence effects such as finite laser linewidths this would require a description of the atomic system coupling to a surrounding heat-bath with an infinite number of modes. Nevertheless, restricting the description to only the atomic subsystem, we can treat the interaction of the atom with its environment by statistical means in a density matrix formalism. The density operator is then defined, written in the atomic basis $|a\rangle$, as

$$\hat{\rho} = \sum_{a,b=1,2,3} \rho_{ab} |a\rangle \langle b|. \quad (2.20)$$

Here, the diagonal elements are the probabilities of finding the atom in the respective state, such that the normalization yields

$$\text{Tr}[\hat{\rho}] = \rho_{11} + \rho_{22} + \rho_{33} = 1. \quad (2.21)$$

The off-diagonal elements, e.g. $\langle 1|\hat{\rho}|2\rangle$, describe the atomic coherences. They are superpositions between two quantum states, where ρ_{12} and ρ_{32} oscillate with their respective driving laser frequency. ρ_{13} denotes the coherence between the $|S_{1/2}\rangle$ and the $|D_{3/2}\rangle$ state and oscillates with the difference frequency of the two applied light fields.

The dynamics of the density matrix is then governed by the von Neumann equation with an additional relaxation term describing the decoherent effects as:

$$\frac{d\hat{\rho}}{dt} = -\frac{i}{\hbar} [\hat{H}, \hat{\rho}] + \mathcal{L}_{\text{relax}}(\hat{\rho}) = \mathcal{L}(\hat{\rho}). \quad (2.22)$$

This form is called the Master equation and the relaxation operator $\mathcal{L}_{\text{relax}}$ is given by

$$\mathcal{L}_{\text{relax}}(\hat{\rho}) = -\frac{1}{2} \sum_{\mathbf{n}} (\hat{C}_{\mathbf{n}}^{\dagger} \hat{C}_{\mathbf{n}} \hat{\rho} + \hat{\rho} \hat{C}_{\mathbf{n}}^{\dagger} \hat{C}_{\mathbf{n}} - 2\hat{C}_{\mathbf{n}} \hat{\rho} \hat{C}_{\mathbf{n}}^{\dagger}), \quad (2.23)$$

where dissipative effects can be described by different \widehat{C}_n operators associating individual couplings between the atomic system and the reservoir. They are written as an amplitude times a projector for the transition or state as:

$$\widehat{C}_{21} = \sqrt{\Gamma_{21}}|1\rangle\langle 2| \quad (2.24)$$

$$\widehat{C}_{23} = \sqrt{\Gamma_{23}}|3\rangle\langle 2| \quad (2.25)$$

$$\widehat{C}_{11} = \sqrt{\delta_{12}}|1\rangle\langle 1| \quad (2.26)$$

$$\widehat{C}_{33} = \sqrt{\delta_{23}}|3\rangle\langle 3|. \quad (2.27)$$

Here, δ_{12} and δ_{23} are the laser linewidths of the two involved laser transitions and Γ_{21} and Γ_{23} are the spontaneous decay rates of the respective atomic levels. In a homogeneous environment this spontaneous emission rate can be described by Fermi's golden rule [39]:

$$\Gamma_{ab} = \frac{8\pi^2}{3\epsilon_0\hbar\lambda_{ab}^3}|\vec{d}_{ab}|^2. \quad (2.28)$$

Using the decay rates we further define a saturation parameter S as

$$S_{12} = \frac{\Omega_{12}}{\Gamma_{12}} \quad S_{23} = \frac{\Omega_{23}}{\Gamma_{23}}. \quad (2.29)$$

As a last step we transform the system into a frame rotating at the laser frequencies ω_{12} and ω_{23} applying the unitary operator

$$\widehat{U} = \begin{bmatrix} e^{-i\omega_{12}t} & 0 & 0 \\ 0 & 1 & 0 \\ 0 & 0 & e^{-i\omega_{23}t} \end{bmatrix}. \quad (2.30)$$

The Hamiltonian \widehat{H} and density operator ρ from Eq. 2.22 are then transformed, where the relaxation terms remain unchanged, as

$$\widehat{H}' = \widehat{U}\widehat{H}\widehat{U}^\dagger - i\hbar\widehat{U}\frac{d\widehat{U}^\dagger}{dt} \quad (2.31)$$

and

$$\hat{\rho}' = \widehat{U}\hat{\rho}\widehat{U}^\dagger. \quad (2.32)$$

We thus find the transformed complete Hamiltonian from Eq. (2.19) as

$$\widehat{H}' = \hbar \begin{bmatrix} \Delta_{12} & \frac{\Omega_{12}}{2} & 0 \\ \frac{\Omega_{12}}{2} & 0 & \frac{\Omega_{23}}{2} \\ 0 & \frac{\Omega_{23}}{2} & \Delta_{23} \end{bmatrix} \quad (2.33)$$

with the laser detunings from the respective atomic Bohr frequencies given by:

$$\Delta_{12} = \omega_{12} - (\omega_2 - \omega_1), \quad \Delta_{23} = \omega_{23} - (\omega_2 - \omega_3). \quad (2.34)$$

To solve the Master equation of the system we rewrite Eq. (2.22) in a set of linear equations into a vector form, where $\hat{\rho}$ transforms into a density vector

$$\vec{P} := (\rho_{11}, \rho_{12}, \rho_{13}, \dots, \rho_{33}) \quad (2.35)$$

and the linear equations of motion for \vec{P} are:

$$\frac{d\vec{P}_1}{dt} = \sum_k \widehat{M}_{1k} \vec{P}_k. \quad (2.36)$$

These nine coupled linear equations are called optical Bloch equations. By introducing the normalization $\text{Tr}[\vec{P}] = 1$ one of the Bloch equations can be canceled. The stationary solution of the Bloch equations is given by

$$\frac{d\vec{P}_1}{dt} = \sum_k \widehat{M}_{kl} \vec{P}_k = 0, \quad (2.37)$$

where these equations can be solved by diagonalizing of the 8x8 Matrix \widehat{M}_{kl} .

Let us now consider the special case, where the detunings of the two laser fields are set to be identical ($\Delta_{12} = \Delta_{23}$) resulting in a Raman transition. Then, assuming ideally small laserlinewidths ($\delta_{12} = \delta_{23} = 0$), the Bloch equations take the stationary solutions

$$\begin{aligned} \rho_{11} &= \frac{\Omega_{32}^2}{\Omega_{12}^2 + \Omega_{32}^2} \\ \rho_{33} &= \frac{\Omega_{12}^2}{\Omega_{12}^2 + \Omega_{32}^2} \\ \rho_{31} &= \rho_{13} = \frac{-\Omega_{12}\Omega_{32}}{\Omega_{12}^2 + \Omega_{32}^2} \\ \rho_{i,2} &= \rho_{2,j} = 0, \quad i, j = 1, 2, 3. \end{aligned} \quad (2.38)$$

Apparently, the diagonal element ρ_{22} as well as the off-diagonal coherences from and to the excited state $|2\rangle$ vanish. The population is in a superposition between the state $|1\rangle$ and $|3\rangle$ with the coherence governed by ρ_{13} .

2.2.2 The eight-level system

In this section the model from a three level Λ -system is extended to a more realistic picture describing a Ba^+ ion. As already pointed out in Sec. 2.1 in the experiment a weak magnetic field at the position of the ion splits the degenerated three-level system into an eight-level system. Here, the individual states are defined as indicated in Fig. 2.2. The dynamics of the atomic levels is now governed by an extended density matrix formalism with a density vector of now 64 entries as

$$\vec{P} = (\rho_{11}, \rho_{12}, \dots, \rho_{41}, \rho_{42}, \dots, \rho_{87}, \rho_{88}) \quad (2.40)$$

together with a set of optical Bloch equations similar to Eq. 2.36 and is elaborated in [35].

In this extended Λ -system after a successful absorption of a laser photon the ion is in one of the two $|P_{1/2}\rangle$ states. From there it can decay either into one of the $|S_{1/2}\rangle$ states with the emission of a 493 nm (green) photon or into one of the four $|D_{3/2}\rangle$ states with the emission of a 650 nm (red) photon with a branching ratio of 3:1 (see Tab. 2.1.1). The emission rate of photons is thus proportional to the population of the excited $|P_{1/2}\rangle$ states (ρ_{33} and ρ_{44}) in the steady state limit. Collecting a fraction of the emitted photon stream the mean count rate $\langle N \rangle$ at a detector is then given by:

$$\langle N \rangle \propto \rho_{ee}, \quad \rho_{ee} = \rho_{33} + \rho_{44}. \quad (2.41)$$

For simplicity we will from now on denote the emitted light and the indices of the laser parameters, such as detuning, linewidth and Rabi-frequency, with the respective color of the transition wavelength, green or red.

Further statements about the observable fluorescence require that the geometrical configuration of the ion with respect to the laser and magnetic field direction has to be taken into account. In all performed measurements we apply a laser polarization, which is perpendicular to the magnetic field vector ($\alpha = 90^\circ$) and to the laser propagation direction as $\vec{k} \perp \vec{B} \perp \vec{e}$. In such a configuration only $\Delta m_j \pm 1$ transitions are excited, whereas $\Delta m_j = 0$ transitions are forbidden. Thus, the linearly polarized green and red laser is seen as a superposition of left and right circular polarized photons addressing the individual transitions. Moreover, the observation direction in all experiments is placed in the direction of the magnetic field vector. Along this direction we collect photons from a mixture of $\Delta m = \pm 1$ transitions composing the green fluorescence, i.e. the $|P_{1/2}, m = -1/2\rangle \rightarrow |S_{1/2}, m = +1/2\rangle$ transition associated with a creation of a single green $\Delta m = +1$ photon with σ^- polarization and the $|P_{1/2}, m = +1/2\rangle \rightarrow |S_{1/2}, m = -1/2\rangle$ transition associated with a creation of a single green $\Delta m = -1$ photon with σ^+ polarization. This described configuration is sketched in Fig. 2.4. Depending on the strength of the elastic and inelastic scattering processes these two involved transitions, when measured at a detector, result in a

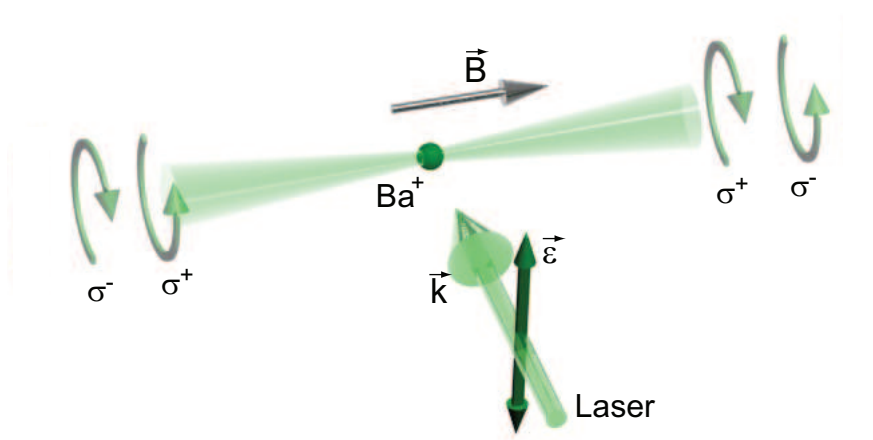


Figure 2.4: Sketch of the geometrical configuration of the ion with respect to the magnetic field vector \vec{B} , the observation direction and the laser beam. Here, $\vec{\epsilon}$ and \vec{k} indicate the laser polarization vector and propagation direction, respectively. σ^+ and σ^- signal the circular polarization of scattered fluorescence photons. Note that only the green fluorescence and laser are shown. See text for details.

more coherent or incoherent mixture of the associated light fields, respectively. This scattering dynamics is elaborated in Sec. 3.1.2 for a simplified two level system for various Rabi-frequencies.

Excitation spectra

Above we have already mentioned that the expected count rate at a detector is proportional to the population of the excited states. Based on this finding excitation spectroscopy can be performed by successively observing the ion's resonance fluorescence as a function of one laser detuning. Because of the branching ratio of the $|P_{1/2}\rangle$ state it is most efficient in the experiment to record only green fluorescence photons, while varying the detuning of the red laser. Since for an excitation spectrum the count rate is typically integrated over a time scale (100 ms - 1 s) much larger than the lifetime of the excited state the atom is observed in steady state condition with the laser fields as indicated in Eq. (2.41). Hence, the simulation of excitation spectra only requires the stationary solutions of the Bloch equations from Eq. (2.37).

In the case of a three-level system we have seen above that for equal laser detunings

a Raman transition will occur. Eq. (2.39) hereby provided the governing steady state relations between the three energy levels. A similar effect can be expected to happen for the situation of an eight-level system. In the vicinity of equal detunings of the red and green laser fields a total number of eight possible Raman transitions appear, being the total number of direct transitions between the two $|S_{1/2}\rangle$ and the four $|D_{3/2}\rangle$ states. As in the three-level system the excited states are not populated. No photons are scattered from the ion and the populations are directly transferred from the $|S_{1/2}\rangle$ to the $|D_{3/2}\rangle$ state. Hence, the Raman transitions are associated with eight so called dark resonances visible in the excitation spectra. They appear as sharp dips, going to zero count rate for the case of ideal small laser linewidths.

In the experiment the positions, depths and widths of the dark resonances depend on all experimental parameters, such as the laser settings, magnetic field strength and furthermore the angles between the magnetic field vector \vec{B} , the laser polarization \vec{e} and laser propagation direction \vec{k} . Because of its sensitivity to all parameters, measuring an excitation spectra is used as an important tool to calibrate the experiment prior to taking data (see Sec. 5.3.5).

In the geometrical configuration described previously ($\vec{k} \perp \vec{B} \perp \vec{e}$) only four dark resonances are visible within the profile of the excitation spectra. As an example, Fig. 2.5 depicts a simulation of an excitation spectrum for typical experimental parameters. The top graph corresponds to the excited state populations in the steady state limit and is directly proportional to the recorded fluorescence in the experiment, while the bottom graph gives the expected populations for the different $|D_{3/2}\rangle$ states. Raman transitions occur at four resonant positions between the states $|1\rangle \leftrightarrow |5\rangle$, $|1\rangle \leftrightarrow |7\rangle$ and $|2\rangle \leftrightarrow |6\rangle$, $|2\rangle \leftrightarrow |8\rangle$ (see Fig. 2.2). The four dark resonances correspond to the increase of the population in one of the individual $D_{3/2}$ states. This simulation along with all further presented calculations throughout the course of this work are based on numerical routines in the Matlab environment employing the Quantum Optical Toolbox [40].

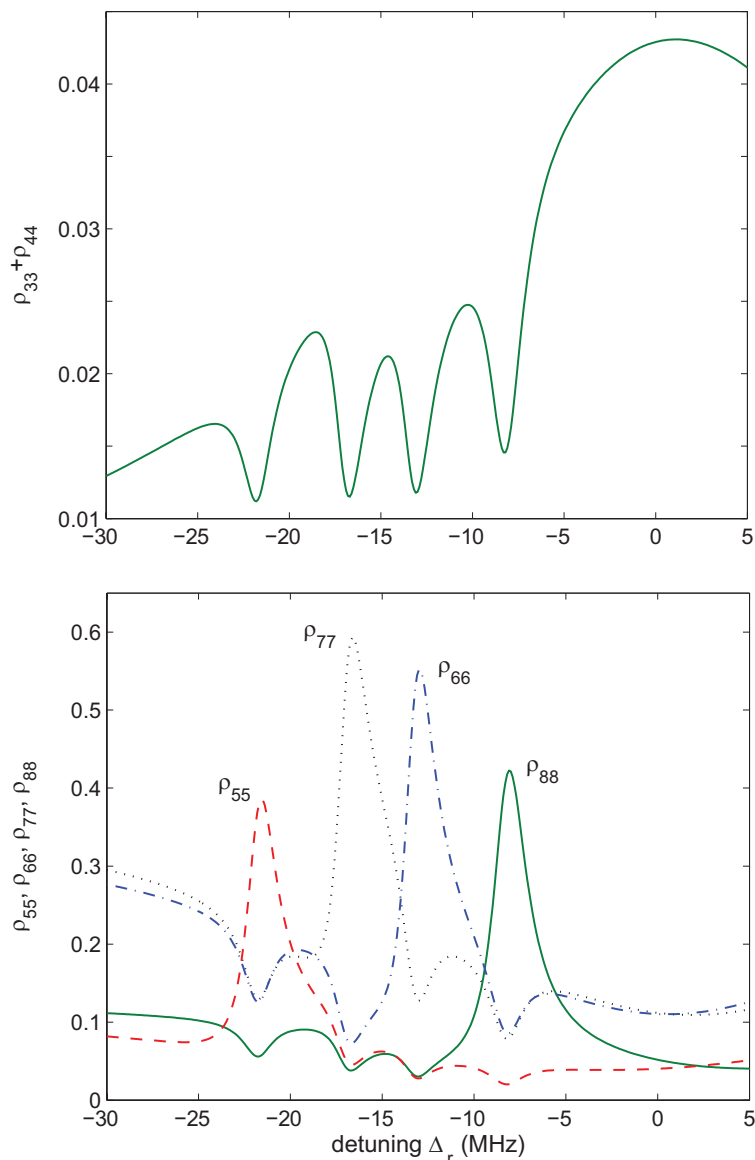


Figure 2.5: Steady state population of the energy levels of barium upon continuous laser excitation on the red and green transition. Top graph: Summed population of the $6^2P_{1/2}$ levels of a Barium ion in dependence of the detuning Δ_r (excitation spectrum) simulated with 8 level optical Bloch equations with the parameters: $S_g = 0.95, S_r = 2.25, \Delta_g/2\pi = -15$ MHz, $\delta_g/2\pi = \delta_r/2\pi = 100$ kHz, $u/2\pi = 3.1$ MHz, $\alpha = 90^\circ$. Bottom graph: Populations of the individual $5^2D_{3/2}$ levels as shown in Fig. 2.2 in dependence of the detuning Δ_r .

Chapter 3

Correlation functions

While the above mentioned excitation spectra monitor fluorescence and populations in steady state, the temporal evolution of the internal states can best be recorded with the aid of correlation functions. This possibility of extracting the time resolved dynamics of an ion is heavily used throughout this thesis to calibrate and quantify experimental findings.

The following chapter starts with a general description of the formalism of correlation functions. Adjacent to this, the three correlation functions relevant for this work are successively discussed initially for the case of a simple two-level system and then for the eight level system of a Ba⁺ ion.

In general, a correlation function of electric fields E at arbitrary space-time points can be defined in a normalized form as [38, 41]:

$$\begin{aligned} g^{(n)}(\vec{r}_1 t_1, \dots, \vec{r}_n t_n, \vec{r}_{n+1} t_{n+1}, \dots, \vec{r}_{2n} t_{2n}) &= \\ &= \frac{\int_T [E^*(\vec{r}_1, t_1) \dots E^*(\vec{r}_n, t_1 + t_{n,1}) E(\vec{r}_{n+1}, t_1 + t_{n+1,1}) \dots \\ &\quad \dots E(\vec{r}_{2n}, t_1 + t_{2n,1})] dt_1}{\left[\int_T |E(\vec{r}_1, t_1)|^2 dt_1 \dots \int_T |E(\vec{r}_n, t_1 + t_{n,1})|^2 dt_1 \int_T |E(\vec{r}_{n+1}, t_1 + t_{n+1,1})|^2 dt_1 \dots \right. \\ &\quad \left. \dots \int_T |E(\vec{r}_{2n}, t_1 + t_{2n,1})|^2 dt_1 \right]^{1/2}}, \end{aligned} \tag{3.1}$$

In the performed experiments, however, only parallel light beams are involved with only a single spatial coordinate restricting Eq. (3.1) to purely time-like correlation functions. The integral form of Eq. (3.1) is conventionally expressed as brackets $\langle \dots \rangle$ denoting the expectation value or statistical average over all values of the field at time t and $t + \tau$ within the duration of the measurement. The correlation functions are then usually extracted from an analysis of the measured detection events of the emitted light as described in Sec. 5.2.2. It is this concept of optical coherences that proved to be an efficient way to get insight to the quantum dynamics of an ion.

3.1 First-order correlation function

The first-order coherence expresses the phase fluctuations of a light field and with that the associated decrease of its ability to interfere. In a normalized form this quantity is defined as

$$g^{(1)}(t, t + \tau) = g^{(1)}(\tau) = \frac{\langle \hat{E}^-(t) \hat{E}^+(t + \tau) \rangle}{\langle \hat{E}^-(t) \hat{E}^+(t) \rangle}, \quad (3.2)$$

where $\hat{E}^\pm(t)$ represent the positive/negative frequency parts of the quantized electric field and the averages $\langle \dots \rangle$ are assumed to be taken in the steady state of the system, i.e. $\langle \hat{E}^-(t) \hat{E}^+(t + \tau) \rangle$ is a function of τ only.

$g^{(1)}(\tau)$ hence gives the degree of first-order temporal coherence between the electric fields at time t and $t + \tau$ [38] and takes the values $0 \leq |g^{(1)}(\tau)| \leq 1$ for all light sources. This correlation is specially of interest as the Fourier transform yields the frequency dependent spectrum of the light. According to the *Wiener-Khintchine theorem* the power spectrum $F(\omega)$ is then given in terms of the two-time correlation function as

$$F(\omega) = \frac{1}{2\pi} \text{Re} \int_{-\infty}^{+\infty} g^{(1)}(\tau) e^{i\omega\tau} d\tau. \quad (3.3)$$

For a chaotic light source with linewidth Γ and center frequency ω the normalized first degree of coherence for the two most important types of frequency distribution Lorentzian and Gaussian is given by [38]

$$g^{(1)}(\tau) = \exp(-i\omega\tau - \Gamma|\tau|), \quad (3.4)$$

$$g^{(1)}(\tau) = \exp(-i\omega\tau - \frac{1}{2}\Gamma^2\tau^2), \quad (3.5)$$

respectively. The left side of Fig. 3.1 pictures a possible setup to measure the first order coherence with a Michelson type interferometer. The light beam is divided with a 50/50 beam splitter (BS) into two parts and sent to two mirrors. One mirror is movable and its adjustable position directly corresponds to the delay time τ between the two interfering fields at the BS. As the light beams are then retro-reflected onto the BS, the interfering fields are detected at a photomultiplier tube (PMT). The bottom part of Fig. 3.1 shows a plot of the $|g^{(1)}(\tau)|$ as given in Eq. 3.5. In the limit when the linewidth $\Gamma \rightarrow 0$ the light field is perfectly coherent and $g^{(1)}(\infty) = 1$. In chapter. 8 the $g^{(1)}(\tau)$ of a single ion is measured and discussed using a self-homodyne setup.

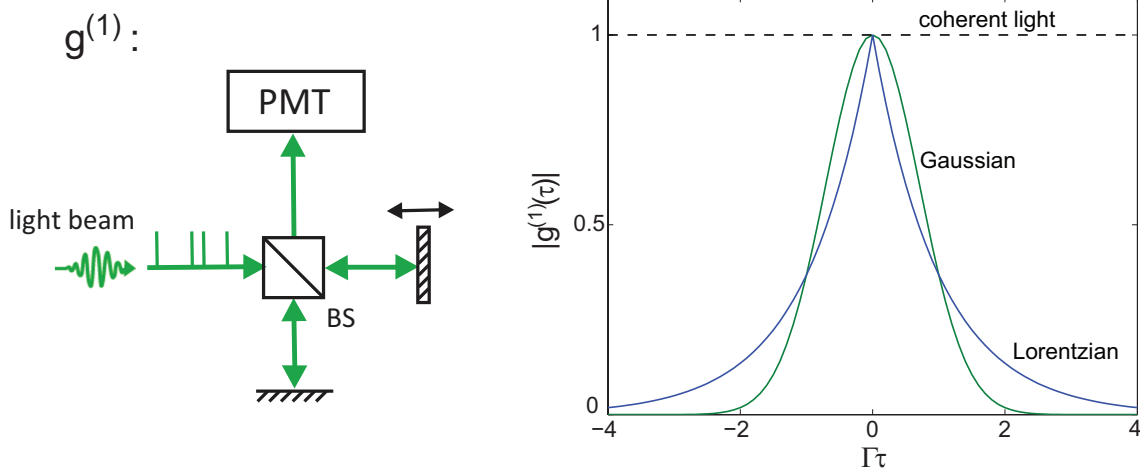


Figure 3.1: Picture of a Michelson interferometer (top), sketch of the first order correlation function for a Gaussian and Lorentzian frequency distribution as described in Eq. 3.5 and for an ideal coherent light field (bottom).

3.1.1 First order coherence and spectrum of a two-level system

To calculate the correlation function of an atomic system we will first consider a two-level system. The excited state has a lifetime $1/\Gamma$ and transition frequency ω_0 . The system is driven at a Rabi frequency Ω with an incident laser light at frequency ω . The laser linewidths is hereby assumed to be infinitely narrow. The state of our two-level hydrogen-like atomic system is a linear combination of the states $|a\rangle$ and $|b\rangle$ as $|\Psi\rangle = C_a|a\rangle + C_b|b\rangle$, and can be expressed as a system density operator $\rho = |\Psi\rangle\langle\Psi|$ written in the matrix form

$$\hat{\rho} = \begin{bmatrix} \rho_{aa} & \rho_{ab} \\ \rho_{ba} & \rho_{bb} \end{bmatrix}. \quad (3.6)$$

Considering the coordinate operator of the bound electron \vec{q} with charge e the mean atomic polarization is further given by

$$\langle e\vec{q} \rangle = \vec{d}_{ab}\rho_{ba} + \vec{d}_{ba}\rho_{ab}. \quad (3.7)$$

with the dipole matrix element $\vec{d}_{ab} = e\langle a|\vec{q}|b\rangle$, $\vec{d}_{ba} = \vec{d}_{ab}^*$.

For deducing the first order correlation function from Eq. (3.2) we hence require the two-time expectation value of the electric field operator. In general, the one-time

expectation value of some observable \widehat{O} at a time t for some density operator $\hat{\rho}$ as governed by the Master equation $d\hat{\rho}/dt = \mathcal{L}(\rho)$ (see Eq. (2.22)) is represented by

$$\langle \widehat{O}(t) \rangle = \text{Tr}[\widehat{O}(t)\hat{\rho}(0)] = \text{Tr}[\widehat{O} e^{\mathcal{L}t} \hat{\rho}(0)], \quad (3.8)$$

where the operator on the left side is in the Heisenberg picture while those on the right are in the Schrödinger picture. A similar result is expected in the time limit $t \rightarrow \infty$, where the system has reached an equilibrium between excitation and dissipation following in a stationary solution $\hat{\rho}_{ss} = d\hat{\rho}/dt = 0$ as

$$\langle \widehat{O}_{ss} \rangle = \text{Tr}[\widehat{O}\hat{\rho}_{ss}]. \quad (3.9)$$

In the case of the two-time average the quantum regression theorem states that [42]

$$\langle \widehat{O}(t + \tau)\widehat{O}(t) \rangle = \text{Tr}[\widehat{O} e^{\mathcal{L}\tau} \widehat{O}\hat{\rho}(t)]. \quad (3.10)$$

Here, the right hand side is formally identical to that of $\langle \widehat{O}(t) \rangle$, except that after the initial condition $\widehat{O}\hat{\rho}(t)$ the system evolves for the time period τ expressed by the evolution operator $\exp\mathcal{L}\tau$ before the second multiplication of \widehat{O} . The expectation value is then found by taking the trace of the time average $\hat{\rho}$.

Introducing the Pauli lowering operator as $\hat{\sigma}^- = |b\rangle\langle a|$ and using Eq. (3.8) we can now write the time-evolution of the expectation value of $\hat{\sigma}^-$ as

$$\langle \hat{\sigma}^-(t) \rangle = \text{Tr}[|b\rangle\langle a|\rho(t)] = \langle a|\rho(t)|b\rangle = \rho_{ab}(t). \quad (3.11)$$

Since the creation of a photon goes hand in hand with the system being projected to its ground state we can relate the electric field operator with the lowering operator. The dipolar radiated source field of the two-level system positioned at the origin of \vec{r} -space is then given in a rotating frame picture at the laser frequency ω_L at the retarded time $t - r/c$ as [43]

$$\widehat{\mathcal{E}}^+(\hat{r}, t) = -\frac{\omega_L^2}{4\pi\epsilon_0 c^2 r} (\vec{d}_{ab} \times \hat{r}) \times \hat{r} e^{-i\omega_L(t-r/c)} \Theta(t - r/c) \hat{\sigma}^-(t), \quad (3.12)$$

where $\hat{r} = \vec{r}/r$ is the unit vector in radial direction, $\Theta(t - r/c)$ is a step function centered at $t - r/c = 0$ and $\vec{d}_{ab}\hat{\sigma}^-$ is the dipole moment operator. For further notations it is more convenient to rewrite Eq. (3.12) in a more simplified form for the steady state limit $t \rightarrow \infty$ as

$$\widehat{\mathcal{E}}^+(t) = \kappa e^{-i\omega_L t} \hat{\sigma}^-(t) \vec{e}, \quad (3.13)$$

where κ represents a constant amplitude and \vec{e} is the polarization unit vector of the radiation. Using the two-time correlation function from Eq. (3.10) the first-order coherence then results in an unnormalized form

$$\begin{aligned} G^{(1)}(t, t + \tau) &= \langle \widehat{\mathcal{E}}^-(t)\widehat{\mathcal{E}}^+(t + \tau) \rangle = \text{Tr}[\widehat{\mathcal{E}}^- e^{\mathcal{L}\tau} \widehat{\mathcal{E}}^+ \hat{\rho}(t)] \\ &\propto \text{Tr}[\hat{\sigma}^+ e^{\mathcal{L}\tau} \hat{\sigma}^- \hat{\rho}(t)]. \end{aligned} \quad (3.14)$$

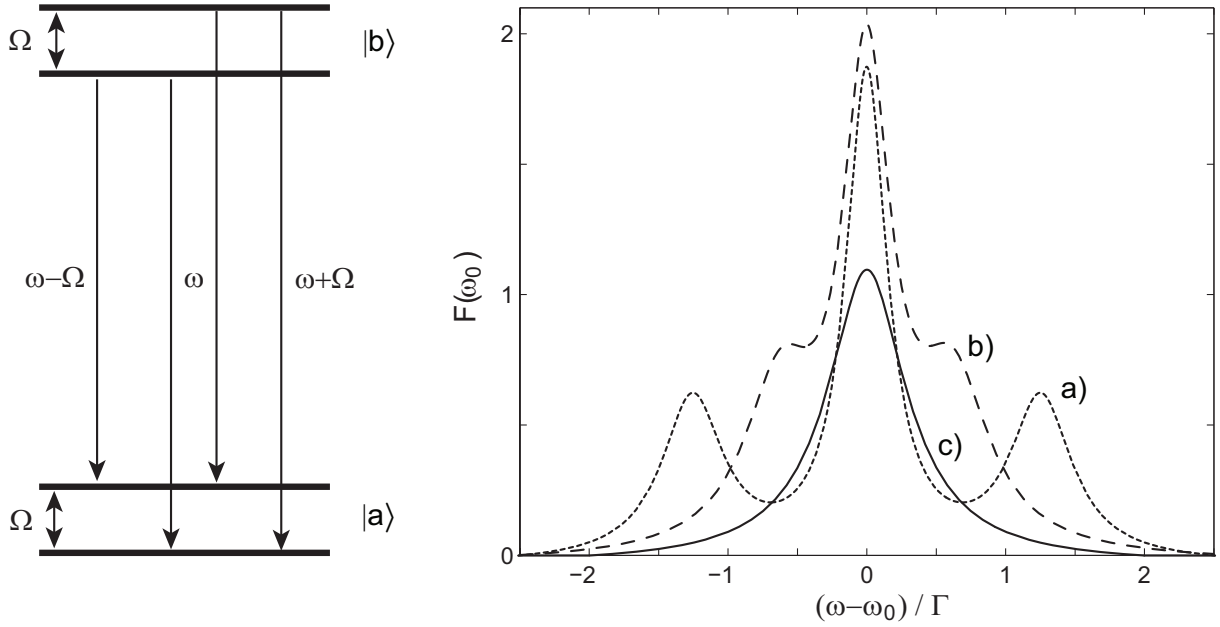


Figure 3.2: *Left*: Splitting of the two-level system $|a\rangle$ and $|b\rangle$ by the dynamic Stark effect. *Right*: Fluorescence power spectrum $F(\omega_0)$ in arbitrary units of a two-level atomic system as given by Eq. (3.18) for a) (dashed line) $\Omega/\Gamma = 7$, b) (dotted line) $\Omega/\Gamma = 3/2$ and c) (solid line) $\Omega/\Gamma = 1/3$.

The first-order coherence will show distinguishable characteristics depending on the excitation intensity of the laser and hence on the Rabi frequency associated with the driving field.

For the situation of $\Omega \ll \Gamma$, when the Rabi frequency of the driving field is much smaller than the rate of emission of spontaneously radiated photons the system is in the weak field limit. Here the atom behaves as an overdamped quantum harmonic oscillator and the power spectrum can be assumed by a δ -function at the driving frequency as predicted for the energy conservation of elastic Rayleigh scattering. In this regime the first-order coherence is approximated by [42]

$$G^{(1)}(\tau) \cong \left(\frac{\Omega}{\Gamma}\right)^2 e^{-i\omega\tau}. \quad (3.15)$$

The power spectrum is then found according to Eq. (3.3) as

$$F(\omega_0) = \left(\frac{\Omega}{\Gamma}\right)^2 \delta(\omega - \omega_0). \quad (3.16)$$

The situation is considerably different when the strength of the incident laser field increases and the Rabi frequency becomes comparable to the atomic linewidth. In the regime of strong excitation, $\Omega \gg \Gamma$, the atomic states split by the dynamic Stark effect indicated in the left side of Fig. 3.2. Here the Rabi oscillations appear as a modulation of the atomic dipole moment observable in the emerging of sidebands in the fluorescence spectrum. The first-order coherence of the two-level system can then be approximated for the initial conditions $\rho_{aa} = \rho_{bb} = 1/2, \rho_{ab} = \rho_{ba} = 0$ as [42]

$$G^{(1)}(\tau) = \frac{1}{4} \left(e^{-\frac{\Gamma}{2}\tau} + \frac{1}{2} e^{-\frac{3\Gamma}{4}\tau} e^{-i\Omega\tau} + \frac{1}{2} e^{-\frac{3\Gamma}{4}\tau} e^{i\Omega\tau} \right) e^{-i\omega\tau}, \quad (3.17)$$

with the power spectrum given by

$$F(\omega_0) = \frac{1}{2\pi} \left(\frac{3\Gamma/4}{(\omega + \Omega - \omega_0)^2 + (3\Gamma/4)^2} + \frac{\Gamma}{(\omega - \omega_0)^2 + (\Gamma/2)^2} + \frac{3\Gamma/4}{(\omega - \Omega - \omega_0)^2 + (3\Gamma/4)^2} \right). \quad (3.18)$$

The right side of Fig. 3.2 depicts $F(\omega_0)$ for various values of Ω/Γ . In curve a) the Rabi frequency is chosen largest demonstrating the basic physics of the three-peak fluorescence spectrum around $\omega_0 = \omega, \omega \pm \Omega$, i.e. Mollow-triplet [44], where the relative height of these peaks is given by the ratio 1 : 3 : 1. For a smaller Ω/Γ ratio the sideband peaks disappear as seen in curve c). As visible in the finite width of the power spectrums the main contribution of the scattered radiation is found to be incoherent compared to the incident laser field. The remaining elastically scattered contribution proportional to $\delta(\omega - \omega_0)$ is hereby not contained in the individual curves.

3.1.2 Elastic and inelastic scattering

As indicated above we can distinguish between two principle categories of scattering processes.

In *inelastic* collisions photons are absorbed and then emitted by the atom. This effect can be expressed by a decay rate of the atomic populations and appears in the optical Bloch equations as an additional damping term. It corresponds to the radiation emitted from the fluctuating part of the atomic dipole. Especially, the emitted photons do not have a well defined phase with respect to the incident laser field.

Elastic scattering leaves the atom in the same initial energy level and the effect is merely limited to changes in the phase of the atomic wavefunction and is also referred to as Rayleigh scattering. We have seen that some information of the coherence properties of the scattered light is obtained from the expectation values of $\hat{E}^-(t)$ and $\hat{E}^+(t)$. The sum of these expectation values has a sinusoidal dependence on position and time and can be written similar to Eq. (2.12) as the electric field

associated with a coherent state. This part now oscillates with a well defined phase relative to the incident laser field and is denoted as the elastically scattered fraction of the radiation. The ratio of the scattered intensity with this coherent behavior to the total scattered intensity is given by

$$\frac{I_s^{elas}}{I_s^{tot}} = \frac{\langle \hat{E}^-(t) \rangle \langle \hat{E}^+(t) \rangle}{\langle \hat{E}^-(t) \hat{E}^+(t) \rangle}. \quad (3.19)$$

This value approaches zero for purely chaotic light and is equal to unity for ideal coherent emission of a source. Taking the steady-state limit with infinite time-delay $\tau \rightarrow \infty$ we can further write

$$\frac{I_s^{elas}}{I_s^{tot}} = |g^{(1)}(\infty)|. \quad (3.20)$$

This general observation on the coherence of the scattered light applies to for all light sources, thus also for multilevel atoms with additional excited-state scattering.

In the case of a two-level system we can write Eq. (3.20) in simply terms of density matrix elements as [38]

$$\frac{I_s^{elas}}{I_s^{tot}} = \frac{|\rho_{21}(\infty)|^2}{\rho_{22}(\infty)}. \quad (3.21)$$

As is further shown by [45] the normalized averaged total scattered intensity of the fluorescence, neglecting Doppler broadening of the energy levels, as a function of the Rabi frequency Ω , the laser detuning Δ and the natural linewidth Γ is expressed as

$$I_{tot} = \frac{\Omega^2/4}{\Delta^2 + \Gamma^2/4 + \Omega^2/2}, \quad (3.22)$$

which can be decomposed into the sum of the individual intensities of the elastically and inelastically scattered part as

$$\begin{aligned} I_{elas} &= \frac{1}{2} \left[\frac{\Delta^2 + \Gamma^2/4}{\Omega^2/2} + 2 + \frac{\Omega^2/2}{\Delta^2 + \Gamma^2/4} \right]^{-1} \\ I_{inelas} &= \frac{1}{2} \left[1 + \frac{\Delta^2 + \Gamma^2/4}{\Omega^2/2} \right]^{-2}. \end{aligned} \quad (3.23)$$

Figure 3.3 pictures the elastically and inelastically scattered intensity for the situation of resonant excitation ($\Delta = 0$) in dependence of the saturation parameter $S = \Omega/\Gamma$. The contributions are normalized to the total intensity as $I_{tot} = I_{elas} + I_{inelas}$ to give 0.5 at saturation ($S \gg 1$). As indicated in the inset of the figure starting from very low S (and thus Rabi frequencies) I_{elas} is proportional to S , whereas I_{inelas} is proportional to S^4 . Thus, in this regime the scattering process is mainly elastic. At higher S the elastically scattered intensity tends to decrease and the inelastic intensity dominates. While S increases further the inelastic part reaches asymptotically

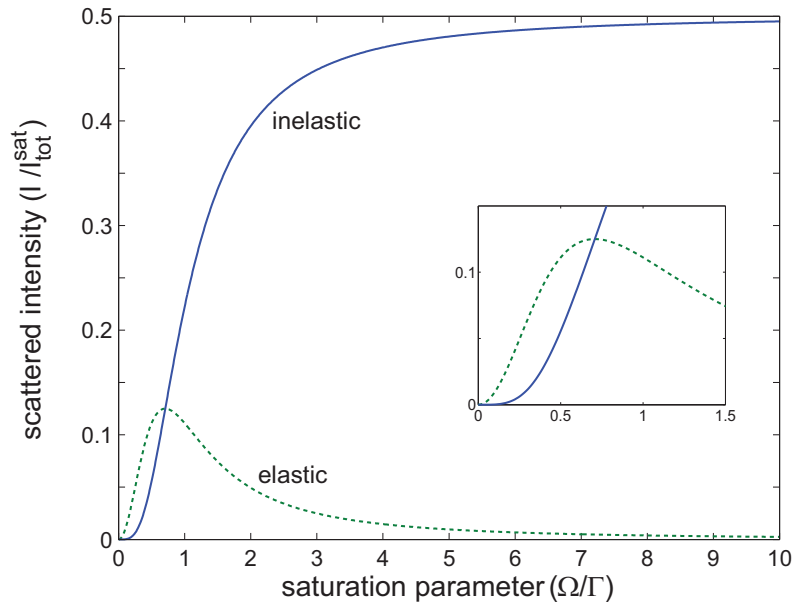


Figure 3.3: Normalized elastically (dotted line) and inelastically (solid line) scattered intensity as defined in Eq. (3.23) as a function of the saturation parameter.

0.5. This reflects the fact, that in a two level system the excited state population at saturation is maximally 0.5 and therefore the system can not emit more than $\Gamma/2$ photons per unit time.

All these conclusions presented for a two-level atom are also valid for multilevel systems, where the spectrum of a Ba^+ ion measured in the strong excitation regime of the 493 nm transition can be found in [46].

At this point we further note that the saturation parameter as defined in Eq. (2.29) is correct for the described two-level system at resonance but is not valid for a multilevel atom, where the individual Clebsch-Gordan coefficients have to be included in the respective Rabi-frequency.

3.1.3 $g^{(1)}(\tau)$ -function of an ion

In the case of a Ba^+ ion we have to consider the 8-level system as described in the previous chapter. Looking back to the level scheme from Fig. 2.2 for the green transition and considering our geometrical configuration (see Sec. 2.2.2), we note that the observed fluorescence actually consists of two transitions. Hence we can write the observable source parts of the radiated light field, in a rotating frame

picture at the laser frequency ω_L and in analogy to Eq. (3.13), as

$$\widehat{E}^+(t) = \xi e^{-i\omega_L t} \hat{\sigma}^-(t) \quad (3.24)$$

with

$$\hat{\sigma}^-(t) = \hat{\sigma}_{+1}^-(t) \vec{e}_{+1} + \hat{\sigma}_{-1}^-(t) \vec{e}_{-1} \quad (3.25)$$

and ξ denoting a constant amplitude. Here $\hat{\sigma}_{+1}^-(t)$ represents the Pauli lowering operator from the $|P_{1/2}, m = -1/2\rangle \rightarrow |S_{1/2}, m = +1/2\rangle$ state associated with the creation of a single $\Delta m = +1$ photon and $\hat{\sigma}_{-1}^-(t)$ represents the Pauli lowering operator from the $|P_{1/2}, m = +1/2\rangle \rightarrow |S_{1/2}, m = -1/2\rangle$ state associated with the creation of a single $\Delta m = -1$ photon. Further, $\vec{e}_{\pm 1}$ denotes the unit vector along the respective polarization of the created source field.

The first-order coherence is then gained by the detected intensity of the interfering electric fields given by Eq. (3.24, 3.25) as a function of a delay time τ between them by

$$\begin{aligned} G^{(1)}(t, t + \tau) &= \langle \widehat{E}^-(t) \widehat{E}^+(t + \tau) \rangle \\ &= \langle (\hat{\sigma}_{+1}^+(t) \vec{e}_{+1} + \hat{\sigma}_{-1}^+(t) \vec{e}_{-1}) \cdot (\hat{\sigma}_{+1}^-(t + \tau) \vec{e}_{+1} + \hat{\sigma}_{-1}^-(t + \tau) \vec{e}_{-1}) \rangle. \end{aligned} \quad (3.26)$$

Since the two involved transitions have orthogonal polarization ($\vec{e}_{+1} \perp \vec{e}_{-1}$) the equation simplifies to

$$G^{(1)}(t, t + \tau) = \langle \hat{\sigma}_{+1}^+(t) \hat{\sigma}_{+1}^-(t + \tau) + \hat{\sigma}_{-1}^+(t) \hat{\sigma}_{-1}^-(t + \tau) \rangle, \quad (3.27)$$

which is just the sum of the correlation functions of the two individual transitions. In the steady state limit $t \rightarrow \infty$, when the ion is statistically stationary, the correlation function can be written as a function of τ only and Eq. (3.27) reduces to a normalized form as

$$\begin{aligned} g^{(1)}(\tau) &= \frac{1}{2} \frac{\langle \hat{\sigma}_{+1}^+(t) \hat{\sigma}_{+1}^-(t + \tau) \rangle}{\langle \hat{\sigma}_{+1}^+(t) \hat{\sigma}_{+1}^-(t) \rangle} + \frac{1}{2} \frac{\langle \hat{\sigma}_{-1}^+(t) \hat{\sigma}_{-1}^-(t + \tau) \rangle}{\langle \hat{\sigma}_{-1}^+(t) \hat{\sigma}_{-1}^-(t) \rangle} \\ &= \frac{1}{2} [g_{+1}^{(1)}(\tau) + g_{-1}^{(1)}(\tau)]. \end{aligned} \quad (3.28)$$

We can now apply the density matrix formalism describing the ion's dynamic to express the first-order correlation function. Then, in steady state condition and using the preliminary step of Eq. (3.10) the first order coherence reads for positive τ values

$$g^{(1)}(\tau > 0) = \frac{1}{2} \frac{\text{Tr}[\hat{\sigma}_{+1}^- e^{\mathcal{L}\tau} (\hat{\rho}_{ss} \hat{\sigma}_{+1}^+)]}{\text{Tr}[\hat{\sigma}_{+1}^+ \hat{\sigma}_{+1}^- \hat{\rho}_{ss}]} + \frac{1}{2} \frac{\text{Tr}[\hat{\sigma}_{-1}^- e^{\mathcal{L}\tau} (\hat{\rho}_{ss} \hat{\sigma}_{-1}^+)]}{\text{Tr}[\hat{\sigma}_{-1}^+ \hat{\sigma}_{-1}^- \hat{\rho}_{ss}]}. \quad (3.29)$$

Considering the left side of Eq. (3.29) the correlation is initialized with the ion in steady state. The first multiplication of the Pauli operator $\hat{\sigma}_{+1}^+$ selects the respective

off-diagonal element in the density matrix. Then, by applying the time propagation operator, i.e. $\exp(\mathcal{L}\tau)$ given by Eq. (2.22), the system evolves to τ . The second multiplication of the complex conjugate operator $\hat{\sigma}_{+1}^-$ and tracing over the diagonal elements of the density matrix yields then the mean temporal coherence of the $\Delta m = +1$ dipole transition for the delay time τ .

In case of negative τ values the correlation is found by first multiplying $\hat{\sigma}_{\pm 1}^-$ to $\hat{\rho}_{ss}$, while keeping the normal ordering of the operators, as

$$g^{(1)}(\tau < 0) = \frac{1}{2} \frac{\text{Tr}[\hat{\sigma}_{+1}^+ e^{\mathcal{L}\tau} (\hat{\sigma}_{+1}^- \hat{\rho}_{ss})]}{\text{Tr}[\hat{\sigma}_{+1}^+ \hat{\sigma}_{+1}^- \hat{\rho}_{ss}]} + \frac{1}{2} \frac{\text{Tr}[\hat{\sigma}_{-1}^+ e^{\mathcal{L}\tau} (\hat{\sigma}_{-1}^- \hat{\rho}_{ss})]}{\text{Tr}[\hat{\sigma}_{-1}^+ \hat{\sigma}_{-1}^- \hat{\rho}_{ss}]}. \quad (3.30)$$

3.2 Second-order correlation function

The pioneer recording of the second-order correlation function marked the beginning of systematic studies of fluctuations of light. It was first carried out by R. Hanbury Brown and R. Q. Twiss, in 1956 [26,27] using spatially coherent light and star light. In a normalized form the second-order correlation is defined as [47]:

$$g^{(2)}(t, t + \tau) = \frac{\langle I(t + \tau)I(t) \rangle}{\langle I(t) \rangle^2} = \frac{\langle \hat{E}^-(t) \hat{E}^-(t + \tau) \hat{E}^+(t + \tau) \hat{E}^+(t) \rangle}{\langle \hat{E}^-(t + \tau) \hat{E}^+(t + \tau) \rangle \langle \hat{E}^-(t) \hat{E}^+(t) \rangle}, \quad (3.31)$$

yielding the normalized probability of detecting a photon at time $t + \tau$ given that one was detected at time t . If the emission properties of the light source are stationary in time, then in the steady-state limit $t \rightarrow \infty$ its second order correlation remains only a function of τ . The $g^{(2)}(\tau)$ can then be seen as a conditioned measurement of the detected photon intensity at times τ .

The measurement of this second-order coherence can be performed in a Hanbury-Brown and Twiss type setup as it is illustrated on the left side of Fig. 3.4. A beam splitter (BS) divides the light beam from a source into two parts that are subsequently sent to two photomultipliers (PMTs). The electronic signals from the PMTs correspond to photon detection events and are directed to a time correlator. Here, correlations are obtained by comparing the photon arrival times by successively binning their time differences. The experimental implementation of this technique is described in Sec. 5.2.2. Note that in principle the second-order coherence could be measured directly from the photocurrent of a single PMT, but the finite dead-time of the detector, typically on the order of tens of nanoseconds, would inhibit the observation of τ values within that dead-time window.

The time-evolution of a second order correlation function exhibits now distinguishable characteristics depending on the type of light source. The righthand side of Fig. 3.4 presents the $g^{(2)}(\tau)$ for three typical types of sources.

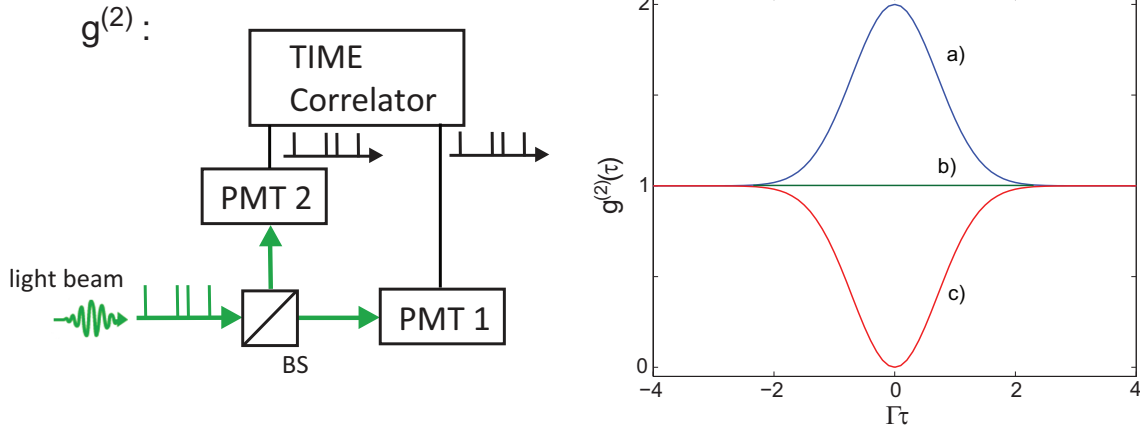


Figure 3.4: *Left*: Picture of a Hanbury Brown and Twiss type measurement setup. *Right*: Sketch of a second order correlation function for a) classical light with Gaussian frequency distribution, b) coherent light and c) non-classical light emitted by an ion (bottom).

Classical light

As was first investigated by Hanbury-Brown and Twiss [26,27] a continuous emitting classical light source, such as thermal light, exhibits the effect of "photon bunching", i.e. after a detection of a photon it is more likely to detect another one shortly afterwards. This property can be expressed in terms of an intensity fluctuation, or second-order coherence of the classical source, defining the intensity $I(t) = \langle I \rangle + \langle \delta I(t) \rangle$ with $\langle \delta I(t) \rangle = 0$, as

$$\begin{aligned} G^2(t, t + \tau) &= \langle I(t + \tau)I(t) \rangle = \langle I \rangle^2 + \langle \delta I(t + \tau)\delta I(t) \rangle \\ &\rightarrow \langle I \rangle^2 + \langle \delta I(t)^2 \rangle |_{\tau \rightarrow 0}. \end{aligned} \quad (3.32)$$

Here $\langle \delta I(t)^2 \rangle$ at the point $\tau = 0$ displays the variance of the intensity fluctuation, which always yields a positive value. Hence in a normalized form one expects to find Eq. (3.32) within the region $1 \leq g^{(2)}(\tau) \leq \infty$. Further, for a classical light source as described by Eq. (3.5) the first-order correlation is related to the second-order correlation as

$$g^{(2)}(\tau) = 1 + |g^{(1)}(\tau)|^2 \quad (3.33)$$

with the resulting value $g^{(2)}(0) = 2$. This equation is plotted as curve a) on the righthand side of Fig. 3.4.

Coherent light

In the limit of a coherent light field, such as featured by a laser with a classical electric field $E(t) = E_0 e^{i\omega t}$, no correlations between intensity fluctuations of the light are found. Here $g^{(2)}(\tau) = 1$ for all values of τ , illustrated in curve Fig. 3.4 b) .

Non-classical light

Assuming non vanishing beam intensities only a non-classical light source can be measured in the region $0 \leq g^{(2)}(0) < 1$ when continuously radiating, yielding to the effect of "photon anti-bunching" at $g^{(2)}(0) = 0$. This can be observed for example in the resonance fluorescence of single atoms [48–50] and requires a quantum mechanical treatment of the source. An anti-bunched statistics of a $g^{(2)}(\tau)$ is plotted in Fig. 3.4 c) and will be discussed in detail below.

3.2.1 Second-order coherence of a two-level system

Before investigating the $g^{(2)}(\tau)$ -function of an ion we consider again our two-level system. In this case the scattered fields exhibit the non-classical statistical property of anti-bunching. Employing Eq. (3.13) the second-order coherence is then given by the two-time average of the electric fields as [42]

$$\begin{aligned} G^{(2)}(t, t + \tau) &= \langle \hat{\mathcal{E}}^-(t) \hat{\mathcal{E}}^-(t + \tau) \hat{\mathcal{E}}^+(t + \tau) \hat{\mathcal{E}}^+(t) \rangle = \text{Tr}[\hat{\mathcal{E}}^+ \hat{\mathcal{E}}^- e^{\mathcal{L}\tau} \hat{\mathcal{E}}^- \rho(t) \hat{\mathcal{E}}^+] \\ &\propto \text{Tr}[\hat{\sigma}^+ \hat{\sigma}^- e^{\mathcal{L}\tau} \hat{\sigma}^- \hat{\rho}(t) \hat{\sigma}^+]. \end{aligned} \quad (3.34)$$

The result is plotted in Fig. 3.5 for two values of Ω/Γ . For a strong driving field, $\Omega \gg \Gamma$, the second-order coherence shows a damped oscillatory dependence on τ and approaches 1 for $\tau \rightarrow \infty$. In the weak excitation regime, $\Omega \ll \Gamma$, the $g^{(2)}(\tau)$ slowly increases with τ before asymptotically reaching the value 1.

3.2.2 $g^{(2)}(\tau)$ -function of an ion

We now consider a Ba^+ ion driven at the laser frequency, ω_L , emitting resonance fluorescence between the $|P_{1/2}\rangle \iff |S_{1/2}\rangle$ states. Intuitively, since after an emission process the atom is projected into the electronic ground state and hence needs some time to reabsorb and emit a second photon, the typical behavior of anti-bunching occurs in the vicinity of $\tau = 0$.

Hence, written in terms of the atomic operators, given by Eq. (3.24), and by applying the combined Pauli lowering operator from Eq. (3.25) the unnormalized

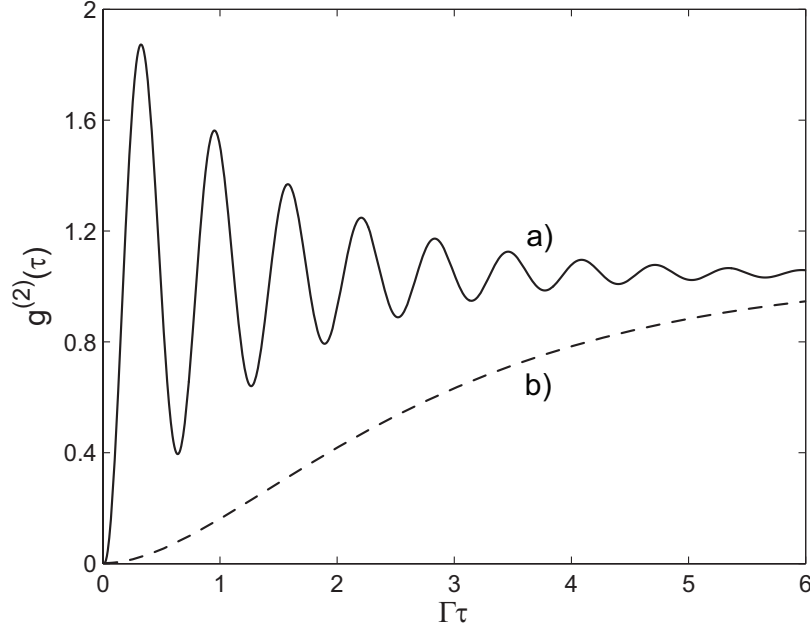


Figure 3.5: Plot of the normalized second order correlation function $g^{(2)}(\tau)$ of a two-level atomic system versus the dimensionless delay time $\Gamma\tau$ for a) (solid line) $\Omega/\Gamma = 10$ and b) (dashed line) $\Omega/\Gamma = 1/40$.

second-order correlation function yields in a matrix form for the limit $t \rightarrow \infty$

$$\begin{aligned}
 G^{(2)}(\tau) &= \langle \hat{E}^-(t) \cdot \hat{E}^-(t+\tau) \cdot \hat{E}^+(t+\tau) \cdot \hat{E}^+(t) \rangle \\
 &= \left\langle \begin{bmatrix} \hat{\sigma}_{+1}^+(t)\vec{e}_{+1} \\ \hat{\sigma}_{-1}^+(t)\vec{e}_{-1} \end{bmatrix} \cdot \begin{bmatrix} \hat{\sigma}_{+1}^+(t+\tau)\vec{e}_{+1} \\ \hat{\sigma}_{-1}^+(t+\tau)\vec{e}_{-1} \end{bmatrix} \cdot \begin{bmatrix} \hat{\sigma}_{-1}^-(t+\tau)\vec{e}_{-1} \\ \hat{\sigma}_{+1}^-(t+\tau)\vec{e}_{+1} \end{bmatrix} \cdot \begin{bmatrix} \hat{\sigma}_{+1}^-(t)\vec{e}_{+1} \\ \hat{\sigma}_{-1}^-(t)\vec{e}_{-1} \end{bmatrix} \right\rangle.
 \end{aligned} \tag{3.35}$$

When evaluating the scalar products and noting that $\vec{e}_{+1} \perp \vec{e}_{-1}$ the $g^{(2)}(\tau)$ hence consists of four individual correlation functions. Since we correlate photon detection events, unlike in the $g^{(1)}(\tau)$, cross-correlations between the two involved $|S_{1/2}\rangle \rightarrow |P_{1/2}\rangle$ transitions can occur. Note that the second order correlation function further obeys the property of time symmetry, i.e. $g^{(2)}(\tau > 0) = g^{(2)}(\tau < 0)$, and gives a value ≥ 0 for all τ .

Employing the quantum regression theorem the expectation values of the two-time correlations can be written in the density matrix formalism as

$$g^{(2)}(\tau) = \frac{\text{Tr}[(\hat{\sigma}_{+1}^+ \hat{\sigma}_{+1}^- + \hat{\sigma}_{-1}^+ \hat{\sigma}_{-1}^-) e^{\mathcal{L}\tau} (\hat{\sigma}_{+1}^- \hat{\rho}_{ss} \hat{\sigma}_{+1}^+ + \hat{\sigma}_{-1}^- \hat{\rho}_{ss} \hat{\sigma}_{-1}^+)]}{(\text{Tr}[(\hat{\sigma}_{+1}^+ \hat{\sigma}_{+1}^- + \hat{\sigma}_{-1}^+ \hat{\sigma}_{-1}^-) \hat{\rho}_{ss}])^2}. \tag{3.36}$$

In this equation the initial condition is given by the excited state populations in the limit of steady state, described by $\hat{\sigma}_{+1}^- \hat{\rho}_{ss} \hat{\sigma}_{+1}^+ + \hat{\sigma}_{-1}^- \hat{\rho}_{ss} \hat{\sigma}_{-1}^+$. This condition evolves then in time through τ using the time propagation operator. The expectation value of the second-order coherence is obtained by multiplying $\hat{\sigma}_{+1}^+ \hat{\sigma}_{+1}^- + \hat{\sigma}_{-1}^+ \hat{\sigma}_{-1}^-$ and computing the trace. The normalization is then found by division of the expectation value of the squared intensity at steady state.

The time-evolution of the excited state populations, as described in Eq. (3.36), can alternatively be expressed directly in terms of the associated diagonal elements of the density matrix $\hat{\rho}$. Adapting the notation of Fig. 2.2 the joint excited state population is then $\rho_{33} + \rho_{44}$, where $\rho_{33} = \hat{\sigma}_{+1}^- \hat{\rho} \hat{\sigma}_{+1}^+$ and $\rho_{44} = \hat{\sigma}_{-1}^- \hat{\rho} \hat{\sigma}_{-1}^+$ yield the connections to the atomic operators. Note that this notation was already derived in the previous chapter in Eq. (2.41) for the proportionality relation between the measured intensity and the excited state populations as $\langle I \rangle \propto \rho_{33} + \rho_{44}$. In the concept of a conditioned second order correlation it hence follows that

$$g^{(2)}(\tau) = \frac{\rho_{33}(\tau)_c + \rho_{44}(\tau)_c}{\rho_{33}(\infty) + \rho_{44}(\infty)}, \quad (3.37)$$

where the normalization is obtained in the steady-state limit of $\tau \rightarrow \infty$. The $g^{(2)}(\tau)$ hence maps the conditioned time evolution of the excited state populations conveyed in the diagonal elements of the density matrix.

Figure 3.6 depicts a second order correlation function for a single Ba^+ ion using Eq. (3.36) and 8-level Bloch equations. The $g^{(2)}(\tau)$ features clear anti-bunching at $\tau = 0$. The overshoot in the vicinity of $\tau \sim \pm 10$ ns is called optical nutation and relates to a higher probability of emitting a second photon at that time difference. Together with the followed smaller oscillations it represents the behavior of the damped Rabi oscillations between the $|S_{1/2}\rangle$ and $|P_{1/2}\rangle$ states. Its height scales with the intensities of the exciting laser fields and is mainly caused by the inelastically scattered part of the fluorescence.

Note that in the experiment a $g^{(2)}(\tau)$ function, besides extracting information of the internal dynamics of the ion, can further be used together with an excitation spectra to gain all relevant experimental parameters.

3.3 Intensity-field correlation function

So far we have considered the correlation function between two interfering fields and between two intensities. While in the $g^{(1)}$ -function the interfering parts of the radiation are detected as an intensity, in the $g^{(2)}$ -function we directly measure intensities and look at their time correlations.

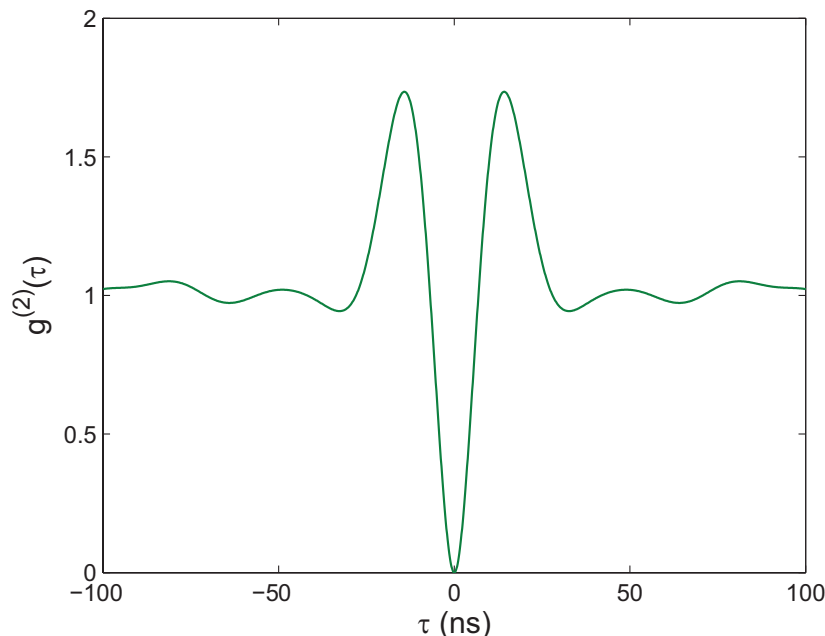


Figure 3.6: Calculated second-order correlation function using 8 level Bloch equations for a single Ba^+ ion with the parameters: $S_g = 0.8$, $S_r = 1.6$, $\Delta_g/2\pi = -30$ MHz, $\Delta_r/2\pi = 0$ MHz, $\delta_g/2\pi = \delta_r/2\pi = 50$ kHz, $u/2\pi = 4.2$ MHz, $\alpha = 90^\circ$.

We might want to ask now the question, if it is further possible to directly measure the source-field, thus the electric field corresponding to a single photon, and along with it its temporal evolution? Such information can indeed be extracted with the aid of a conditioned homodyne measurement, thus combining the techniques of an intensity correlation and a homodyne detector.

In a conventional homodyne setup the electromagnetic wave of a light source is coherently overlapped on a beam splitter with a wave of identical frequency from a local oscillator (LO). The resulting beat signal of the two light fields is then detected on a photodiode or PMT, whose photocurrent is then analyzed. For illustration we consider the electric field of the light source of one spectral component $E_S \cos(\omega_L t)$, where ω_L is the light frequency. The light field of the local oscillator $E_{LO} \cos(\omega_L t + \phi_{LO})$ shall have the same polarization and frequency but an adjustable phase ϕ_{LO} with respect to the phase of the fluorescence at the beam splitter. The resulting field is now a superposition of the two input fields and the detector after the beam splitter measures the intensity $I_{\text{Hom}} \propto [E_S E_{LO} \cos(\phi_{LO})]$. Hence, we can obtain information about the electric field fluctuations of the light source as a function of the phase

of a local oscillator. Note that in chapter 6 a detailed description of the homodyne signal is given using a quantum mechanical treatment of the beam splitter.

However, the random nature of the arrival times of the photons at the homodyne detector emitted from a light source does not permit us to extract any information so far on the temporal evolution of the electric source field acquired over many integration cycles. At this point we can make use of a conditioned measurement, in a similar way as described for the second-order correlation. In this concept of a conditional homodyne detection we trigger the homodyne signal I_{Hom} with a photon detection from the source I_S at yet another detector. We only look at the output of the homodyne detector when we know the light source has just emitted a photon. Because in this setup we correlate a photon detection with a field sensitive measurement we consider this technique as a measurement of an intensity-field correlation function. Moreover, since the correlation function of two fields is termed $g^{(1)}$ and that of two intensities is termed $g^{(2)}$, we accordingly "nick-name" the $g^{(1.5)}$ for this third-order correlation function of the field.

Figure 3.7 depicts a schematic setup for an intensity-field correlator. It is similar to the $g^{(2)}$ correlator with a start-stop scheme. The main difference is the homodyne detector, whose signal is used for the stop-channel. Summarizing, we can find a

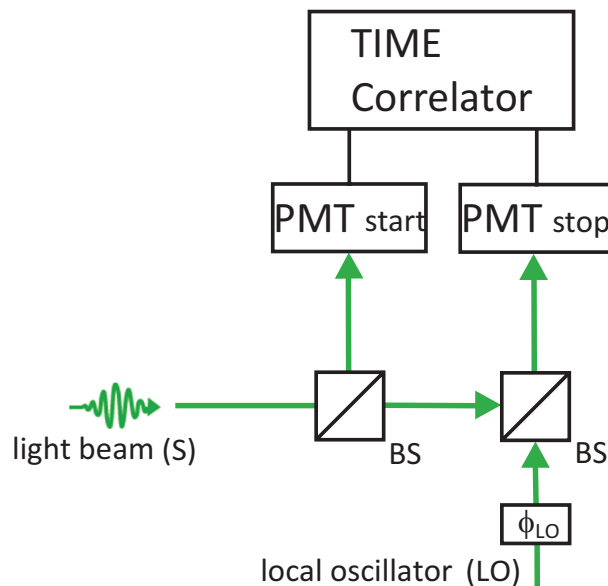


Figure 3.7: Schematic picture of a setup to measure an intensity-field correlation function.

general form of the third-order correlation function as

$$g^{(1.5)}(t, t + \tau) = \frac{\langle I_S(t) I_{\text{Hom}}(t + \tau) \rangle}{\langle I_S(t) I_{\text{Hom}}(t) \rangle} \propto \langle I_{\text{Hom}}(\tau) \rangle_c, \quad (3.38)$$

being proportional to a conditioned measurement of the homodyne signal at time τ . Written in atomic operators the expectation values of this two-time correlation is expressed in the density matrix formalism as

$$g^{(1.5)}(\tau) = \frac{\text{Tr}[\hat{\sigma}^- e^{\mathcal{L}\tau} (\hat{\sigma}^- \hat{\rho}_{ss} \hat{\sigma}^+)]}{\text{Tr}[\hat{\sigma}^+ \hat{\sigma}^- \hat{\rho}_{ss}] \text{Tr}[\hat{\sigma}^- \hat{\rho}_{ss}]}, \quad (3.39)$$

where the joint Pauli operator $\hat{\sigma}^-$ is given by Eq.(3.25). In analogy to Eq.(3.36) the correlation is initialized with a photon detection in steady state conditions described by $\hat{\sigma}^- \hat{\rho}_{ss} \hat{\sigma}^+$. After the evolution of the atomic system through time to τ a multiplication with a single $\hat{\sigma}^-$ represents the measured source field at the homodyne detector. Its expectation value is then found by taking the trace. To gain a dimensionless unit the correlation function is normalized by dividing through the mean values of the intensity times the field at steady state.

In chapter 7 the setup realized to measure the intensity-field correlation function from a single ion is presented in detail.

Chapter 4

Trapping of single atoms

The Paul trap, named after Wolfgang Paul almost 40 years ago, has since then emerged to become a major tool in quantum optics experiments with its possibility of storing single charged particles as ions. This trapping technique makes use of electrodynamic quadrupolar potentials and enables an effective way to store single ions over time scales of up to months and within micrometer confinement. The principle methodology and the geometric realizations in linear and ring-shaped Paul traps are discussed in the following chapter. Similar descriptions about ion-trapping can be found in [51–53].

4.1 The Paul-trap

In general, the principle of trapping atoms relies on a restoring force that holds the particles at one fixed position in space. In the case of charged atoms this can be realized by the design of electric fields. The trapping potential of a Paul trap consists of an electrodynamic part of amplitude V_{rf} at the radiofrequency Ω_{rf} and an electrostatic part V . They are then superimposed to yield a quadrupolar spatial shape in the trapping region of the trap. In Cartesian coordinates the combined potential is then given by

$$\Phi(x, y, z, t) = \frac{1}{2}[V + V_{\text{rf}} \cos(\Omega_{\text{rf}}t)] \sum_i \eta_i r_i^2 \quad , \quad i = x, y, z. \quad (4.1)$$

The potential has to fulfill the Laplace equation $\Delta\Phi = 0$ for every moment in time. This leads to the geometrical restriction that at least one of the spatial coefficients η_x, η_y, η_z has to be negative. The equation of motion for a particle with mass m and charge q in such a potential obeys the Mathieu differential equation

$$\frac{d^2 r_i}{d\zeta_i^2} + [\alpha_i - 2\beta_i \cos(2\zeta_i)]r_i = 0, \quad (4.2)$$

with $\zeta_i = \Omega_{\text{rf}}t/2$ and

$$\alpha_i = \frac{4qV\eta_i}{m\Omega_{\text{rf}}^2}, \quad \beta_i = \frac{2qV_{\text{rf}}\eta_i}{m\Omega_{\text{rf}}^2}. \quad (4.3)$$

The coefficients α_i, β_i hereby span a two-dimensional space of possible solutions of the differential equation. Stable trapping conditions can be found in lowest order approximation for the case where $\alpha_i \ll \beta_i \ll 1$. In this region the charged particles are bound in all three spatial directions and the particle trajectory is

$$r_i(t) \approx \left[1 - \frac{\beta_i}{2} \cos(\Omega_{\text{rf}} t)\right] \cos(\omega_i t + \psi_i) r_i^0, \quad (4.4)$$

where

$$\xi_i \approx \sqrt{\alpha_i + \frac{\beta_i^2}{2}}, \quad \omega_i = \frac{1}{2} \xi_i \Omega_{\text{rf}}. \quad (4.5)$$

Hence, the trajectory can be written consisting of two harmonic oscillating parts. The secular motion at the frequency ω_i and the micromotion, with a $\beta_i/2$ smaller amplitude, at the trap rf frequency Ω_{rf} . If the micromotion is assumed to be negligible the motion of the particle can be approximated by that of a harmonic oscillator moving in a pseudo-potential U

$$qU = \frac{1}{2} m \sum_i \omega_i^2 r_i^2. \quad (4.6)$$

So far we have treated the motion of a trapped particle classically. By applying the technique of laser cooling (see Sec. 5.3.3) trapped ions can be cooled to temperatures in the order of μK . In this regime it is necessary to describe the system using a quantum mechanical treatment of motion.

Let \hat{r}_i now be the position operator in the three Cartesian coordinates and \hat{p}_i the momentum operator of the particle. Assuming a potential that has a quadratic dependence in all directions the Hamiltonian is written as

$$H = \sum_i \left(\frac{\hat{p}_i^2}{2m} + \frac{1}{2} m \omega_i^2 \hat{r}_i^2 \right). \quad (4.7)$$

In the same way as with electromagnetic harmonic oscillator modes we can define an annihilation \hat{a} and creation \hat{a}^\dagger operator for one harmonic oscillation quanta in the trapping potential. The position and momentum operator are then expressed in terms of \hat{a} and \hat{a}^\dagger as

$$\hat{p}_i = i \sqrt{\frac{1}{2} m \hbar \omega_i} (\hat{a}_i^\dagger - \hat{a}_i) \quad (4.8)$$

$$\hat{r}_i = \sqrt{\frac{\hbar}{2m\omega_i}} (\hat{a}_i^\dagger + \hat{a}_i), \quad (4.9)$$

along with the Hamiltonian

$$H = \sum_i \hbar\omega_i \left(\hat{a}_i^\dagger \hat{a}_i + \frac{1}{2} \right). \quad (4.10)$$

The quantity of harmonical excitations, or phonon numbers, is then given by the number operator $\hat{n}_i = \hat{a}_i^\dagger \hat{a}_i$ with $|n\rangle = |0\rangle, |1\rangle, |2\rangle, \dots$ taking the energy values $E_{n,i} = \hbar\omega_i(n_i + 1/2)$. Further, the wave packet extension of a particular excitation quanta $\langle \hat{n} \rangle^2 = n$ is then given by

$$\sqrt{\langle n | \hat{r}_i^2 | n \rangle} = \sqrt{\frac{\hbar}{2m\omega_i}} \sqrt{2n+1}. \quad (4.11)$$

When we apply the atomic mass for a trapped barium ion of 138 u we obtain an extension of the motional wavepacket of the ion for the ground state $\sqrt{\langle 0 | \hat{r}_i^2 | 0 \rangle} \simeq 6$ nm. For a typical occupation number after Doppler cooling of $n = 20$ (discussed in Sec. 5.3.3) the spread is $\simeq 40$ nm.

4.1.1 The linear Paul trap

The linear trap employed in the laboratory consists of four blade shaped electrodes. The blades are at a radial distance of $r_0 = 0.7$ mm away from the trap center forming a two dimensional quadrupole potential. In the axial direction two end tips are located at a distance of $l = 2.2$ mm from the center. The ion is confined along this axis by applying a static voltage to both of the tip electrodes on the order of 1000 V. Note that this design is identical to a linear quadrupole mass filter with two additional end caps for axial confinement. Defining the radial plane as the x, y plane and the trap axis along z the trap potential hence reads:

$$\Phi_{\text{linear}} = \frac{V_{\text{rf}}}{2r_0^2} \cos(\Omega_{\text{rf}}t)(x^2 - y^2) - \frac{V_{\text{cap}}}{l} \left[\frac{1}{2}(x^2 + y^2) - z^2 \right]. \quad (4.12)$$

For a particle with the coordinates x, y, z the equations of motion in analogy to Eq. (4.2) are then given by

$$\frac{d^2}{d\zeta^2} x + [\alpha - 2\beta \cos(2\zeta)]x = 0 \quad (4.13)$$

$$\frac{d^2}{d\zeta^2} y + [\alpha + 2\beta \cos(2\zeta)]y = 0$$

$$\frac{d^2}{d\zeta^2} z - \frac{\alpha}{2}z = 0 \quad (4.14)$$

with $\zeta = \Omega_{\text{rf}}t/2$ and

$$\alpha = \frac{q\epsilon V_{\text{cap}}}{ml^2\Omega_{\text{rf}}^2}, \quad \beta = \frac{2qV_{\text{rf}}}{mr_0^2\Omega_{\text{rf}}^2}, \quad (4.15)$$

where ϵ is a numerical factor depending on the trap geometry. Typical stability values are $\beta < 0.5$ and $-0.05 < \alpha < 0.05$ [51]. Neglecting the micromotion and assuming a pseudo potential the particle's secular motion frequency around the trap center in the radial and axial direction are expressed as

$$\omega_r = \omega_x = \omega_y = \sqrt{\frac{\Omega_{\text{rf}}^2}{8}(\beta^2 - 2\alpha)}, \quad \omega_{ax} = \omega_z = \sqrt{\frac{q\epsilon V_{\text{cap}}}{2ml^2}}. \quad (4.16)$$

Whereas the axial secular frequency is only dominated by the geometrical factor α and the tip voltages the radial secular frequency is determined by both the static and the rf confinement. In the laboratory the linear trap is operated at $\Omega_{\text{rf}}/2\pi = 15.1$ MHz with an applied rf-amplitude of $V_{\text{rf}} = 1500$ V and a tip dc voltage of $V_{\text{cap}} = 2000$ V. The resulting calculated secular motion frequencies are $\omega_r/2\pi = 2.33$ MHz and $\omega_{ax}/2\pi = 1.05$ MHz. In the experiment the two radial modes have slightly different frequencies in the order of $\delta\omega_r \sim 30$ kHz. This splitting is introduced because of geometrical imperfections and the fact that the radiofrequency signal is only applied to two of the trap electrodes where the other two are grounded.

One advantage of the linear trap is that multiple ions can be stored along the trap axis for the usual case of $\omega_{ax} \ll \omega_r$. When sufficiently laser cooled the ions form a crystal, whose center of mass position follows the minimum of the trapping potential and is hence the same as for a single ion. From this center position the distance in axial direction Δl between two ion, defined by the trapping potential and the Coulomb repulsion, is then given by

$$\Delta l = \left(\frac{e^2}{\pi\epsilon_0 m\omega_{ax}^2} \right)^{1/3}. \quad (4.17)$$

Using typical values of $\omega_{ax}/(2\pi) = 1$ MHz and the barium mass this yields a spacing of $\Delta l = 3.7 \mu\text{m}$ between two ions.

4.1.2 The ring Paul trap

The second Ba^+ trap in the lab is a ring trap with a cylindrically symmetric rf-potential. It consists of a ring electrode with a radius of $r_0 = 0.7$ mm and two endcaps along the ring axis. The endcaps are at a distance of $z_0 = 0.7$ mm away from the center and form the ground potential ($V_{\text{cap}} = 0$). When x, y lie in the plane of the ring and z in the axial direction the trapping potential is given by

$$\Phi_{\text{ring}} = \frac{V_{\text{rf}}}{r_0^2 + 2z_0^2} \cos(\Omega_{\text{rf}}t) \left(x^2 + y^2 - \frac{1}{2}z^2 \right). \quad (4.18)$$

The trajectories of a particle along x, y, z in such potential are then governed by the three Mathieu type equations of motion

$$\frac{d^2}{d\zeta^2}x + 2\beta \cos(2\zeta)x = 0 \quad (4.19)$$

$$\frac{d^2}{d\zeta^2}y + 2\beta \cos(2\zeta)y = 0$$

$$\frac{d^2}{d\zeta^2}z - \beta \cos(2\zeta)z = 0 \quad (4.20)$$

with $\zeta = \Omega_{\text{rf}}t/2$ and

$$\beta = \frac{2qV_{\text{rf}}}{m(2r_0^2 + z_0^2)\Omega_{\text{rf}}^2}. \quad (4.21)$$

In the lowest stability region $\beta < 0.8$ the particle oscillates along the x, y, z direction with the frequencies

$$\omega_x = \omega_y = \frac{\omega_z}{2} = \frac{\beta\Omega_{\text{rf}}}{2\sqrt{2}}. \quad (4.22)$$

In the experiment the trap is operated at $\Omega_{\text{rf}}/2\pi = 19.3$ MHz with an rf-amplitude of $V_{\text{rf}} = 500$ V yielding typical secular frequencies in the vicinity of 1 MHz.

Chapter 5

Experimental setup and operation

The measurements reported in the succeeding chapters were performed using a laboratory setup consisting of two major components: A vacuum apparatus with a linear and a ring trap and a laser setup with 493 nm and 650 nm lasers for cooling, a 413 nm ionization laser and the light detection system. In Fig. 5.1 a schematic overview of these parts is illustrated. Its main workpieces will be discussed in detail in the upcoming sections.

At first, the vacuum setup is described starting with the linear and then the ring trap vessels. Then the laser systems and the light detection methods are specified. The chapter ends with a section discussing the necessary trap methodologies and laser cooling techniques.

5.1 Vacuum setup

In the laboratory two traps are operated, either separately in individual experiments or in a joint configuration. Each trap is situated in a UHV environment consisting of a steel vacuum vessel with view ports for optical access and a pressure inside at the order of 10^{-11} mbar. This pressure can be sustained (after bake-out and after removing the turbo pump) with an ion-getter-pump and a titanium-sublimation pump. In order to form a quadrupole potential a radiofrequency voltage is applied to either the ring electrode in the case of the ring-trap or to two out of four blade electrodes in the case of the linear trap. A detailed description of the trapping process can be found in Chap. 4. In both traps the high voltage is then achieved by the use of a helical resonator with a quality factor of typically $Q \simeq 300$. The resonator is driven by an rf synthesizer¹, which signal is amplified² to 5-10 W. The respective trap drive frequencies are $\Omega_{\text{rf}}/2\pi=19.3$ MHz for the ring trap and 15.1 MHz for the linear trap.

¹Rohde&Schwarz, SML01

²Mini Circuit, LZY-1

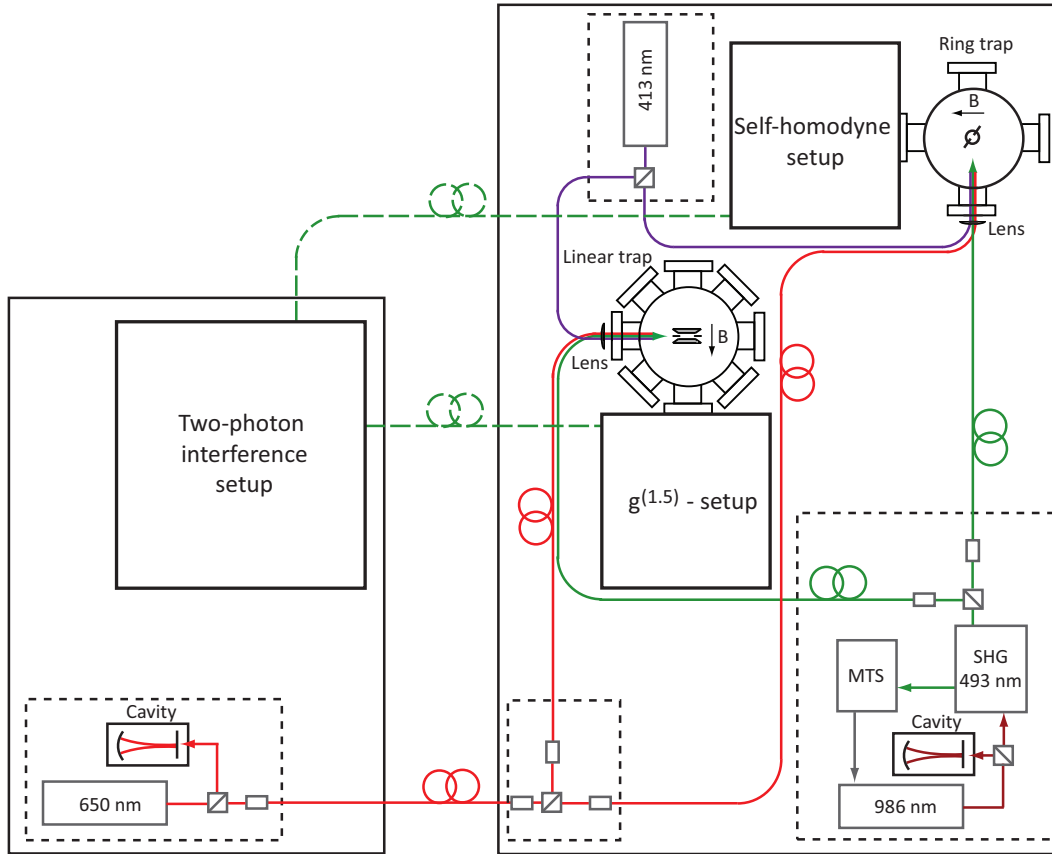


Figure 5.1: Sketch of the major laboratory components including the trap apparatuses, laser systems at 650 nm, 986 nm ($\times 2=493$ nm), 413 nm introduced in this chapter. Further, the indicated experimental blocks are marked, which are discussed in the following part of the thesis.

5.1.1 The linear trap

Figure 5.2 shows a schematics of the linear trap apparatus together with a picture of the actual setup. The trap is mounted on a large CF-200 flange, which is attached to an octagon steal vacuum vessel. For good optical access the main chamber offers one CF-200 viewport below the trap and seven CF-63 viewports in the horizontal plane of the trap. Furthermore, the solid CF-200 flange hosts three smaller CF-16 viewports. At one CF-63 flange a six-way cross is attached to the vessel that hosts

an ion-getter-pump³, a vacuum gauge⁴, a titanium sublimation pump⁵ and a vacuum valve⁶ to maintain the vacuum.

The magnetic field at the position of the ion is formed using three pairs of Helmholtz coils located in the horizontal plane each at 45° from the main beam hosted on the CF-63 flanges (coils 1 and 2) and on the vertical plane around the CF-200 flanges (coils 3).

The observation channels are situated perpendicular to the trap axis and parallel to the magnetic field. To collect fluorescence two custom-designed objectives⁷ are mounted on the left and right hand side ~ 12 mm away from the trap center. Each objective covers 4% of the total solid angle (NA=0.4) with a collimated beam diameter of 20 mm and a specified wave front distortion of $\lambda/10$. The objectives can be positioned with in-vacuum slip-stick piezo translation stages individually controlled by 3-axes piezo-mechanical actuators⁸, each with a travel distance of 5 mm and a resolution of 400 nm. In principle this allows for individual addressing of single ions. The objective on the left side of the trap is adjusted to focus the light to a CCD camera 300 mm away resulting in a magnification of 10. Alternatively, by rotation of the mirror (M_2) into the beam path the light can be reflected and after passing a slit iris⁹ it is focused onto a PMT. In front of the PMT an additional 50:50 BS can be inserted splitting the light to a second PMT to form a Hanbury-Brown and Twiss (HBT) type setup. Furthermore, spectral filters¹⁰ optimized for 493 nm are mounted in the light paths of both arms. The other objective located on the right hand side of the trap is adjusted at a distance of 11.8 mm to collimate the 493 nm fluorescence. Here various experimental setups can be mounted. For example, a piezo mounted mirror can be placed for back reflection of the light in a self-homodyne setup as described in Chap. 8. Alternatively a telescope can be inserted to scale the beam diameter to a smaller size suited for coupling the fluorescence into a single mode optical fiber¹¹.

To excite the ion the green and the red laser beams are first superimposed using a dichroic mirror (M_1), before they traverse a Glan-Thompson polarizer to guarantee vertical polarization. Then, the photoionization laser is mixed with the other two beams on a polarizing beam-splitter (PBS) and all lasers are focused onto the center of the trap with a $f = 250$ mm lens. The lens is optimized for the green light, while

³Varian, Star Cell 20 l

⁴Varian, UHV-24 Bayard-Alpert-Gauge

⁵Varian, TiSub

⁶VAT, all-metall valve

⁷Linos, HALO lens

⁸Attocube XYZ positioner, ANPxyz 100

⁹Owis, SP60

¹⁰Semrock, FF01-494/20-25

¹¹Thorlabs, PM-S405-HP with a Schäfter&Kirchhoff, 60FC-4-M15-13 coupler

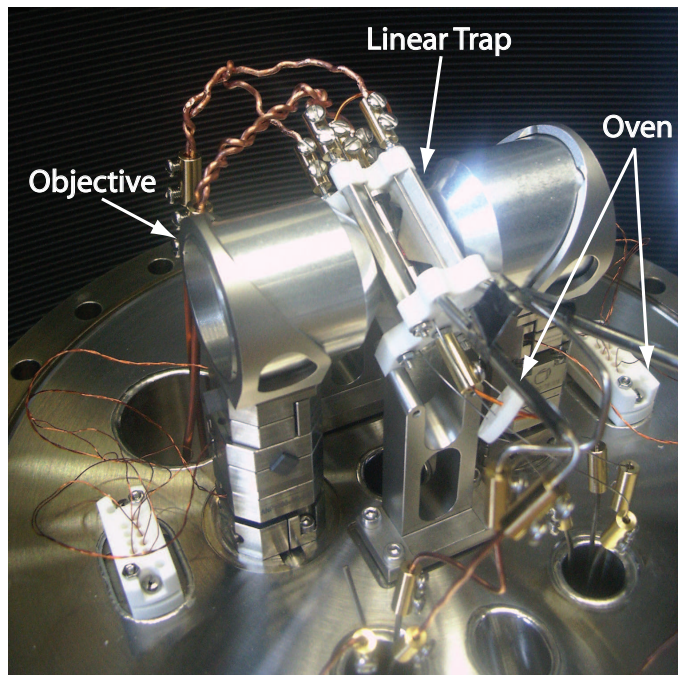
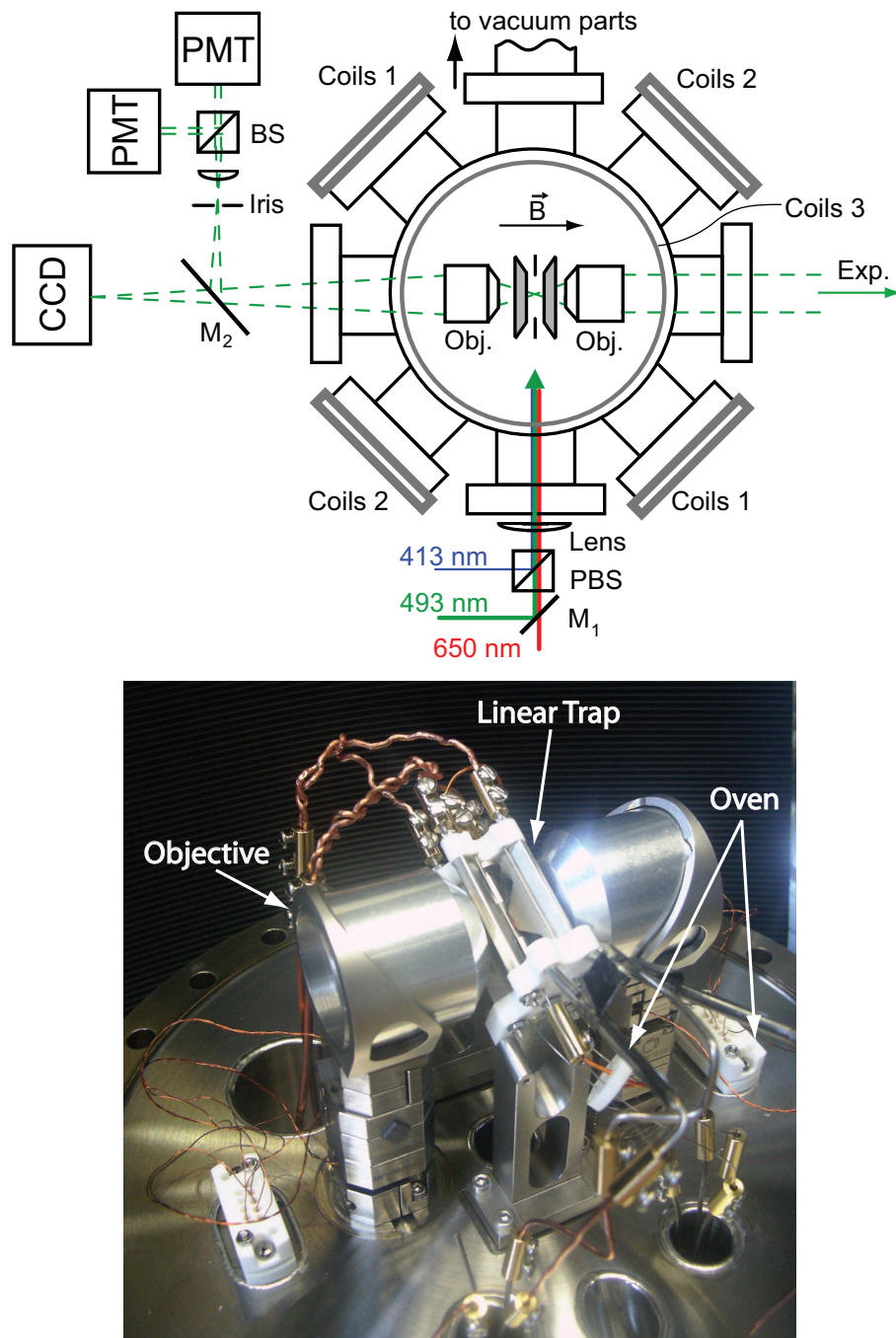


Figure 5.2: *Top graph:* Sketch of the linear trap system. The lasers are superimposed on M_1 and a PBS and are focused to the trap center. Fluorescence is collected on the left and right hand side of the trap using two objectives. The setup on the left hand side is used as the detection channel, where the light is alternatively guided using mirror M_2 to a CCD camera or to a HBT setup with two PMTs. The right hand side is used for further experimental setups. *Bottom graph:* Picture of the actual linear trap and objectives attached to the vacuum vessel. See text for details.

chromatic aberrations on the other beams are found to have no major influence on the performance of the experiments.

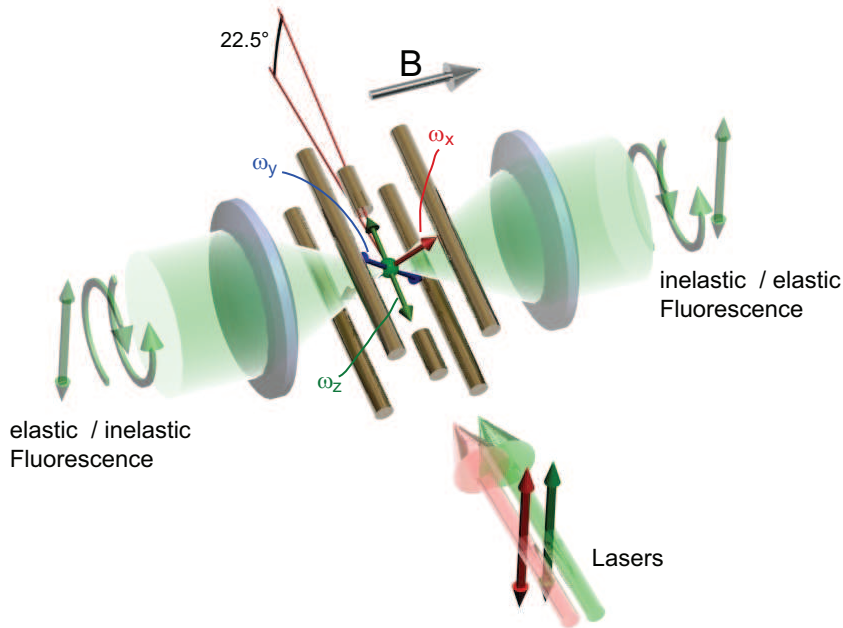


Figure 5.3: Sketch of the geometrical and optical configuration for the linear trap setup. Indicated are the respective polarizations of the light fields as arrows together with the directions of the ion's motional degrees of freedom. See text for details.

The linear trap itself consists of four blade shaped electrodes, on which two electrodes are connected to the rf source and two are grounded. The axial confinement is achieved with two tip electrodes connected to a dc voltage. Three additional pairs of dc-electrode wires are installed to compensate for micromotion located in the upper, lower segment of the trap and in one of the side segments. The method is explained in Sec. 5.3. All electrodes are held in place by two ceramic holders¹² which also provide a mount for two barium ovens pointing towards the trap center. In the resulting quadrupole pseudopotential the ions can be trapped for up to a week without laser cooling. The secular motion of the ions in the trap is hereby decomposed into three eigenmodes pointing along the trap axis. The x and y direction of the motion are along the radial direction of the trap towards the blade electrodes, where the z components points along the trap axis towards the endcap electrodes. At an rf power of

¹²Corning Inc., Macor

7 W the radial secular trap frequencies are measured to be $\omega_x/2\pi \simeq 1.675$ MHz and $\omega_y/2\pi \simeq 1.706$ MHz. To have proper Doppler cooling conditions, which is discussed later in Sec. 5.3.3, the lasers need to have projections to all of the three principal axis. This is ensured by a tilted trap axis of 22.5° pointing upwards with respect to the laser direction. The geometrical arrangement of the trap and the principal motions are hereby illustrated in Fig. 5.3. Furthermore, this picture shows the propagation and polarization directions of the lasers and the observed fluorescence. The linear polarized light of the laser is hereby scattered elastically or inelastically by the ion as discussed in Chap. 2. Note that further descriptions of the linear trap with its design parameters can be found in [54].

5.1.2 The ring trap

This part gives an overview of the ring trap setup. A more detailed description can be found in [55] and [52]. Figure 5.4 shows a sketch of the ring trap apparatus with its major components together with a picture of the zoomed-in ring trap setup.

The trap is housed in a steel vacuum vessel of spherical shape and grants optical access for laser addressing and observation of the fluorescence from several directions. The main laser beams are coupled into the trap through a tilted CF-150 viewport. Similar as in the linear trap all three lasers are overlapped using a dichroic mirror and a polarizing beam-splitter (PBS) and focused onto the center of the trap with a $f=250$ mm lens. Alternatively, three smaller CF-35 viewports allow for additional optical access. To maintain the vacuum inside the vessel an ion-getter-pump¹³, a titanium sublimation pump¹⁴ and a vacuum valve¹⁵ are attached to the spherical vessel.

Two CF-100 flanges along each side of the trap and perpendicular to the main excitation direction are used as the observation channels. The direction of the magnetic field at the trap center is aligned to be parallel with the observation axis using two pairs of coils. One viewport is inverted and houses an objective¹⁶ that covers $\sim 1.5\%$ of the solid angle (NA=0.24). The collected part of the fluorescence is then focused on an iris with 0.8 mm diameter and passes a spectral filter. With an effective magnification of 10 the light can then be sent to a CCD camera or to two PMTs in a HBT configuration. Further, a flip mirror can be inserted in the path and the 493 nm light can be coupled to a single mode optical fiber. The fluorescence collected at this viewport can further be directed to a macroscope type objective, where the observation of the trap region with the naked eye is possible. Along the

¹³Varian, Star Cell 20 l

¹⁴Varian, TiSub

¹⁵VAT, all-metall valve

¹⁶Wild Modell, M400

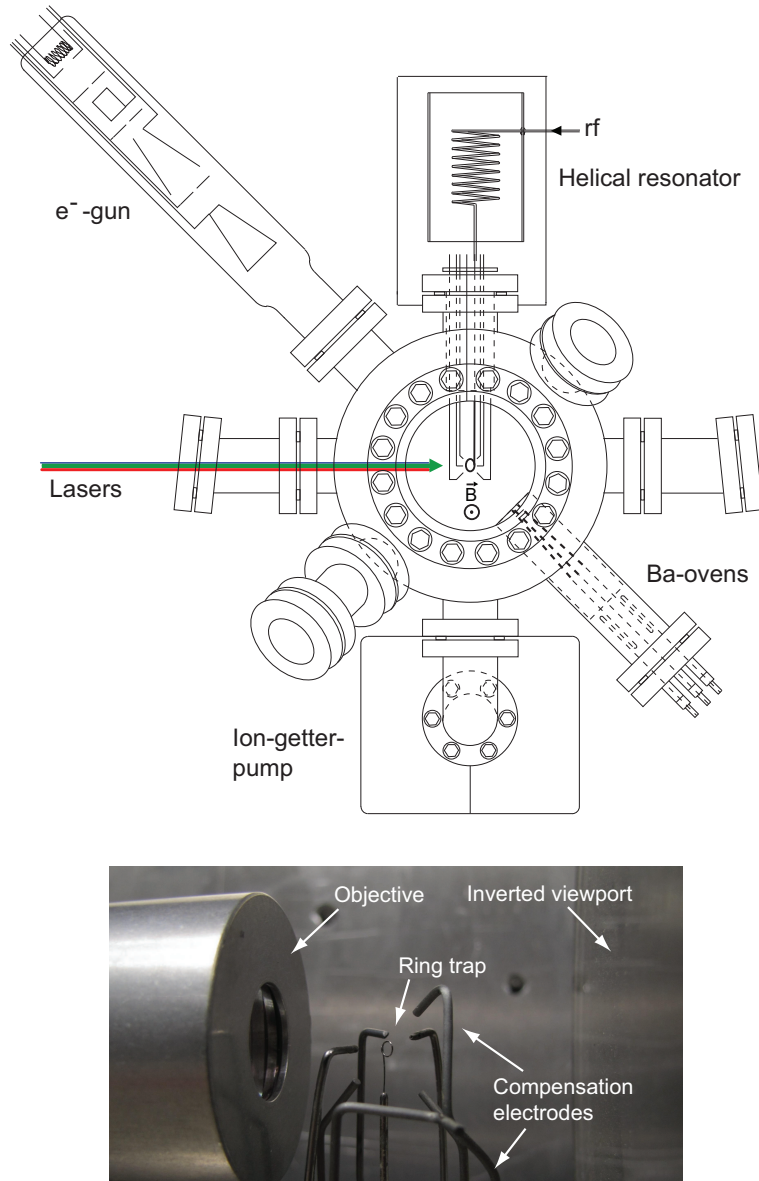


Figure 5.4: *Top graph:* Sketch of the ring trap setup. The vacuum vessel is shown from the perspective looking into the direction of the observation channels and \vec{B} -field. *Bottom graph:* Picture of the ring trap looking in the direction of the lasers. The in-vacuum objective is situated on the left and the inverted viewport, housing the in-air objective, is on the right.

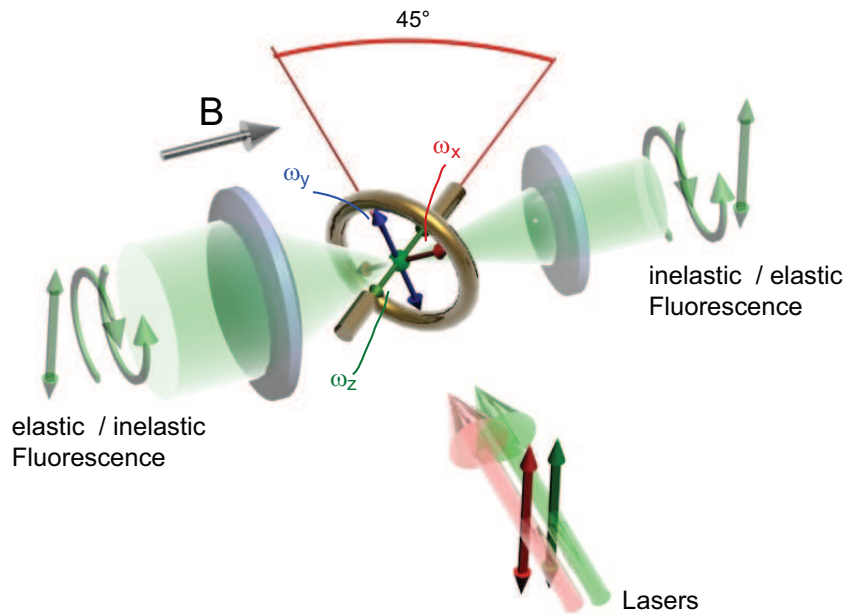


Figure 5.5: Sketch of the optical and geometrical arrangement for the ring trap setup. Indicated are the respective polarizations of the light fields as arrows together with the directions of the ion's motional degrees of freedom. See text for details.

same axis on the opposite side of the trap another objective is situated inside the vacuum vessel. This custom-made objective¹⁷ collects and collimates $\sim 4\%$ of the solid angle ($NA=0.4$) with a measured low wave front distortion smaller than $\lambda/10$. It can be aligned using three fine threaded screws pressing against the vacuum chamber. Here, similar as in the linear trap setup outside the vacuum a distant mirror or a telescope for fiber coupling can be mounted.

The ring trap itself is mounted on the top flange of the vacuum vessel and consists of a $200\ \mu\text{m}$ thick molybdenum wire with an inner diameter of 1.4 mm set to rf-potential. Along the radial axis 0.7 mm away from the trap center are the two grounded cap electrodes (see chapter 4). To compensate for micromotion at the drive frequency four additional electrodes are located 5 mm away from the ring. The resulting quadrupole potential has a depth of about 50 eV in which ions can be stored for a period of time up to a month. Two barium ovens point at the center of the trap as well as an electron gun with deflection optics.

In order to achieve optimal laser cooling along all principle modes of the secular

¹⁷Linos, Halo 25/04

motion the trap is tilted by 45° and is illustrated in Fig. 5.5. Here the respective secular frequencies in the x and y direction, lying in the radial plane, were measured to be $\omega_x/2\pi \simeq 1$ MHz and $\omega_y/2\pi \simeq 1.17$ MHz. The z component along the ring axis was found $\omega_z/2\pi \simeq 2$ MHz. These values hold for an applied rf-power of 5 W fed to the helical resonator. Figure 5.5 indicates the directions of the motional components as well as the optical configuration of the lasers and the observed fluorescence with their polarizations.

5.2 Laser setup

For Doppler cooling two diode laser systems together with an additional laser for photoionization are available in the lab. The lasers can be individually distributed to both traps, where a lab computer controls and monitors the laser frequencies. Further, the lab computer records the photocounts of each PMT. Below the individual laser systems and the light detection methods are elaborated in more detail.

5.2.1 Laser system

493 nm laser

For the dipole transition from the $|6S_{1/2}\rangle$ to the $|6P_{1/2}\rangle$ states the ions are excited with a laser system at 493 nm. The laser is based on a second harmonic generation (SHG) setup described in [55], where the master laser has been replaced by a commercially available diode laser¹⁸ with an output power of 130 mW at 986 nm. The master laser is stabilized to a reference cavity ($\mathcal{F} \approx 1000$) using the Pound-Drever-Hall technique [56]. From the width of the error signal during locking the master laser linewidth was measured to be ~ 20 kHz using a low noise PID controller¹⁹. A small part of the infrared light is then sent to a wavemeter²⁰, whose signal is monitored on the lab computer. Hereby, the wavemeter provides a real time observation of several wavelengths in parallel with an accuracy of ~ 10 MHz within several hours. From the rest of the infrared light second harmonic generation is performed in a bow-tie cavity resonant to 986 nm with a KNbO_3 crystal placed at one focus. The output power of the 493 nm light is then found to be ~ 30 mW. Against frequency drifts of the laser system the reference cavity is locked to a tellurium vapor (Te_2) cell by Doppler-free modulation transfer spectroscopy (MTS) [57]. In order to lock the laser to a suitable Te_2 resonance close to the 493 nm transition in Ba^+ some of the green light is frequency shifted by -500 MHz by a double pass

¹⁸Toptica, DL pro 986

¹⁹Toptica, FALC

²⁰Toptica, WS7

AOM. Fine tuning of the wavelength of the laser system towards the ion's resonance is performed by changing the double pass AOM's²¹ driving frequency with the lab computer by ± 30 MHz. The remaining light of the green laser is shifted $+140$ MHz by a single pass AOM²², on which the light is also intensity stabilized to 1% and directed to the individual traps by single mode polarization maintaining fibers.

650 nm laser

Repumping of the population from the metastable $|5D_{3/2}\rangle$ state to the $|6P_{1/2}\rangle$ state requires a light field at 650 nm. We generate light at this wavelength with a commercially available diode laser system²³ with an output power of 10 mW.

The laser light passes an AOM²⁴ in a double pass arrangement. The shifted light is used to lock the laser to a reference cavity ($\mathcal{F} \approx 1000$) with a linewidth of <100 kHz. The first order of the AOM is coupled into a single mode fiber²⁵ and guided to a distribution stage. Here the light is split and directed to the individual traps, where it is superimposed with the green laser. Furthermore, to constantly measure the wavelength, a small part of the red light after the first fiber is sent to the wavemeter.

413 nm laser

For photoionisation of neutral barium we employ a commercially available laser-diode system²⁶ generating light at 413 nm. The laser is operated in a Littrow-configuration and its wavelength is adjusted using the wavemeter. By inserting or removing a flip mirror the beam can be directed through air to one of the traps. After mode cleaning with a spatial filter the laser delivers a power of 2.5 mW to the trap center.

5.2.2 Light detection methods

In both traps fluorescence light emitted by the ions is collected with high numerical aperture objectives as described in the previous section. After filtering the fluorescence for the wavelength of 493 nm the light is either detected with photo-multiplier tubes²⁷ (PMT) or an electron-multiplying-CCD (EM-CCD) camera²⁸.

²¹Brimrose, EF-270-100

²²Crystal Tech, 3080-125

²³Toptica, DL 100

²⁴Crystal Tech, 3200-121

²⁵Thorlabs, PM-S630-HP with a Schwfter&Kirchhoff, 60FC-4-A6-13 coupler

²⁶Toptica, DL 100

²⁷Hamamatsu, H7421-40

²⁸Andor, Luca

In the latter case the CCD camera images the trapping zone which allows to spatially resolve single ions. At a magnification of 10 and a pixel size of $8 \times 8 \mu\text{m}$ the image from one ion appears as a point spread out over an area of about 4×4 pixels. The quantum efficiency at 493 nm is specified to be 51%.

In the other branch the PMTs record single fluorescence photons with a specified quantum efficiency of 40% at 493 nm and a dark count rate of ~ 75 cps. The intrinsic dead time after each photon detection is about 80 ns. Inside the PMT one impinging photon can create first a single electron (photoelectric effect) that successively triggers an avalanche of electrons, which can then be detected as a current pulse. The detected rate of pulses is hence proportional to the beam intensity for low intensities. In a quantum mechanical picture the measurement process can be regarded as a projection of the expanding wave function of the atomic radiation field at the position of the detector. It is this basis of a single photon detector that allows for a time resolved analysis of the recorded photon stream and the realization of all the performed experiments.

Note that because of the non-negligible dead time of the PMTs a detection setup consisting of two PMTs after a beam-splitter is required to extract time resolved information of the fluorescence light at the nanosecond time scale (HBT-setup see Sec. 3.2).

After a single photon detection event the resulting photo-electron pulse is then converted by the internal PMT electronics into a TTL pulse with a pulse length of 45 ns. The pulses are converted into NIM pulses²⁹ and pass a discriminator stage³⁰. At its output the pulses are split into three parts.

One part is fed into a photon counter³¹ followed by a time-to-digital converter³². The acquired count rate is then typically integrated over 100 ms and monitored on the LabVIEW controlling software. Another part of the discriminator's output can be investigated in the frequency domain with a spectrum analyzer³³. The third output of the discriminator

To furthermore extract statistical information contained in the emitted fluorescence the photocounts can be elaborated in a high resolution histogram counter³⁴ with a time resolution of $t_{res} = 4$ ps. The counter has two input channels, each able to monitor the signal pulses of one PMT. The individual detection arrival times are then recorded and stored in two time-ordered lists as $(l_0^1, l_1^1, \dots, l_i^1, \dots, l_n^1)$ and $(l_0^2, l_1^2, \dots, l_k^2, \dots, l_m^2)$. From these lists a histogram $H(\tau)$ of the time-differences can be

²⁹LeCroy, NT15

³⁰LeCroy, 821

³¹LeCroy, 3615

³²LeCroy, TDC 4204 and 3588 Histogram Memory

³³Rhode & Schwarz, FSP 13

³⁴PicoQuant, PicoHarp 300

calculated as:

$$H(\tau) \approx H(t_{ik}, t_{res}) = \sum_{i=0}^n \sum_{k=0}^m (l_i^1 - l_k^2). \quad (5.1)$$

Thus, all time differences (e.g. $t_{ik} = l_i^1 - l_k^2$) are evaluated, where each bin ik has a temporal width t_{res} and we denote $\tau = t_{ik}$. Additionally, $H(\tau)$ can be re-binned with a larger bin size δt_{bin} of typically 1 ns, which then yields the expression

$$H(t_{ik}, t_{res}, \delta t_{bin}) = \sum_{-\delta t_{bin}/2t_{res}}^{\delta t_{bin}/2t_{res}} H(t_{ik}, t_{res}). \quad (5.2)$$

The resulting cross-correlation is summed over larger binning times of width δt_{bin} . Further, note that the total number of cross-correlations obtained in this process is given by the multiplication of the total amount of detection events for each list as: $\sum_{i,k} H(\tau) = n m$.

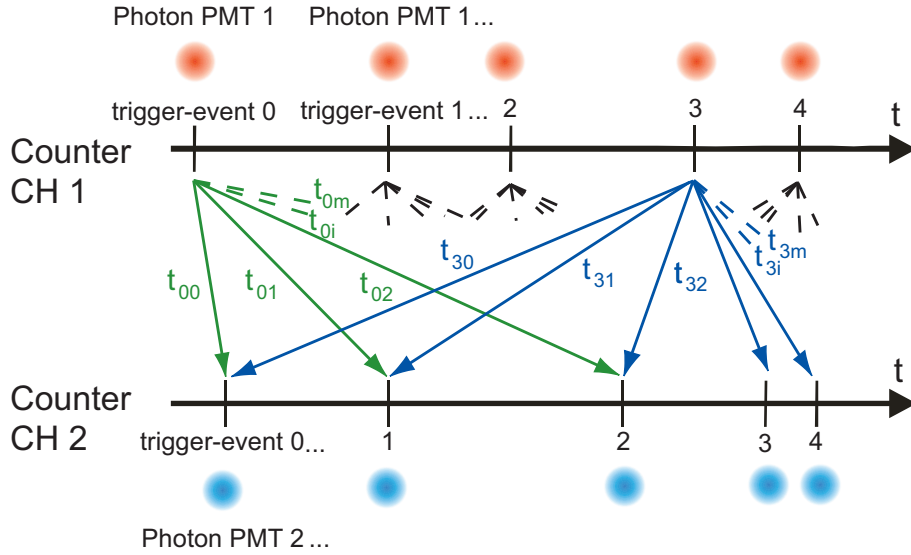


Figure 5.6: Acquiring cross-correlations between counted trigger-events from PMT 1 and PMT 2. The time differences of the trigger-events 0 and 3 of ch, 1 to trigger-events of ch. 2 are indicated as solid arrows. See text for details.

In Fig. 5.6 the process of obtaining a cross-correlation is illustrated. The photocounts of PMT 1 and 2 in a HBT-setup are recorded with a counter and listed in two time-ordered channels. After the data is obtained a histogram as described in Eq. (5.1) can be evaluated from the two lists. Starting from the first trigger-event of ch. 1 the time differences to all stored trigger-events of ch. 2 are calculated

$(t_{00}, t_{01}, \dots, t_{0i}, \dots, t_{0m})$. The obtained time differences are then binned and their occurrences stored in a histogram. These steps are subsequently repeated for the second trigger-event of counter ch. 1. The process is continued until all time differences between ch. 1 and ch. 2 have been evaluated. The binned histogram $H(\tau)$ is then identical to the unnormalized intensity correlation function as discussed in Sec. 3.2.

Additionally to the fluorescence photons emitted from an ion, a PMT may also be triggered by background noise. Such noise is comprised of residual stray-light from the 493 nm laser scattered on the trap electrodes as well as unfiltered light from the laboratory environment by the intrinsic dark count rate of the PMT. Since the 650 nm light is not detected by the PMTs the background rate is easily obtained by blocking the repumping 650 nm laser light so that the ion is trapped in the $|D_{3/2}\rangle$ state and stops fluorescing. The background rate can then be directly subtracted from the total count rate to obtain the fluorescence count rate from the ion. In the case of an intensity correlation function the background subtraction requires more post-processing of the data and is performed in the following way.

We consider the recorded signals from two PMTs used to deduce an intensity correlation function each PMT signal with a rate $s(t)$ incorporates a certain background noise rate $bg(t)$ and a fluorescence signal rate $s'(t)$. Thus, we can write $s_1(t) = s'_1(t) + bg_1(t)$ for the PMT 1 signal and $s_2(t) = s'_2(t) + bg_2(t)$ for the PMT 2 signal. Here, the time dependence of the background rate can be omitted in the case of a Poissonian noise distribution. This assumption was confirmed by measuring a flat correlation function in the case of pure background signal. The measured correlation function is then given by

$$h(\tau) = \frac{\langle [s'_1(t + \tau) + bg_1][s'_2(t) + bg_2] \rangle}{\langle s'_1(t) + bg_1 \rangle \langle s'_2(t) + bg_2 \rangle}. \quad (5.3)$$

Only the contribution $\langle s'_1(t + \tau)s'_2(t) \rangle$ will yield an intensity correlation function $g^{(2)}(\tau)$ of the ion and we can write the normalized form as

$$g^{(2)}(\tau) = \frac{h(\tau) - 1}{\left(1 - \frac{\langle bg_1 \rangle}{\langle s_1(t) \rangle}\right) \left(1 - \frac{\langle bg_2 \rangle}{\langle s_2(t) \rangle}\right)} + 1. \quad (5.4)$$

5.3 Experimental routines

In this section the basic techniques necessary to trap barium ions are explained. Starting with the loading process the experimental methodologies to minimize the micromotion and to operate the traps are discussed intended as hints for future daily lab routines. Similar operation procedures can be found in various previous works [52, 54, 58].

5.3.1 Trap loading

In order to trap a single ion the following procedures have proven valuable in the daily lab work.

First, the wavelengths of the lasers are coarsely adjusted using the wavemeter. Then the cooling lasers are locked to the Gaussian mode of the respective reference cavities. In case of the green laser the cavity is furthermore locked to the "big" Te_2 resonance [57] situated at about 493.410 nm (all wavelength values are measured in air) and the master laser is set to a far detuning value ($\Delta_g/2\pi \approx -200$ MHz) within LabVIEW. The red laser is tuned to a wavelength of about 649.6900 nm ($\Delta_r/2\pi \approx -40$ MHz) and the photoionization laser (PI) is tuned to 413.2430 nm on the wavemeter. Note that since the PI laser is not stabilized to a cavity its wavelength has to be slightly adjusted after about 20 min to compensate for slow drifts. Then, all three lasers are spatially overlapped in front of the trap before focusing into the trap center. The powers are adjusted to about 100 μW for the green, 150 μW for the red and to maximal 2.5 mW for the PI. The trap power is usually adjusted to a lower value of about 2 W.

Then the barium ovens can be heated, which is performed by applying a typical current of 3.4 A to one or both of the barium ovens. Usually Ba atoms are then photoionized and trapped into the center region within a few minutes. This time span is mainly needed for the ovens to heat up. Once a single ion is loaded the PI has to be blocked immediately and the oven current switched off, since once an ion is caught, it acts as a condensation core for further ions soon resulting in the trapping of several ions visible as a diffuse cloud. Note that should the position of the lasers be misaligned from the trap center, a cloud can often be used to readjust the beam positions.

When the required number of ions is loaded into the trap the trap power can be increased to a working point of 5 W for the ring trap and 8 W (tip voltage at 1000 V) for the linear trap.

After loading, the lasers may be tuned closer to resonance by first locking the green laser cavity to the "small" Te_2 resonance situated at a wavelength of the master laser of ~ 986.82050 and tuning its frequency close to about $\Delta_g/2\pi \approx -20$ MHz. Then the red laser is tuned and is tuned or fixed close to or at resonance. For cooling conditions the green laser power is lowered to yield about 1/3 of the maximal count rate and the red laser power is adjusted slightly below saturation.

5.3.2 Compensation of micromotion

With an ion loaded into the trap center the compensation of micromotion is an essential part for stable experimental conditions. As discussed in chapter 4 the

trajectory of a trapped ion in a quadrupolar trap constitutes of two parts, the secular motion due to the pseudo-potential and the micromotion oscillating at the trap rf-frequency. The amplitude of the latter increases linearly with the displacement of the trap center and can not be laser cooled. Micromotion hence leads to additional Doppler broadening of the dipole transitions resulting in a higher occupation of the motional state after Doppler cooling and needs to be minimized by shifting the ion into the zero position of the driving field. The displacement of the ion away from the center may arise due to geometrical imperfections, stray charges on the trap electrodes or slow drifts of the electrodes relative positions caused by different thermal expansions of the trap parts while operating.

Repositioning the ion towards the trap center is achieved by applying dc voltages to additionally installed compensation electrodes situated close to the trap in all three spatial directions. Observing the micromotion and the experimental routine for its compensation can be performed in three different ways.

In a first step of minimizing the micromotion the position of the ion is observed while the trap stiffness is varied. As the rf-power is increased the ion moves towards the center of the pseudo-harmonical potential, whose position can be marked on the CCD camera image. When the trap power is now lowered the voltages applied to the compensation electrodes can be changed in such a way that the ion is shifted back to the marked position. This method works well for two dimensions. To observe a change of the position in the third dimension along the camera axis the camera is moved out of focus, such that the ion is visible as a diffraction ring. A change in the diameter of the ring when lowering the trap power indicates a movement towards or away from the camera and thus can be compensated for.

The second method relies on a correlation measurement between the phase of the trap rf and the arrival times of the fluorescence photons [59]. Here, the laser detunings are adjusted slightly off-resonant to a point of a steep slope in the excitation spectra. At this laser settings, due to the Doppler shift, the oscillating ion will absorb and emit more or less photons when moving towards or away from the lasers, respectively. As the ion oscillates at the trap frequency the oscillation amplitude can be retrieved by correlating the rf signal with the photon arrival times. After a few seconds of integration the compensation voltages can be adjusted in such a way that any variance in the correlation is minimized.

A third method discloses the motional information of the ion via recording a $g^{(2)}(\tau)$ -function of the resonance fluorescence. The method is described in detail in [60]. An oscillation of the ion in the trap appears as a sinusoidal modulation of the correlation function considering a large span of τ . This method yields the most

sensitive way to visualize potential micromotion since no electronic noise or pick-up effect enters the optical signal combined with the possibility for a large integration time.

5.3.3 Laser cooling

As the technique of laser cooling of trapped ions constitutes an essential ingredient in the experiment its principle is briefly elaborated in this section. The aim of laser cooling is to reduce the kinetic energy of trapped ions from a thermal regime on the order of several hundred Kelvin towards a quantum regime of μK . There are several other comparative approaches available today to cool stored particles such as buffer gas cooling [61], Raman cooling [62] or stochastic cooling [63].

If the ion's oscillation frequency in the trap is smaller than the natural linewidth of the cooling transition the motional sidebands can not be resolved by the laser. The ion behaves like a free particle that is driven by a Doppler shifted laser frequency. The momentum of the ion can then be dissipated by radiation till the Doppler cooling limit [7, 64].

If the ion's oscillation frequency is larger than the natural linewidth of the cooling transition the laser can be tuned to the lower energy sideband. This regime is called side-band cooling [65], where it is possible to reach the motional ground state.

In this thesis only Doppler cooling is relevant, which is performed mainly via the green $|S_{1/2}\rangle \rightleftharpoons |P_{3/2}\rangle$ transition as indicated in Fig. 2.2. In the following the equilibrium temperature reached after Doppler cooling of a trapped ion is calculated.

It is sufficient to treat the ion as a two-level system ($|1\rangle$ and $|2\rangle$) with a certain initial temperature T and thus velocity \vec{v} interacting with a laser field along the wave vector direction \vec{k} . The laser is detuned from the transition frequency as $\Delta = \omega_{\text{laser}} - \omega_0$. Due to the Doppler shift the ion sees an effective laser frequency $\Delta_{\text{Doppler}} = \Delta - \vec{k} \cdot \vec{v}$. Then the average radiation force exerted by the laser is expressed as

$$F_{\text{rad}} = \frac{dp}{dt} = \hbar k \Gamma_{12} \rho_{22}. \quad (5.5)$$

Here, the absorption-emission cycle of that transition is determined by the decay rate Γ_{12} times the probability of being in the excited state ρ_{22} , which is given by

$$\rho_{22} = \frac{\Omega_{12}^2}{\Gamma_{12}^2 + 2\Omega_{12}^2 + 4\Delta_{\text{Doppler}}^2} \quad (5.6)$$

with Ω_{12} being the Rabi frequency on resonance. For small velocities we can now expand ρ_{22} around $v = 0$ and approximate by the linear term, which yields

$$\rho_{22} \approx \rho_{22}^0 + \frac{d\rho_{22}}{dv} v. \quad (5.7)$$

In terms of the radiation force this reads

$$F_{\text{rad}} \approx F_{\text{rad}}^0 [1 + \chi v] \quad (5.8)$$

with a time-constant part displacing the ion from the trap center and a velocity-dependent part with the "friction coefficient" χ as:

$$F_{\text{rad}}^0 = \frac{\hbar k \Gamma_{12} \Omega_{12}^2}{\Gamma_{12}^2 + 2\Omega_{12}^2 + 4\Delta^2}, \quad \chi = \frac{8k\Delta}{\Gamma_{12}^2 + 2\Omega_{12}^2 + 4\Delta^2}. \quad (5.9)$$

If the detuning Δ is negative χ can be interpreted as a viscous drag term.

The cooling rate is now provided by averaging the radiation force over many movements

$$\dot{R}_{\text{cool}} = \langle F_{\text{rad}} v \rangle = F_{\text{rad}}^0 \chi \langle v^2 \rangle. \quad (5.10)$$

Competing against this cooling rate is the spontaneous emission process as a heating rate. Since this process can be assumed to be uniform in space it results in a redistribution process of the averaged momentum $\langle p^2 \rangle$, which is proportional to the number of emission cycles as $\frac{d}{dt} \langle p^2 \rangle \propto \hbar^2 k^2 \Gamma_{12} \rho_{22}$. The heating rate at the final temperature at $v = 0$ thus reads:

$$\dot{R}_{\text{heat}} = \frac{1}{2m} \frac{d}{dt} \langle p^2 \rangle = \frac{\hbar^2 k^2}{2m} \Gamma_{12} \rho_{22}(v = 0). \quad (5.11)$$

Due to the different directions of absorption and emission the heating rate is altered to $\dot{R}'_{\text{heat}} = \dot{R}_{\text{heat}}(1 + \kappa)$ with $\kappa = 2/5$ for linearly polarized dipole radiation [66]. At equilibrium the heating and cooling rate are equal ($\dot{R}'_{\text{heat}} = \dot{R}_{\text{cool}}$) leading to a final temperature

$$T = \frac{m \langle v^2 \rangle}{k_B} = \frac{\hbar}{16k_B} (1 + \kappa) \left[\frac{\Gamma_{12}^2}{\Delta} + \frac{2\Omega_{12}^2}{\Delta} + 4\Delta \right], \quad (5.12)$$

with k_B being the Boltzmann constant. For the performed experiments the thumb rule for optimal Doppler cooling parameters are $\Omega_{12} \approx \Gamma_{12}/3$ and $\Delta = \Gamma_{12}/2$ which yields a minimal temperature of

$$T_{\text{min}} \approx \frac{7}{18} \Gamma_{12} \frac{\hbar}{k_B}. \quad (5.13)$$

Note that to guarantee cooling of a trapped ion in all coordinate directions in the experiment the wave vector \vec{k} of the cooling laser is chosen to have projections along all three harmonic oscillation directions of the ion. In real experimental conditions the Doppler limit is slightly increased due to unwanted static potentials causing a not totally compensated micromotion.

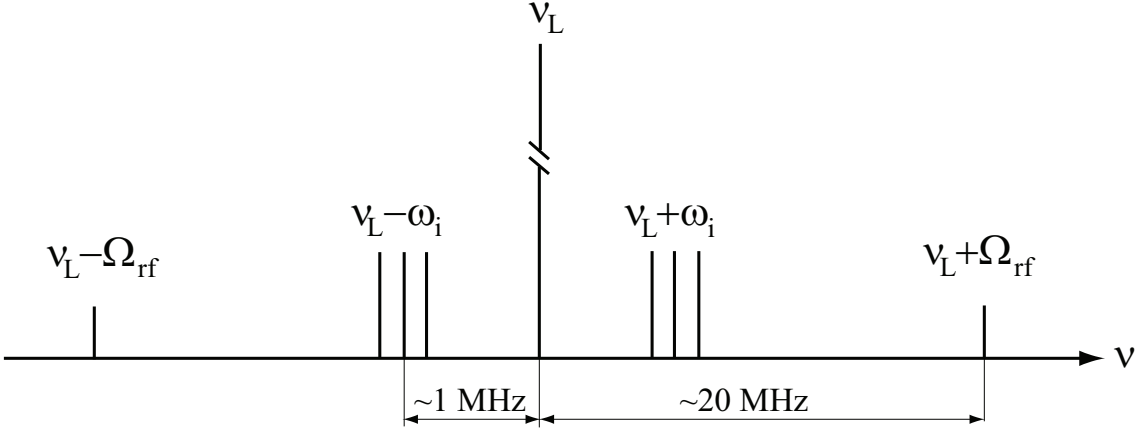


Figure 5.7: Spectrum of the resonance fluorescence of a trapped ion including its motion. The secular sidebands in the three Cartesian directions at $\xi_i \Omega_{\text{rf}}$, $i = x, y, z$ and the micromotional sideband at Ω_{rf} appear symmetrically around the atomic transition frequency ν_L .

5.3.4 Spectra of a trapped ion

In the previous chapters we have introduced the emission properties of a free atom interacting with a laser field as well as the technique of trapping ions in Paul traps. In this section we want to discuss how the emission properties are altered when we consider the motion of the trapped ion. Due to the motion of the ion in the trap the fluorescence is expected to be modulated and thus sidebands occur in the spectrum at the secular and micromotion frequency symmetrically around the transition frequency. Figure 5.7 shows a sketch of the spectrum emitted by a irradiated trapped ion. In the spectrum the three secular sidebands are situated around 1 MHz and the micromotion sideband is at the rf-drive frequency shifted from the central transition peak. Since the cooling transition from $|S_{1/2}\rangle$ to $|P_{3/2}\rangle$ has a natural line width of 15 MHz the sidebands are concealed within the carrier transition and are not directly observable. However, in the experimental part in Sec. 8.1 a method of revealing those sidebands with the aid of a self-homodyning technique is presented.

In order to calculate the transition strengths on the sidebands we start by recalling that the vibrational energy of the phonon state $\langle n \rangle$ is given by Eq. (4.10). We furthermore assume ideal compensation of the micromotion. The ion's secular motion with frequencies ω_i is then expressed as a harmonically oscillator along the principle directions $i = x, y, z$, where the position operator \hat{r}_i is given by Eq. (4.9) as $\hat{r}_i(t) = r_0(\hat{a}_i e^{-i\omega_i t} + \hat{a}_i^\dagger e^{i\omega_i t})$ [51]. Note that the indices $i = x, y, z$ hereby state the projections of the ion's radial and axial motional eigenmodes in the trapping

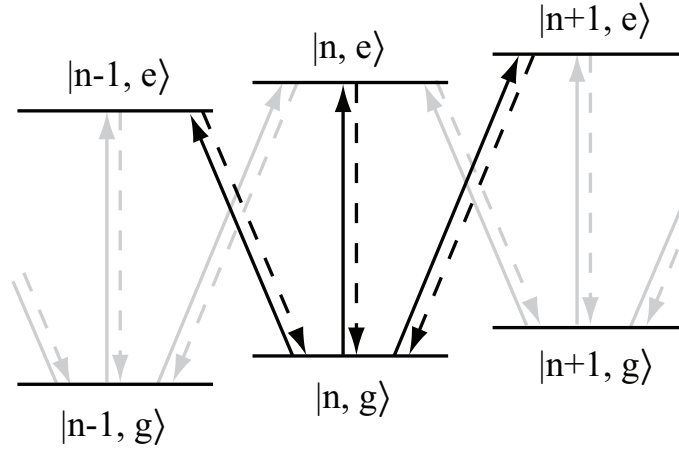


Figure 5.8: Level scheme of trapped ion in a harmonic potential coupled to a resonant laser field. The ion is initially in the electronic ground state $|g\rangle$ and at the motional quantum number $|n\rangle$. The carrier transition and the first order sideband transitions are shown, where the solid lines represent the absorption of a photon and the dashed lines indicate spontaneous decays [67].

potential along the observation channel direction. Further, \hat{a}_i and \hat{a}_i^\dagger are the bosonic creation and annihilation operator of one motional quantum as $\langle n_i \rangle = \langle \hat{a}_i^\dagger \hat{a}_i \rangle$ and \vec{k}_L is the associated transition wave vector.

We can now define the Lamb-Dicke parameter η as the ratio of the lowest wavepacket extension given by Eq. 4.11 to the wavelength of the atomic transition λ_L . This reads for one vibrational direction

$$\eta_i = \frac{\sqrt{\hbar/2m\omega_i}}{\lambda_L/2\pi}. \quad (5.14)$$

After laser cooling the ion is found in the so called Lamb-Dicke regime with $\eta_i \ll 1$. Here the wavepacket of the ion is smaller than the wavelength of the transition and it is possible to expand the position operator as

$$\exp(i\eta_i(\hat{a}_i^\dagger + \hat{a}_i)) = 1 + i\eta_i(\hat{a}_i^\dagger + \hat{a}_i) + O(\eta_i^2). \quad (5.15)$$

In this regime we can assume that only changes in the vibrational quanta by one are relevant and can be observed in the fluorescence spectra. Hence, for each vibrational mode we can distinguish between three possible transitions with different frequencies, i.e. the carrier transition with no change of the vibrational quanta centered at ν_L and a red and a blue sideband, changing the motional state by minus or plus one, respectively, located at $\nu_L \pm \omega_i$ symmetrically around the carrier. The

strength of the individual transitions compared to the overall Rabi frequency Ω is then determined by the Lamb-Dicke parameter and the vibrational state. It yields for the carrier transition [68]

$$\Omega_{n,n} = \Omega(1 - \eta^2 n) \quad (5.16)$$

and for the red and the blue sideband transition

$$\Omega_{n,n-1} = \Omega\eta\sqrt{n}, \quad (5.17)$$

$$\Omega_{n,n+1} = \Omega\eta\sqrt{n+1}, \quad (5.18)$$

where $\Omega_{n,n\pm 1} = \Omega_{n\pm 1,n}$. Figure 5.8 depicts the three considered transitions starting from the initial level $|n, 0\rangle$.

The widths of the described sideband transitions reflect the laser cooling rate, whereas the area under the sideband is proportional to the mean phonon number of the respective motional state. This is further treated in [58, 69].

5.3.5 Calibration of the setup

Chapter 2 discusses the excitation spectra of a single laser cooled ion. Considering the geometrical configuration of the trap its shape then reveals four dark resonances. As was mentioned the spectra are especially interesting due to their sensitivity to all experimental parameters, which can be extracted with the aid of a theoretical fit. When parameters as the magnetic field strength and direction are fixed a second order correlation function can be additionally used, as in most performed experiments, to gain information about laser detunings and intensities and to calibrate these parameters. Figure 5.9 depicts a measured excitation spectrum of a single Ba^+ ion located in the ring trap. The solid line represents the theoretical prediction using the Bloch equation model.

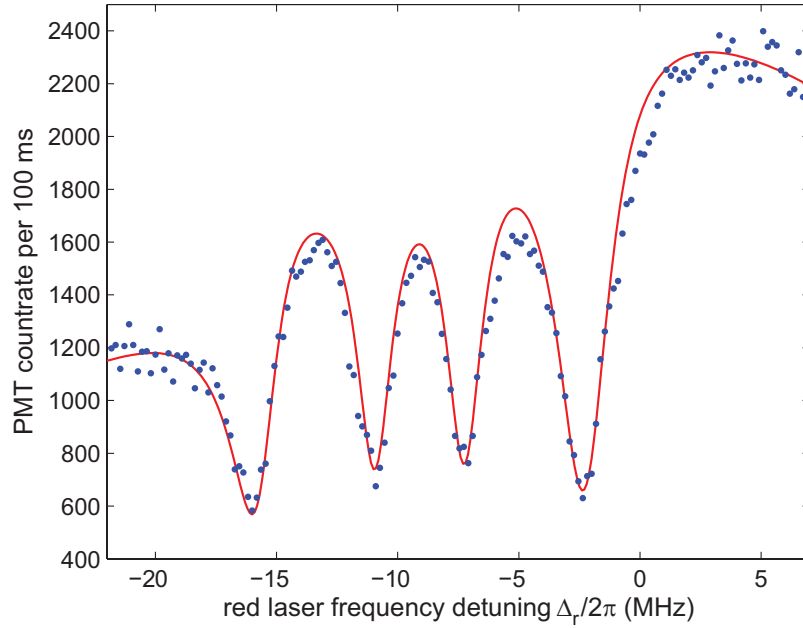


Figure 5.9: Excitation spectrum of a barium ion measuring the 493 nm fluorescence. The solid line represents the fit obtained with 8-level Bloch equations with the setup parameters as described in Sec. 2.2.2: $S_g = 0.72$, $S_r = 2.98$, $\Delta_g/2\pi = -9.1$ MHz, $\delta_g/2\pi = \delta_r/2\pi = 100$ kHz, $u/2\pi = 3.1$ MHz, $\alpha = 90^\circ$.

Chapter 6

Two photon interference

The following chapter discusses the two-photon interference between two remotely trapped Ba^+ ions. In this experiment the fluorescence light of each ion is collected and superimposed on a beam splitter with a maximal contrast of the photon's indistinguishability of 89(2)%. Furthermore, the coherence of the resonance fluorescence light field is determined from the observed interference.

Interfacing stationary qubits with quantum communication channels is currently at the focus of many research efforts with a goal towards the realization of quantum networks. In this picture ion traps may represent the nodes of a quantum network, while communication between remote nodes may be realized through photonic channels transmitting quantum states and entanglement [14]. Recently multiple experiments have addressed the realization of an atom-photon qubit interface and its fundamental components. Studies were performed with various systems, including atom-cavity devices [23–25, 70–73], atomic ensembles [74–77], and single trapped atoms or ions [22, 78, 80, 81, 84]. For the case of single trapped particles investigations have been made using single-photon interference between two ions in the same trap and continuously laser-excited [31, 82], interference between photons emitted by two atoms in distinct traps under pulsed laser-excitation [80], and two-photon interference between two ions located in remote traps along with pulsed laser excitation [81]. In the latter experiment a demonstration of distant entanglement between the two independently trapped ions was shown [22, 83].

The entanglement between two distinctly situated atomic systems can be achieved either through single- or two-photon interference. In the first case two indistinguishable scattering paths from two atomic sources are overlapped on a beam splitter. Both atoms are weakly excited such that only one photon is scattered in the system, whose detection yields an entanglement of the two sources [20]. In the second case a coincident detection of two photons after a beam splitter, where each photon is entangled with one of the atoms [84], projects the two atoms into an entangled state [21, 85, 86]. Here the realization of entanglement highly depends on the degree of indistinguishability of the two photons transmitting the quantum states. This

property can be efficiently characterized observing the interference of two superimposed light beams on a beam splitter and forms the topic of the current chapter.

In an earlier experiment using a similar setup a two-photon interference measurement was performed using a single ion as a pseudo two-photon source by splitting its resonance fluorescence, delaying part of it, and recombining both parts on a beam splitter. The indistinguishability of the photons of 83% was measured in a Hong-Ou-Mandel two-photon interference. This previous work is summarized in [78] and a detailed description is given in [54].

Since the entanglement methods using single- or two photon-interference rely on the interference of two light fields at a beam splitter, it is suitable to start this chapter with a theoretical description of such a device and its effect to classical as well as quantized light fields in Sec. 6.1.

Subsequently, in Sec. 6.2, the performed experiment is described showing two-photon interference between two remotely trapped Ba^+ ions. In this context the experimental setup is first introduced followed by a theoretical model. Concluding this chapter, the experimental results are discussed and summarized. The experiment presented here is published in [87] as a joint publication together with similar results obtained for Ca^+ ions elaborated in [88].

6.1 Interference at a beam splitter

A beam splitter is an optical device that reflects one part and transmits the other part of an incoming light beam. They form the central components in interferometer experiments and play important roles in various studies of quantum aspects of light.

6.1.1 Classical and quantum description of a beam splitter

Let us consider a beam splitter with two input fields \vec{E}_1 and \vec{E}_2 and two output fields \vec{E}_a and \vec{E}_b as shown in Fig. 6.1. For simplicity we will assume an ideal beam splitter with negligible absorption and diffraction losses. At the beam splitter the electric fields of the two input ports interfere, weighted by the transmission coefficient t and the reflection coefficient r , adding to the fields at the two output ports. This linear transformation can be written in a compact matrix form with complex coefficients as [89]

$$\begin{bmatrix} \vec{E}_a \\ \vec{E}_b \end{bmatrix} = \hat{B} \begin{bmatrix} \vec{E}_1 \\ \vec{E}_2 \end{bmatrix} \quad (6.1)$$

with

$$\hat{B} = \begin{bmatrix} r_1 & t_2 \\ t_1 & r_2 \end{bmatrix} = \begin{bmatrix} |r_1| e^{i\phi_1} & |t_2| e^{i\phi_2} \\ |t_1| e^{i\phi_3} & |r_2| e^{i\phi_4} \end{bmatrix}. \quad (6.2)$$

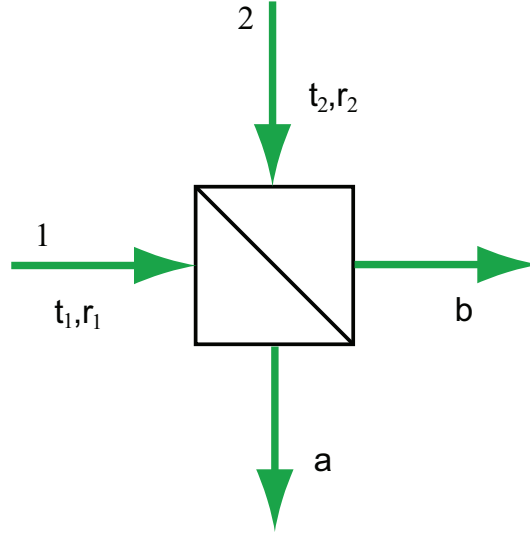


Figure 6.1: Geometrical arrangement of a beam splitter with input parts 1 and 2 and output ports a and b . Here r and t are the individual reflection and transmission coefficients.

Energy conservation of the two input and output fields require that

$$|\vec{E}_1|^2 + |\vec{E}_2|^2 = |\vec{E}_a|^2 + |\vec{E}_b|^2, \quad (6.3)$$

which yields for the coefficients of \hat{B} :

$$|r_1|^2 + |t_1|^2 = |r_2|^2 + |t_2|^2 = 1 \quad \text{and} \quad r_1 t_1^* = r_1 t_2^* = 0. \quad (6.4)$$

These equations are only fulfilled if the transmission and reflection coefficients for both input ports are equal. We can therefore write

$$\begin{aligned} |r_1| &= |r_2| = |r| & (6.5) \\ |t_1| &= |t_2| = |t| \\ |t|^2 + |r|^2 &= 1 \\ \phi_1 - \phi_2 - \phi_3 + \phi_4 &= \pi. \end{aligned}$$

Thus, the beam splitter is unitary. One possibility is to choose real values for the reflection and transmission coefficients. Since the phases do not have any effect on the measurement outcome we will choose from now on $\phi_1 = \phi_2 = \phi_4 = 0$, $\phi_3 = \pi$ or $\phi_1 = \phi_4 = 0$, $\phi_2 = \phi_3 = \pi/2$, which yields

$$\hat{B} = \begin{bmatrix} r & t \\ -t & r \end{bmatrix}. \quad (6.6)$$

For a 50:50 beam splitter furthermore the reflection and transmission coefficients are $r = t = 1/\sqrt{2}$ [90].

For the quantum mechanical treatment we replace the classical electric field vectors by operators. Let \hat{E}_1, \hat{E}_2 and \hat{E}_a, \hat{E}_b denote the annihilation operators for the beams entering and leaving the beam splitter, respectively. Because the transmission and reflection coefficients may depend on polarization and frequency we assume that the signal is carried by the complex amplitude of only one mode. The unitary transformation matrix as derived in the classical limit is still valid for describing the relation between the output and input operators as

$$\begin{bmatrix} \hat{E}_a \\ \hat{E}_b \end{bmatrix} = \hat{B} \begin{bmatrix} \hat{E}_1 \\ \hat{E}_2 \end{bmatrix}. \quad (6.7)$$

For photons the bosonic commutator rules hold as

$$\begin{aligned} [\hat{E}_1, \hat{E}_2^\dagger]_- &= 0 = [\hat{E}_2, \hat{E}_1^\dagger]_- \\ [\hat{E}_a, \hat{E}_b^\dagger]_- &= 0 = [\hat{E}_b, \hat{E}_a^\dagger]_- \\ [\hat{E}_i, \hat{E}_j^\dagger]_- &= \delta_{ij}, \end{aligned} \quad (6.8)$$

with $i, j = 1, 2, a, b$. Defining the photon number operator as $\hat{n}_i = \hat{E}_i^\dagger \hat{E}_i$ we can write down the relation for conservation of energy as

$$\hat{n}_1 + \hat{n}_2 = \hat{n}_a + \hat{n}_b. \quad (6.9)$$

Given now one photon at each input port the four possible situations occurring at the beam splitter are illustrated in Fig. 6.2. The mean photon flux at the output ports can then be calculated in the Heisenberg picture for the port a as

$$\begin{aligned} \langle \hat{n}_a \rangle &= \langle \hat{E}_a^\dagger \hat{E}_a \rangle = \langle (r \hat{E}_1^\dagger + t \hat{E}_2^\dagger)(r \hat{E}_1 + t \hat{E}_2) \rangle \\ &= t^2 \langle \hat{n}_2 \rangle + r^2 \langle \hat{n}_1 \rangle + tr \langle \hat{E}_1^\dagger \hat{E}_2 \rangle + rt \langle \hat{E}_1 \hat{E}_2^\dagger \rangle \end{aligned} \quad (6.10)$$

and similar for b as

$$\begin{aligned} \langle \hat{n}_b \rangle &= \langle \hat{E}_b^\dagger \hat{E}_b \rangle = \langle (-t \hat{E}_1^\dagger + r \hat{E}_2^\dagger)(-t \hat{E}_1 + r \hat{E}_2) \rangle \\ &= r^2 \langle \hat{n}_2 \rangle + t^2 \langle \hat{n}_1 \rangle - rt \langle \hat{E}_1^\dagger \hat{E}_2 \rangle - tr \langle \hat{E}_1 \hat{E}_2^\dagger \rangle \end{aligned} \quad (6.11)$$

with the last terms indicating the interference between the two input ports.

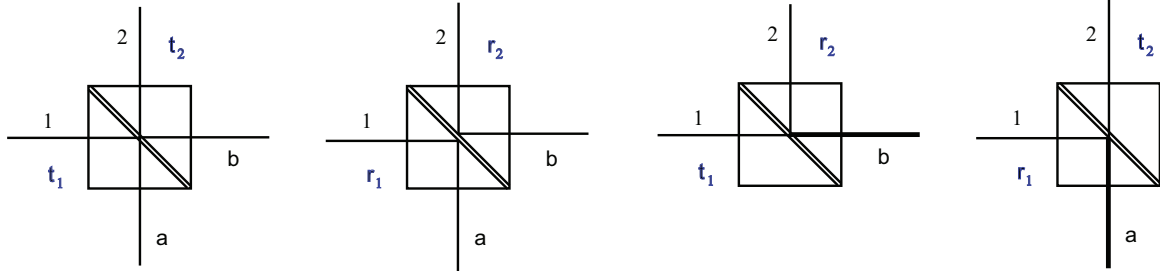


Figure 6.2: Sketch of the four possible situations that can occur at a beam splitter starting with one photon at each input port 1, 2. The output ports are labeled a , b .

6.1.2 Quantum interference and HOM-dip

The interesting case of quantum interference occurs when both of the input fields are in a one-photon Fock state. As originally described by Hong, Ou and Mandel [34] in experiments with starlight and spatially coherent light [26,27], two indistinguishable photons impinging simultaneously on each input port of a beam splitter coalesce, i.e. they will leave the beam splitter together in one of the two output modes.

Considering two indistinguishable photons at each input port we can deduce similarly as in Eq. (6.11,6.12) the joint probability of detecting a photon in both of the output beams as

$$\begin{aligned}
 P_{ab} &= \langle \hat{n}_a \hat{n}_b \rangle = \langle \hat{E}_a^\dagger \hat{E}_b^\dagger \hat{E}_b \hat{E}_a \rangle = \langle \hat{n} \rangle^2 (T^4 + R^4 - 2R^2 T^2) \\
 &\propto (T^2 - R^2)^2,
 \end{aligned} \tag{6.12}$$

which vanishes for a 50:50 beam splitter. The indistinguishability of the two input photons corresponds then to the generation of two-photon states and can be observed by a vanishing coincidence rate between the two output ports. Either both photons leave at port a or leave at port b .

This quantum interference effect for a two-photon state can be understood as follows. There are two different ways where one photon leaves port a and the other leaves port b . Either the two photons are both transmitted or reflected. With the two photons being indistinguishable these two situations cannot be distinguished. Hence, the two photons interfere and their probability amplitudes must be added. Due to the phase shift of the beam splitter associated with a reflection or a transmission

process, one of the probability amplitude exhibits a π phase shift with respect to the other and therefore the amplitudes cancel each other.

The visibility of the described two-photon interference is reduced, however, when the temporal or spatial overlap of the incident photon wave packets is only partial, such that the photons become distinguishable. This behavior is efficiently observed in measuring the so called Hong Ou Mandel dip (HOM-dip) using a second order correlation function. Here, two detectors monitor the time properties of the arriving photons at output ports where the second order coherence is given by Eq. (3.31) and is written as

$$g^{(2)}(\tau) \propto \langle \hat{E}_a^\dagger(t) \hat{E}_b^\dagger(t + \tau) \hat{E}_b(t + \tau) \hat{E}_a(t) \rangle. \quad (6.13)$$

When two perfectly identical photons impinge at the same time on the two input ports, the destructive interference is at a maximum and the coincidence rate of the detectors will drop to zero. If one of the photons is now slightly delayed in time a continuous increase in the coincidence rate is observed till one reaches the limit of fully distinguishable photon modes and the dip disappears completely. The shape of the dip is related to the first order coherence of the single-photon wave packet and hereby depends on the type of the light source. Figure 6.3 pictures the HOM-dip as it would show up for a typical down-conversion two-photon source with a Gaussian dip profile, whose width reflects the coherence length of the source [34]. In the

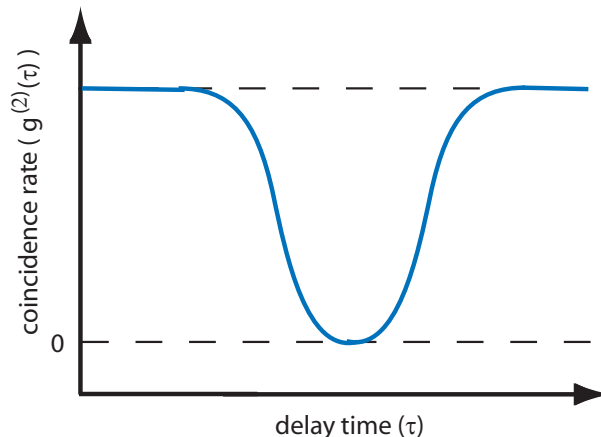


Figure 6.3: Sketch of a Hong Ou Mandel dip as coincidence rate of splitter outputs versus delay time between two identical input photons with a Gaussian wave packet.

following experiment the HOM-dip is presented for Ba^+ ions.

We briefly note at this point that for fermions, as particles under consideration, instead of Eq. 6.9 the anti-commutator relation holds as $\{b_i^\dagger, b_j^\dagger\}_+ = \delta_{ij}$ with the

consequence of observing for a two-particle interference at a beam splitter exactly the opposite effects as for bosons, i.e. a bunching effect in the HOM experiment.

Beam splitter as homodyne detector

The beam splitter also plays an important role when implementing a homodyne detector as it is required in the intensity field correlation setup introduced in Sec. 3.3. In this experiment, a phase sensitive measurement of the fluorescence field emitted from an ion is performed. In this homodyne setup one of the input fields is the signal field from the ion and on the other is a coherent light field serving as a local oscillator with the phase ϕ_{LO} and the complex amplitude \mathcal{A} , i.e. $\hat{E}_1 = \hat{E}_S$ and $\hat{E}_2 = \mathcal{A}e^{i\phi_{LO}}$. Substituting the input states into Eq. 6.11 yields for the photon flux at the beam splitter output a :

$$\begin{aligned}\langle \hat{n}_a \rangle &= t^2 \langle \hat{n}_2 \rangle + r^2 \langle \hat{n}_1 \rangle + rt \langle \hat{E}_2^\dagger \hat{E}_1 + \hat{E}_1^\dagger \hat{E}_2 \rangle \\ &= t^2 \langle \mathcal{A}^2 \rangle + r^2 \langle \hat{n}_S \rangle + rt \mathcal{A} \langle \hat{E}_S e^{-i\phi_{LO}} + \hat{E}_S^\dagger e^{i\phi_{LO}} \rangle.\end{aligned}\quad (6.14)$$

Similar for the output state b the expected photon flux is given by

$$\langle \hat{n}_b \rangle = r^2 \langle \mathcal{A}^2 \rangle + t^2 \langle \hat{n}_S \rangle - rt \mathcal{A} \langle \hat{E}_S e^{-i\phi_{LO}} + \hat{E}_S^\dagger e^{i\phi_{LO}} \rangle. \quad (6.15)$$

Hence, we can identify the last term as the typical quadrature operator of the electric field of the signal beam as

$$\hat{X}_\vartheta = \hat{E}_S e^{-i\vartheta} + \hat{E}_S^\dagger e^{i\vartheta} \quad (6.16)$$

with $\vartheta = \phi_{LO}$. By varying the phase of the local oscillator different quadratures of the signal can be measured.

In interferometric experiments often a balanced homodyne detector is used. In this case the detected photo currents from the two output ports are subtracted from each other, i.e. $S_{BH} \propto \langle \hat{n}_a - \hat{n}_b \rangle$ resulting in a direct observation of the quadrature operator proportional to

$$S_{BH} \propto \mathcal{A} \langle \hat{X}_\vartheta \rangle \quad (6.17)$$

for a 50:50 beam splitter.

6.2 Two photon interference between two remotely trapped ions

In this experiment we observe quantum interference of photons emitted by two distant Ba^+ ions independently trapped in distinct vacuum chambers. The ions

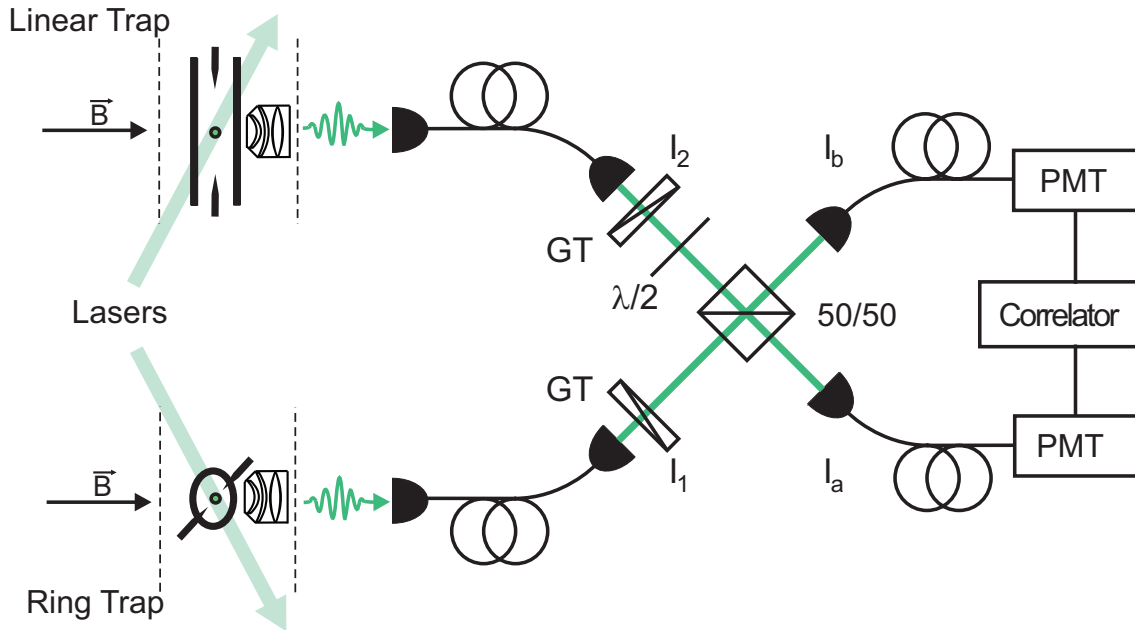


Figure 6.4: Sketch of the experimental setup. Resonance fluorescence photons emitted by each ion are collected with high NA lenses, coupled into single mode fibers and overlapped on a 50:50 beam splitter. Subsequently, second order correlation among photon detections are evaluated.

emit under continuous laser excitation, where their resonance fluorescence photons are collected by single-mode optical fibers and overlapped at two input ports of a beam splitter with the polarizations of the two input ports being controlled. Two detectors at the output ports correlate the arriving photons and the detection events are evaluated. As we will see below the recorded correlation further allows us to quantify the coherence of resonance fluorescence between two ions.

6.2.1 Experimental setup

The schematic experimental setup is depicted in Fig. 6.4. One single Ba^+ ion is loaded into the ring trap (ion 1) and a second ion into the linear trap (ion 2). The ions are continuously driven and laser-cooled by the same 493 nm (green) and 650 nm (red) lasers, where only the green fluorescence is used in the experiment. The experimental parameters for both traps are matched by comparing their excitation spectra and fitting individual $g^{(2)}$ -functions. With this techniques the emission properties of the two ions are adjusted to be identical. With the present geometrical configuration the ions hereby continuously emit left and right circular ($\Delta m \pm 1$)

polarized photons in direction of the observation channel as indicated by Eq. (3.24, 3.25). In each trap an objective collects 4% of the green resonance fluorescence. After passing a telescope for mode matching the light of each ion is coupled to single mode polarization maintaining (PM) optical fibers, where we record a count rate of ~ 25 kcps after each fiber. The photons are then guided to the entrance ports of a 50:50 beam splitter, labeled I_1 and I_2 corresponding to ion 1 and ion 2, respectively. The two output ports are denoted I_a and I_b . Before the beam splitter the polarizations of the two fiber outputs are controlled by Glan-Thompson polarizers (GT). Here, the polarization of the fluorescence from ion 1 is set to be horizontal, while the polarization of the fluorescence emitted by the second ion can be varied by an additional half wave-plate mounted after the polarizer. Hence, its projection of $\Delta m \pm 1$ polarized photons to a linear polarization halves the count rate for each ion at a gain of a well defined and controllable polarization of the ions fluorescence before the beam splitter.

The beam splitter output ports are again coupled into single mode fibers to guarantee optimum spatial mode matching. At the two outputs of the last fibers we then obtain a count rate at the detectors of ~ 6 kcps per ion. Optimizing the coupling efficiencies of this fiber-to-fiber interferometer the visibility is measured to be 97 % by sending laser light through the interferometer.

Correlations are obtained by subsequently monitoring the arrival times of the two PMTs in a Hanbury-Brown and Twiss type setup and calculating their time differences as described in Sec. 5.2.2.

6.2.2 Theoretical model

The theoretical description to quantify the two-photon interference for the current experimental configuration is based on the beam splitter formalism described in the beginning of this chapter. The corresponding electric fields of the two input ports of the beam splitter are labeled \hat{E}_1 and \hat{E}_2 , which are written in a linear (\vec{h} , \vec{v}) polarization basis. Fluorescence photons emitted on the $|P_{1/2}\rangle$ to $|S_{1/2}\rangle$ transition are then expressed in terms of the Pauli lowering operators from Eq. (3.25) for ion 1 and 2 as

$$\begin{aligned}\hat{\sigma}_1^- &= \hat{\sigma}_{1,+1}^- \vec{e}_{+1} + \hat{\sigma}_{1,-1}^- \vec{e}_{-1} \\ \hat{\sigma}_2^- &= \hat{\sigma}_{2,+1}^- \vec{e}_{+1} + \hat{\sigma}_{2,-1}^- \vec{e}_{-1},\end{aligned}\tag{6.18}$$

respectively. As realized in the experimental setup after the polarizers the now linear polarization of the fluorescence along \vec{h} is then expressed as a linear combination of the $\Delta m \pm 1$ polarization emitted by the ions using the relation:

$$\vec{e}_h = \frac{1}{\sqrt{2}}(\vec{e}_{+1} + \vec{e}_{-1}),\tag{6.19}$$

where \vec{e}_h denotes the unit vectors in \vec{h} direction. Thus, without loss of generality we fix the photon's polarization of the first ion at the port I_1 to be along \vec{h} . The photon's polarization of the second ion at I_2 is then rotated by the angle ϕ with respect to the \vec{h} direction. Combining Eq. (6.18) and Eq. (6.19) we can hence write for the electric field operator of ion 1

$$\begin{aligned}\widehat{E}_1(t) &\simeq e^{-i\omega_L t} [\hat{\sigma}_{1,+1}^- + \hat{\sigma}_{1,-1}^-] \vec{e}_h \\ &\simeq e^{-i\omega_L t} \hat{\sigma}_1^-(t) \vec{e}_h\end{aligned}\quad (6.20)$$

and respectively for ion 2

$$\begin{aligned}\widehat{E}_2(t) &\simeq e^{-i\omega_L t} \cos \phi [\hat{\sigma}_{2,+1}^- + \hat{\sigma}_{2,-1}^-] \vec{e}_h + \sin \phi [\hat{\sigma}_{2,+1}^- + \hat{\sigma}_{2,-1}^-] \vec{e}_v \\ &\simeq e^{-i\omega_L t} \hat{\sigma}_2^-(t) (\cos \phi \vec{e}_h + \sin \phi \vec{e}_v)\end{aligned}\quad (6.21)$$

with ω_L being the 493 nm transition wavelength. For an ideal 50:50 beam splitter the transmission (t) and reflection (r) coefficients are given according to Eq. (6.7) and (6.6). The field operators at the output arms then read

$$\begin{aligned}\widehat{E}_a(t) &\simeq \frac{1}{\sqrt{2}} e^{-i\omega_L t} \{ [\hat{\sigma}_1^-(t) e^{i\psi} + \cos \phi \hat{\sigma}_2^-(t)] \vec{e}_h + [\sin \phi \hat{\sigma}_2^-(t)] \vec{e}_v \} \\ \widehat{E}_b(t) &\simeq \frac{1}{\sqrt{2}} e^{-i\omega_L t} \{ [-\hat{\sigma}_1^-(t) e^{i\psi} + \cos \phi \hat{\sigma}_2^-(t)] \vec{e}_h + [\sin \phi \hat{\sigma}_2^-(t)] \vec{e}_v \}.\end{aligned}\quad (6.22)$$

Here ψ represents a random phase fluctuation between the electric fields emitted by the two ions. This is required, since the experimental setup does not ensure sub-wavelength mechanical stability.

The overall correlation function of the detected signals can then be expressed as

$$G_{\text{tot}}^{(2)}(t, t + \tau) \propto \sum_{(i,j)=\{h,v\}} \langle \widehat{E}_{a,i}^\dagger(t) \widehat{E}_{b,j}^\dagger(t + \tau) \widehat{E}_{b,j}(t + \tau) \widehat{E}_{a,i}(t) \rangle, \quad (6.23)$$

where $\widehat{E}_{(a,b),h}^\dagger$ and $\widehat{E}_{(a,b),v}^\dagger$ correspond to the part of the field $\widehat{E}_{(a,b)}^\dagger$ polarized along \vec{h} and \vec{v} , respectively. With the emission properties of ion 1 and 2 set to be identical and after averaging over all possible values of ψ these four terms can be evaluated to:

$$\begin{aligned}G_{\text{tot}}^{(2)}(t, t + \tau, \phi) &\propto \frac{1}{4} [\langle \hat{\sigma}_1^+(t) \hat{\sigma}_1^+(t + \tau) \hat{\sigma}_1^-(t + \tau) \hat{\sigma}_1^-(t) \rangle \\ &\quad + \langle \hat{\sigma}_2^+(t) \hat{\sigma}_2^+(t + \tau) \hat{\sigma}_2^-(t + \tau) \hat{\sigma}_2^-(t) \rangle \\ &\quad - 2 \cos^2(\phi) \langle \hat{\sigma}_1^+(t) \hat{\sigma}_1^-(t + \tau) \rangle \langle \hat{\sigma}_2^+(t + \tau) \hat{\sigma}_2^-(t) \rangle \\ &\quad + 2 \langle \hat{\sigma}_1^+(t + \tau) \hat{\sigma}_1^-(t + \tau) \rangle \langle \hat{\sigma}_2^+(t) \hat{\sigma}_2^-(t) \rangle].\end{aligned}\quad (6.24)$$

Identifying the individual contributions in Eq. (6.24) we find the first two terms representing second order correlations, $G^{(2)}$, between photons both emitted by the same ion, i.e. the first term contributed by ion 1 and the second term by ion 2. The third term expresses the interference between two photons emitted by different ions weighted by the polarization angle ϕ . This term can further be rewritten as the product of the individual first order correlation functions as $-2 \cos^2(\phi) [G_1^{(1)}(t, t + \tau) G_2^{(1)*}(t, t + \tau)]$. It represents the degree of indistinguishability of photons at the input ports of the beam splitter and thus vanishes in the case of $\phi = \pi/2$. The fourth term indicates the product of the mean number of photons $\langle n_1 \rangle \langle n_2 \rangle$ emitted by each ion. It reflects the level of random correlations between photons emitted by different ions. Under the assumption of identical emission properties for ion 1 and 2 we can now set $G_1^{(2)}(t, t + \tau) = G_2^{(2)}(t, t + \tau) = G^{(2)}(t, t + \tau)$ and $G_1^{(1)}(t, t + \tau) = G_2^{(1)}(t, t + \tau) = G^{(1)}(t, t + \tau)$ and further $\langle n_1 \rangle = \langle n_2 \rangle$. This simplifies Eq. (6.24) to the expression

$$G_{\text{tot}}^{(2)}(t, t + \tau, \phi) = \frac{1}{2} [G^{(2)}(t, t + \tau) - \cos^2(\phi) |G^{(1)}(t, t + \tau)|^2 + \langle n \rangle^2]. \quad (6.25)$$

In the steady state limit $t \rightarrow \infty$ the normalization of the measured correlation function is then given by $g_{\text{tot}}^{(2)}(\tau, \phi) = G_{\text{tot}}^{(2)}(\tau, \phi) / G_{\text{tot}}^{(2)}(\tau \rightarrow \infty, \phi)$ and we can write the normalized form as

$$g_{\text{tot}}^{(2)}(\tau, \phi) = \frac{1}{2} g^{(2)}(\tau) + \frac{1}{2} [1 - \cos^2(\phi) |g^{(1)}(\tau)|^2]. \quad (6.26)$$

In this correlation function the last term represents the two-photon interference contribution with an amplitude given by the coherence properties of interfering fields. The shape of the first order coherence $|g^{(1)}(\tau)|$ continuously decreases with τ , starting from $|g^{(1)}(0)| = 1$, with a time constant equal to the coherence time of resonance fluorescence photons (see Sec. 3.1). Hence, for $\tau \neq 0$, the individual coherence of interfering photons is revealed by subtracting the measured $g_{\text{tot}}^{(2)}$ correlation function. On the other hand, for the angle ϕ set to 0 and for $\tau = 0$, the coincidence rate for the total correlation function vanishes, due to the discrete character of photon emission by a single ion ($g^{(2)}(0) = 0$) and due to the two-photon interference with complete photon coalescence at the beam splitter.

6.2.3 Experimental results

First we measure the second-order correlation function, $g^{(2)}(\tau)$, of fluorescence photons emitted by one ion. For this we block one input channel of the 50:50 beam splitter. The obtained normalized $g^{(2)}(\tau)$ is then presented in Fig. 6.5 and exhibits an almost ideal anti-bunching ($g^{(2)}(0) = 0.03$ without background subtraction) and an optical nutation of $g^{(2)}(13 \text{ ns}) = 2.9$. This data was obtained with an accumulation

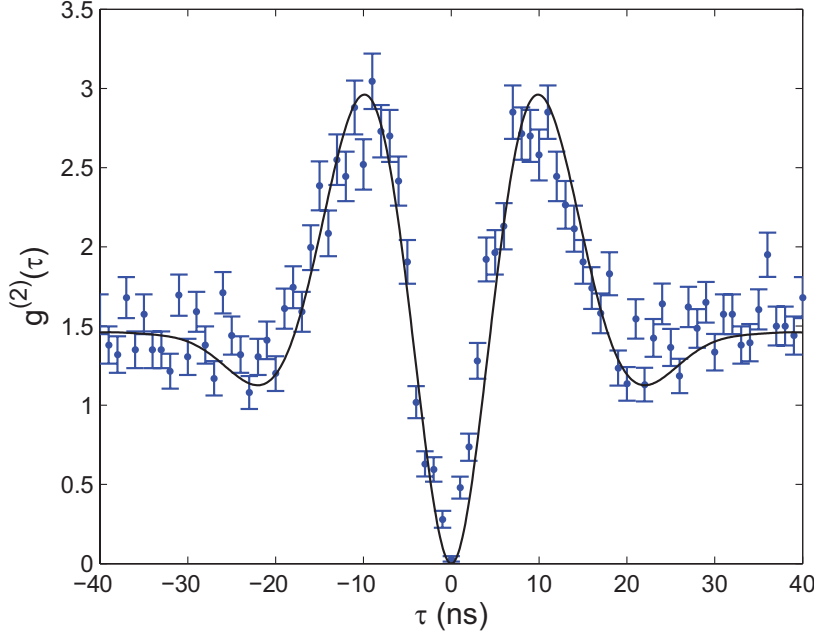


Figure 6.5: Normalized second-order correlation function of one ion when the beam path of the second ion is blocked. The solid line represents the theoretical prediction using eight-level Bloch equations.

time of ~ 30 minutes. The theoretical fit is drawn as a solid line neglecting the ion's motional degrees of freedom using the eight-level Bloch equations (see Chap. 2). The $g^{(2)}(\tau)$ -function is further used to calibrate the experimental parameters.

In Fig. 6.6 the total correlation function, $g_{\text{tot}}^{(2)}$ is presented such that photons impinging at the two input ports of the beam splitter are distinguishable by setting $\phi = 90^\circ$. Data points are obtained after 30 minutes of integration. The coincidence rate at $\tau = 0$ is measured $g_{\text{tot}}^{(2)}(0, 90^\circ) \approx 0.5$, as expected from Eq. (6.26). Indeed, for input with orthogonal polarization, the last term in Eq. (6.26) reduces to 0.5 without dependence on τ . The photons from the two ions are rendered distinguishable by their orthogonal polarization such that no interference occurs. Since in this case each photon still has a 50 % chance of being reflected or transmitted, among all possible correlations exactly half occur between photons exiting the beam splitter on the same output port. The result of the theoretical model from Eq. (6.26) is presented using the eight-level optical Bloch equations with the individual contributions indicated in the caption.

Figure 6.7 presents the second-order correlation function, $g_{\text{tot}}^{(2)}$, for the case that

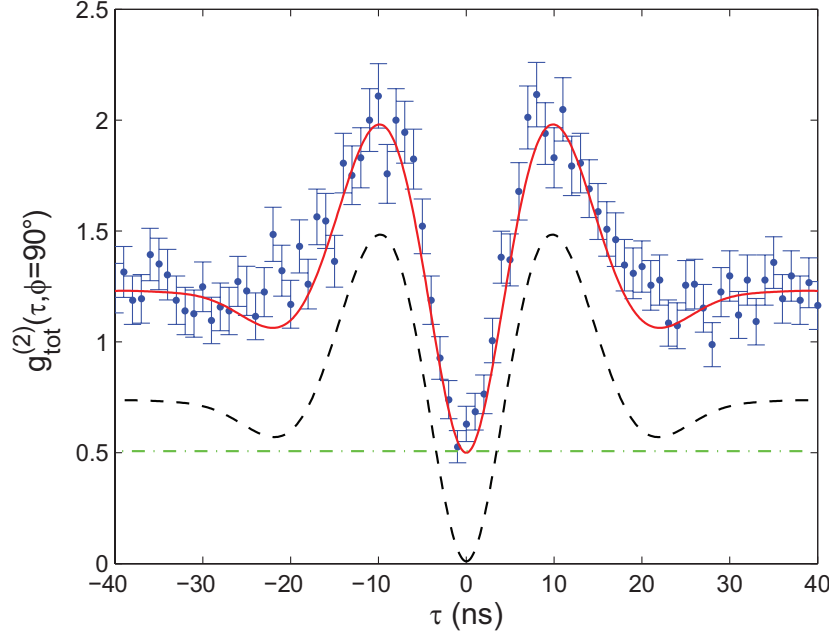


Figure 6.6: Normalized total second-order correlation function for orthogonal polarization between I_1 and I_2 ($\phi = 90^\circ$, i.e the non-interfering case). The results of the theoretical model (Eq. 6.26) based on Bloch equations is displayed by the solid line. The dashed and dash-dotted lines show the contributions of the first and second term of Eq. (6.26), respectively. Experimental data are all presented with a 1 ns resolution, without background subtraction, including the variance obtained from shot noise (Poisson statistics at all times τ).

the photons emitted by each ion are made fully indistinguishable, by setting $\phi = 0^\circ$. As expected, the normalized number of coincidences drops around $\tau=0$ which signals a two-photon interference. Comparing the measurement results of $g_{\text{tot}}^{(2)}(0, 90^\circ)$ and $g_{\text{tot}}^{(2)}(0, 0^\circ)$ we deduce a contrast of the two-photon interference of 89(2) %. The contrast is derived from raw experimental data, without subtraction of dark-counts from the PMTs and of laser stray light.

In Fig. 6.8 the number of coincidence counts at the point $\tau = 0$ as a function of the polarization angle ϕ is presented. This is obtained by gradual rotation of the half wave-plate in front of I_2 . Herewith the distinguishability of interfering photons decreases along with the amplitude of the two-photon interference. As indicated in Eq. (6.26) one expects a $\frac{1}{2}[1 - \cos^2 \phi] = \frac{1}{2} \sin^2 \phi$ dependence, which is displayed by the solid line in Fig. 6.8.

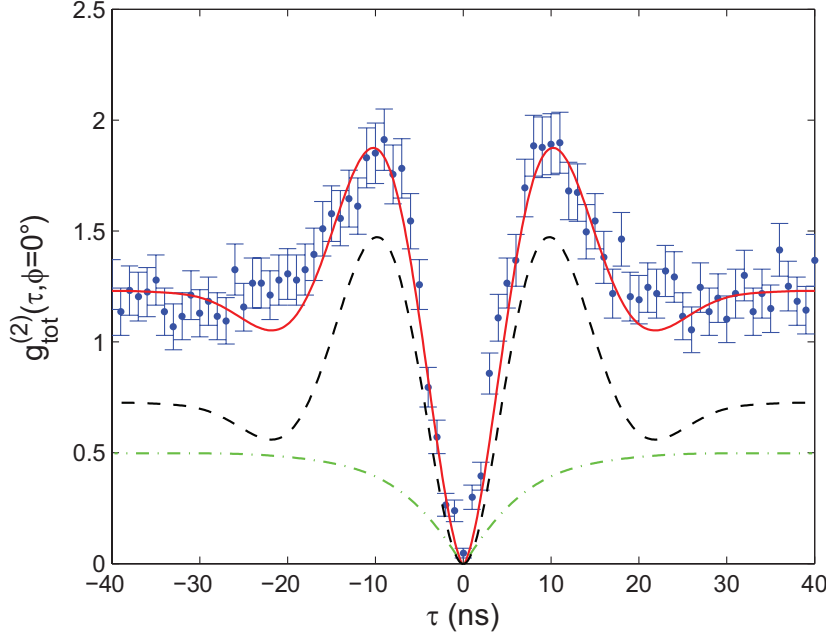


Figure 6.7: Normalized total second-order correlation function for the case of indistinguishable photons arriving at the beam splitter ($\phi = 0^\circ$). The contrast of the two-photon interference deduced from these measurements is 89(2) %. Similar to Fig. 6.6 the theoretical model given by Eq. (6.26) is displayed by the solid line. The dashed and dash-dotted lines represents the contributions of the first and second term of Eq. (6.26), respectively. Experimental data are presented with a 1 ns resolution, without background subtraction, including the variance obtained from shot noise (Poisson statistics at all times τ).

As mentioned above in the case of $\phi=0$ the first-order coherence properties of the interfering fields influences maximally the shape of the total measured correlation function. Here, in the vicinity of $\tau = 0$ the degree of indistinguishability of input photons is only characterized by the temporal overlap between the photon wave-packets. The length of these wave-packets corresponds to the coherence time of the photon which then governs the contrast of this two-photon interference [70]. For the point $\tau=0$ incident photons are detected simultaneously and thus are fully indistinguishable with a maximum amplitude of the two-photon interference. This behavior is represented by the last term of Eq. (6.26) and is shown in the experimental figures by the dash-dotted lines. The first order coherence $|g^{(1)}(\tau)|^2$ continuously decreases so that the first term of Eq. (6.26) continuously increases before saturating

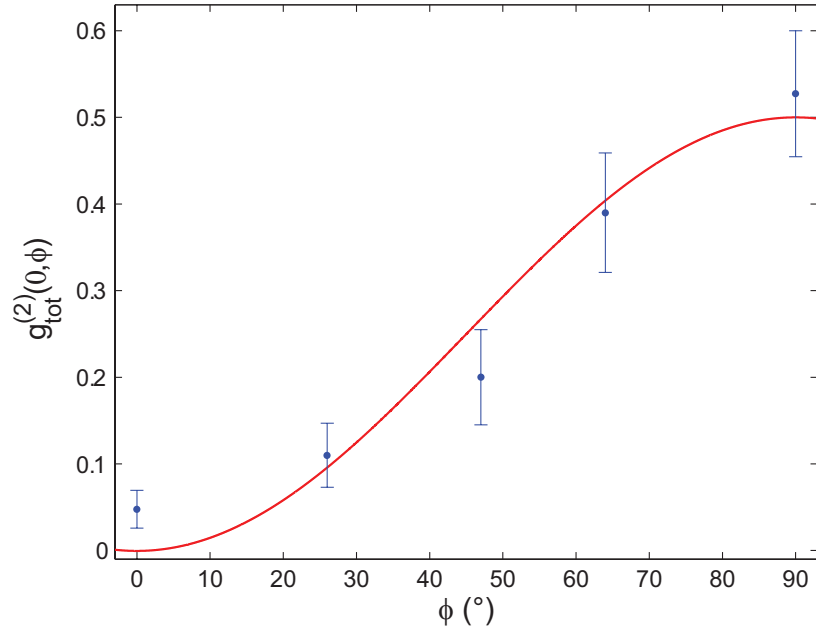


Figure 6.8: Coincidence rate at the point $g_{\text{tot}}^{(2)}(0, \phi)$ for varying polarization angles, $\phi \in \{0^\circ, 26^\circ, 47^\circ, 64^\circ, 90^\circ\}$. The solid line represents the $\frac{1}{2} \sin^2(\phi)$ dependence of the number of coincidences at $\tau = 0$ given by Eq. (6.26).

at 0.5 for $|\tau| \approx 30$ ns. This reveals a coherence time of the interfering photons of about 30 ns in our experiment. Furthermore, the fact that the $|g^{(1)}(\tau)|^2$ vanishes completely indicates for the resonance fluorescence a dominating part of incoherent scattering. Also compared to the non-interfering case of $\phi = \pi/2$ the optical nutation at $\tau = 10$ ns is reduced from ~ 2 to ~ 1.8 due to the normalization of the correlation function.

In summary, we have observed two-photon interference between resonance fluorescence photons emitted by remotely trapped ions. By superimposing their fluorescence on a 50:50 beam splitter the degree of the photons indistinguishability is determined to be 89(2)%. This is achieved by the use of high numerical aperture objectives inside the individual vacuum vessels and a fiber-to-fiber free space interferometer. The indistinguishability of the emitted photons constitutes an essential part for the implementation of entanglement protocols using atom-photon interfaces and thus demonstrates the setup's suitability for future processing of quantum information. Furthermore, the experiment is quantitatively reproduced by eight-level Bloch equations and shows that the coherence of resonance fluorescence photons can be quantified by means of two-photon interference under continuous laser excitation, in close analogy with the original work of Hong, Ou and Mandel [34].

Chapter 7

Intensity-field correlation

In this chapter the measurement of an intensity-field correlation function of the resonance fluorescence of a single trapped Ba^+ ion is discussed. The concept of this correlation and the basic measuring technique have been introduced in Sec. 3.3.

The method of cross-correlating light intensities first described by Hanbury-Brown and Twiss (HBT) [26] has revealed important insights in the field of statistical optics. Based on this idea we attempt to demonstrate the particle and wave aspect of light simultaneously by correlating a photon detection with fluctuations from the fluorescence field amplitude. In this approach a photon detection prepares the atom in its ground state and we observe the time evolution of the electromagnetic wave with well defined phase.

Measurements of the source-field employing correlation functions have been proposed by W. Vogel [91]. A wave-particle correlation function of the field was then first shown in a series of experiments by G. T. Foster et al. using optical pumped Rb atoms traversing through a high-finesse cavity. The field emitted out of a cavity corresponded on average to only a fraction of a photon excitation [32,33,92]. Further investigations of correlation functions sensitive to the electric field of many photons have been reported using laser and other light sources [27,38,47] and were recently approached theoretically [93]. In this experiment we show the first observation of the time evolution of the electromagnetic field corresponding to a single resonance fluorescence photon using a third-order correlation function.

Here, the correlation function is triggered by the detection of an initial fluorescence photon from a single trapped Ba^+ ion, which projects the ion into its ground state. Stop events are then obtained using a homodyne detection scheme, where the fluorescence field is overlapped with a local oscillator (LO) of well-controlled phase relative to the exciting laser. The experimental setup is interferometrically stabilized and the phase of the LO can be adjusted to anywhere within $[0, 2\pi]$. This correlation measurement is repeated many times for particular phases of the LO field, such that we gain an integrated signal that records the average conditional time evolution of the source field evolution back to equilibrium forming the emission of a single resonance fluorescence photon.

The following chapter starts with a description of the experimental setup followed by the theoretical model. The chapter ends with a discussion and summary of the experimental results. This work was published in [94].

7.1 Experimental setup

The schematic experimental setup is presented in Fig. 7.1. A single Ba^+ ion is loaded into the linear trap. The ion is continuously driven and laser-cooled by the 493 nm (green) and 650 nm (red) lasers.

The quantization axis is defined perpendicular to the laser polarization \vec{E} and the \vec{k} vector. The two observation channels are along the magnetic field direction, where we observe $\Delta m \pm 1$ photons on the left and right side of the trap.

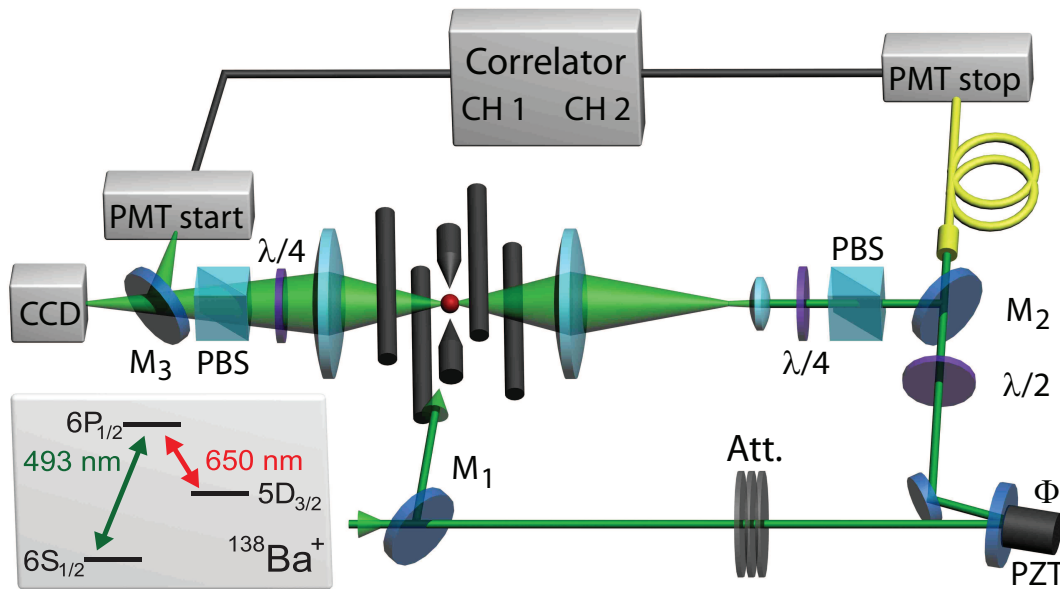


Figure 7.1: Sketch of the experimental setup: A single $^{138}\text{Ba}^+$ ion in a linear Paul trap is continuously laser excited. Two detection channels, left and right, allow for visual observation of the ion (CCD), or for recording correlations of the emitted light. The local oscillator (LO) is split off the excitation laser by M_1 in front of the trap, attenuated (Att.), and its polarization is adjusted with a $\lambda/2$ plate to match the polarization of the fluorescence beam. The inset shows the relevant electronic levels of $^{138}\text{Ba}^+$.

The objective collecting the fluorescence on the left side focuses the beam either on a PMT, which is used to provide the start signal for the correlator, or to the CCD

camera. On the righthand side the fluorescence is first collimated and outside of the chamber sent through a telescope¹, such that the beam has a collimated diameter of 2.7 mm. The fluorescence is then mixed with the LO field on a mirror M_2 with 99% reflectivity. After coupling to a single mode fiber², the interfering fields are detected at another PMT, which is used as the stop signal for the correlator. The count rate of the fluorescence after the fiber is about 10 kcps.

In both detection channels a quarter wave-plate and a Glan-Thompson polarizer select $\Delta m = +1$ photons, where the $\Delta m = -1$ transition is filtered out. In the stop channel a half-wave plate additionally rotates the polarization to match the linear polarization of the LO. The LO field used for mixing is split off the excitation laser in front of the trap by the mirror M_1 , successively attenuated and the polarization is controlled to cancel rotations due to mirror reflections.

The LO and the fluorescence beam hence form a Mach-Zehnder type interferometer, where the phase Φ can be set within 2π using a Piezo mounted mirror in the LO path. The phase information is directly visible in the count rate of the homodyne signal at the stop-PMT, which we continuously record during the experiment. The noise of the count rate is measured to be shot noise limited. Due to this shot noise and the observed visibility we know that the phase uncertainty is $< 10.3^\circ$ at the phase set to $\Phi = \pi/2$ and $< 24.1^\circ$ at $\Phi = \pi$ or $\Phi = 0$. To identify the different phase positions in the count rate we record the fringe of the interferometer prior to taking data by feeding a slowly triangular signal (1 mHz, 0.5 Vp-p) to the Piezo mirror. Phase locking is then performed by keeping the homodyne count rate constant. Here phase stability is found to be ensured within a time constant of several seconds and does not affect the contrast of the data within the limits set by the shot noise. Slowly varying phase drifts are continuously servoed using a PID controller³ applying feedback to the Piezo mounted mirror.

Correlations between the PMT start- and the PMT stop-counts are obtained by recording and processing of the obtained time information of single photon arrival times with the Time Acquisition Card (Correlator).

7.2 The model

Let us now consider the measured quantity of the apparatus. In a frame rotating at the (green) laser frequency, ω_L , the green source part of the field radiated by the ion reads

$$\hat{E}(t) = \xi e^{-i\omega_L t} \hat{\sigma}_{+1}^-(t) \vec{e}_{+1}, \quad (7.1)$$

¹Jenoptik, beam expander 2x-10x

²Schäffter&Kirchhoff, PMA-15 fiber coupler used with Thorlabs 493-PM fiber

³SRS, SIM960

where t is in the steady state limit after the exciting laser is turned on, ξ represents a constant amplitude and $\hat{\sigma}_{+1}^-$ is the Pauli lowering operator from $|P_{1/2}, m = -1/2\rangle$ to $|S_{1/2}, m = +1/2\rangle$, associated with a creation of a single $\Delta m = +1$ photon with polarization along \vec{e}_{+1} . For the remaining part of this chapter, however, we will omit the indices notation and simply write $\hat{\sigma}^-$.

If the LO path is blocked, we measure a conventional second-order correlation (see Sec. 3.2) as

$$g^{(2)}(\tau) \propto \langle \hat{E}^\dagger(0)\hat{E}^\dagger(\tau)\hat{E}(\tau)\hat{E}(0) \rangle \equiv \lim_{t \rightarrow \infty} \langle \hat{E}^\dagger(t)\hat{E}^\dagger(t+\tau)\hat{E}(t+\tau)\hat{E}(t) \rangle. \quad (7.2)$$

In terms of atomic lowering operators the correlation can be reexpressed as

$$g^{(2)}(\tau) = \frac{\langle \hat{\sigma}^+(0)\hat{\sigma}^+(\tau)\hat{\sigma}^-(\tau)\hat{\sigma}^-(0) \rangle}{\langle \hat{\sigma}^+(0)\hat{\sigma}^-(0) \rangle^2} \quad (7.3)$$

and is presented in Fig. 7.2. The curve exhibits the characteristic anti-bunching for small τ , with a coincidence rate of $g^{(2)}(\tau = 0) = 0.042(2)$ (without background subtraction). Aside from this small offset, the data is well reproduced by fitting laser powers and detunings with the 8-level Bloch equations. This $g^{(2)}(\tau)$ is then used to calibrate the laser settings for the later $g^{(1.5)}(\tau)$ measurement.

With the LO unblocked, we measure the homodyne signal at the PMT-stop conditioned on a photon detection at the PMT-start, with an adjustable phase Φ of the LO. We start by writing the measured fields at the detectors in units of the square root of photon flux. The mean photon flux impinging on the PMT-start is then given by $\gamma_1 \langle \hat{\sigma}^+ \hat{\sigma}^- \rangle$, where γ_1 is the radiative decay rate times the overall collection and detection efficiency of the PMT-start. Similarly, we can write the fluorescence field measured at the PMT-stop by $\sqrt{\gamma_2} \hat{\sigma}^-(0)$, where γ_2 is the radiative decay rate times the collection and detection efficiency of a photon at the PMT-stop. With the LO field expressed by a complex amplitude $\mathcal{E}e^{i\Phi}$ we denote the interfering fields at the PMT-stop as

$$X_\Phi(t) = [\mathcal{E}e^{i\Phi} + \sqrt{\gamma_2}\hat{\sigma}^-(t)]. \quad (7.4)$$

Note that this signal takes a similar form as Eq. (6.16), where we have derived the homodyne signal using a beam splitter. It follows that for positive τ we then measure a total unnormalized second-order correlation between PMT-start and PMT-stop as

$$G_\Phi^{\text{total}}(t, t + \tau) = \langle \sqrt{\gamma_1}\hat{\sigma}^+(t)X_\Phi^\dagger(t + \tau)X_\Phi(t + \tau)\sqrt{\gamma_1}\hat{\sigma}^-(t) \rangle, \quad (7.5)$$

which expands out to

$$G_\Phi^{\text{total}}(\tau) = F\{(1 - V)[(1 - r) + rg^{(2)}(\tau)] + Vg_\Phi^{(1.5)}(\tau)\}. \quad (7.6)$$

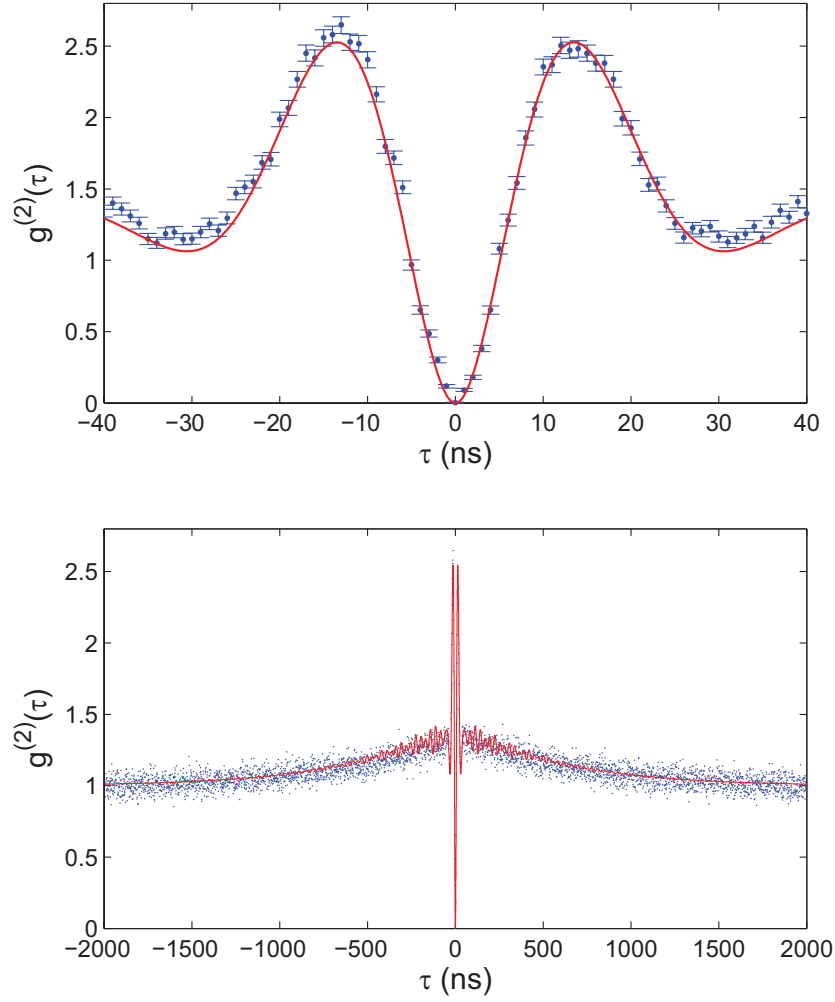


Figure 7.2: Measured second order correlation function with the LO path blocked for *top*: short delay times with Poisson statistics at all τ and for *bottom*: longer delay times. The solid line shows the theoretical prediction using experimental parameters and 8-level optical Bloch equations.

Here, we can identify the individual terms, where $g^{(2)}(\tau)$ is the intensity correlation function given by Eq. (7.3). Further, the prefactor F in Eq. (7.6) denotes the total photon flux into the correlator as

$$F = \gamma_1 \langle \hat{\sigma}^+ \hat{\sigma}^- \rangle (\mathcal{E}^2 + \mathcal{E} \sqrt{\gamma_2} \langle \hat{\sigma}^+ + \hat{\sigma}^- \rangle + \gamma_2 \langle \hat{\sigma}^+ \hat{\sigma}^- \rangle), \quad (7.7)$$

while the visibility of the interference part in $G_{\Phi}^{\text{total}}(\tau)$ is

$$V = \frac{\mathcal{E}\sqrt{\gamma_2}\langle\hat{\sigma}^+ + \hat{\sigma}^-\rangle}{\mathcal{E}^2 + \mathcal{E}\sqrt{\gamma_2}\langle\hat{\sigma}^+ + \hat{\sigma}^-\rangle + \gamma_2\langle\hat{\sigma}^+\hat{\sigma}^-\rangle} \quad (7.8)$$

and the ratio of the fluorescence intensity to the total intensity at the PMT-stop is given by

$$r = \frac{\gamma_2\langle\hat{\sigma}^+\hat{\sigma}^-\rangle}{\mathcal{E}^2 + \gamma_2\langle\hat{\sigma}^+\hat{\sigma}^-\rangle}. \quad (7.9)$$

The third-order correlation function at a given LO phase is then given by

$$g_{\Phi}^{(1.5)}(\tau) = \frac{\langle\hat{\sigma}^+(0)[e^{i\Phi}\hat{\sigma}^+(\tau) + e^{-i\Phi}\hat{\sigma}^-(\tau)]\hat{\sigma}^-(0)\rangle}{\langle\hat{\sigma}^+ + \hat{\sigma}^-\rangle\langle\hat{\sigma}^+\hat{\sigma}^-\rangle}. \quad (7.10)$$

When we examine at this point the phase Φ between the LO and the fluorescence at the mixing mirror more closely, we find that it consists of two parts. Considering the phase shift the ion induces when scattering light from the laser field we can write the phase as the sum of two parts $\Phi = \Phi' + \Psi$. Here Ψ denotes the phase of the oscillating atomic dipole (the source field) of the $|P_{1/2}, m = -1/2\rangle$ to $|S_{1/2}, m = +1/2\rangle$ transition with respect to the exciting laser and with that to the LO. The phase Φ' represents the interferometer phase of the LO with respect to the fluorescence at the mixing mirror. Hence, while the phase Φ' is freely tuneable by the Piezo mirror as seen above the phase Ψ is predetermined by the laser parameters. The $g_{\Phi}^{(1.5)}(\tau)$ from Eq. (7.10) is then reexpressed in a form depending on Φ' as

$$g_{\Phi}^{(1.5)}(\tau) = e^{-i(\Phi'+\Psi)}g^{(1.5)'}(\tau) + e^{i(\Phi'+\Psi)}(g^{(1.5)'}(\tau))^*, \quad (7.11)$$

where $g^{(1.5)'}(\tau)$ and its complex conjugate $(g^{(1.5)'}(\tau))^*$ are the correlation functions of the three Pauli lowering operators given by

$$g^{(1.5)'}(\tau) = \frac{\langle\hat{\sigma}^+(0)\hat{\sigma}^-(\tau)\hat{\sigma}^-(0)\rangle}{\langle\hat{\sigma}^+ + \hat{\sigma}^-\rangle\langle\hat{\sigma}^+\hat{\sigma}^-\rangle}. \quad (7.12)$$

The $g_{\Phi}^{(1.5)}(\tau)$ defined by Eq. (7.11) is hence a real function for all Φ' with the interesting cases as

$$\begin{aligned} g_0^{(1.5)}(\tau) &= \text{Real}(g^{(1.5)'}(\tau) e^{-i\Psi}) \\ g_{\pi}^{(1.5)}(\tau) &= -\text{Real}(g^{(1.5)'}(\tau) e^{-i\Psi}) \\ g_{\pi/2}^{(1.5)}(\tau) &= \text{Imag}(g^{(1.5)'}(\tau) e^{-i\Psi}). \end{aligned} \quad (7.13)$$

For illustration purposes the dependence of Ψ as a function of the green laser detuning is plotted in Fig. 7.3 using Bloch equations. The remaining parameters

entering the plot are the same as used in Fig. 7.2. Ψ is then found by calculating the phase argument of the $g^{(1.5)'}(\tau)$ from Eq. (7.12) as

$$\Psi = \arctan \frac{\text{Imag}(g^{(1.5)'}(\tau))}{\text{Real}(g^{(1.5)'}(\tau))}. \quad (7.14)$$

The two visible resonances are associated with the two Raman transitions involving the $|S_{1/2}, m = +1/2\rangle$ state between the $|2\rangle \Leftrightarrow |6\rangle$ and $|2\rangle \Leftrightarrow |8\rangle$ electronic levels as indicated by Fig. 2.5, where the position of the resonances mainly depends on the laser intensities and the red laser detuning. As all parameters are fixed for the duration of the experiment the theoretical phase lag of the driven oscillating atomic dipole is found to be $\Psi = 18.25^\circ$ as indicated by the red cross in Fig. 7.3.

For our experimental analysis we define Φ' in such a way, that the LO phase at the mixing mirror relative to the asymptotic phase of the fluorescence field is $g_{\pi/2}^{(1.5)}(\tau \rightarrow \infty) = 0$, i.e. by this convention we denote the fluorescence being in phase with the LO at the position of the mixing mirror for $\Phi = 0$. Calibration of the LO phase is then obtained by looking for the maximum and minimum count rate at the PMT-stop, where we measure the asymptotic values of $G_{\Phi}^{\text{total}}(\tau)$, and assigning to them the LO phases $\Phi = 0$ and π , respectively.

Recalling now the total measured correlation function from Eq. (7.6) we can identify three individual parts which constitute the recorded correlation function. The last term in Eq. (7.6) expresses the interfering part of the fluorescence with the LO weighted by the visibility V and reveals the $g^{(1.5)}(\tau)$ correlation in dependence of Φ . The remaining non-interfering part proportional to $1 - V$ consists of a second-order correlation function $g^{(2)}(\tau)$, where both the start and stop counts are only from fluorescence photons, weighted by r . Further, within the non-interfering part a constant offset in the correlation function, weighted by $1 - r$, arises for the cases where the stop counts are solely triggered from LO photons. We then normalize $G_{\Phi}^{\text{total}}(\tau)$ by $F(1 - V)$ as

$$g_{\Phi}^{\text{total}}(\tau) = (1 - r) + rg^{(2)}(\tau) + \frac{V}{1 - V}g_{\Phi}^{(1.5)}(\tau), \quad (7.15)$$

where this normalization is chosen such that at a LO phase of $\Phi = \pi/2$ the $g_{\Phi}^{(1.5)}(\tau)$ vanishes asymptotically for large τ and the measured correlation function $g_{\Phi}^{\text{total}}(\tau)$ yields an asymptotic value of 1.

7.3 Experimental results

Figure 7.4 shows the measured correlations between PMT-start and PMT-stop with the LO phase adjusted to $\Phi = 0, \pi/2$ and π . The data acquisition time is 30 minutes

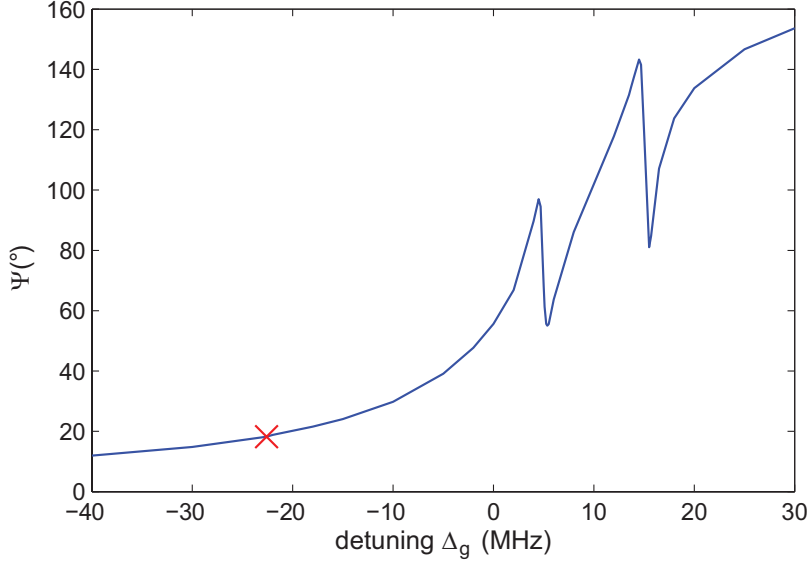


Figure 7.3: Calculated phase Ψ of the atomic dipole of the $|P_{1/2}, m = -1/2\rangle$ to $|S_{1/2}, m = +1/2\rangle$ transition with respect to the excitation laser as a function of the green laser detuning. Parameters are the same as used in Fig. 7.2. The red cross indicates the detuning for this experiment.

for each curve and is presented with a 1 ns resolution. The corresponding variance is obtained from shot noise, i.e. assuming Poisson statistics at all times τ . The individual solid curves represent the theoretical predictions applying optical Bloch equations. The data is then reproduced with a superposition of the three contributions as described by Eq. (7.15) with an intensity ratio $r = 0.31$ and a visibility $V = 17.5\%$. Given by these parameters all curves contain a constant offset and scaled $g^{(2)}(\tau)$ and $g^{(1.5)}(\tau)$ correlation functions. As indicated by Eq. (7.14) and by measuring at particular phases Φ , we can observe different contributions of the complex third-order correlation function. Thus, curve b), where the LO phase is adjusted to $\Phi = \pi/2$, reveals the imaginary part of the atomic polarization whose asymptotic value is zero. On the other hand, curve a) and c) imply the real part of the polarization. In curve a) the LO phase is adjusted to 0 and the real part of the polarization is added constructively to the offset and $g^{(2)}(\tau)$. In curve c) the LO phase is adjusted to π and the real part is added destructively to the other two contributions. In all three curves we observe the same coincidence rate at $\tau = 0$. Since both the $g^{(2)}(\tau)$ contribution and the $g_{\Phi}^{(1.5)}(\tau)$ contribution exhibit anti-bunching and are identically zero at $\tau = 0$, the coincidence rate for the total correlation function is merely defined by the constant contribution of non-interfering LO photons

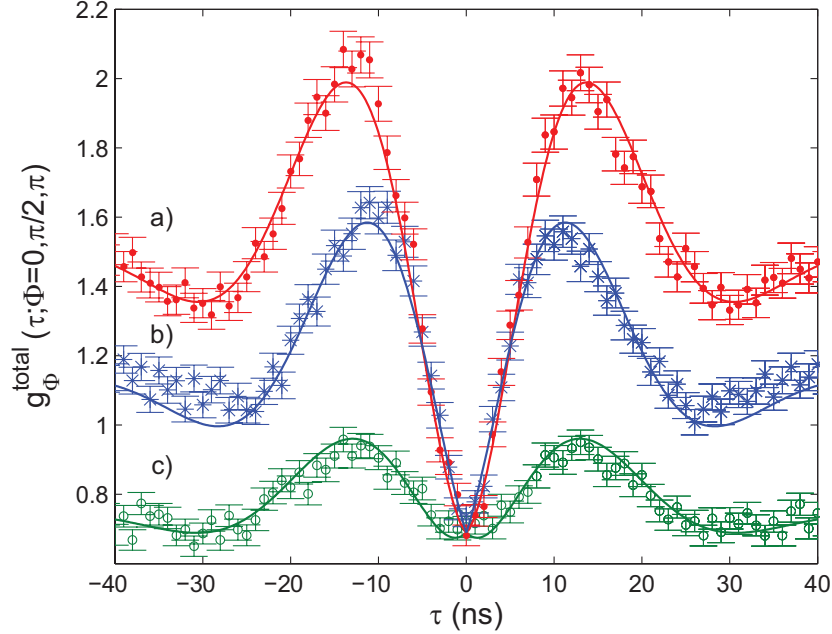


Figure 7.4: Normalized measured correlation function $g_{\Phi}^{\text{total}}(\tau)$ obtained for a) the fluorescence being in-phase with the LO, $\Phi = 0$, c) the fluorescence being out-of-phase with the LO, $\Phi = \pi$, and b) at $\Phi = \pi/2$. The results of the theoretical model from Eq. (7.15) based on Bloch equations are displayed by the solid lines.

(plus background counts) in the homodyne signal of the PMT-stop.

Obtaining the bare complex $g^{(1.5)}(\tau)$ correlation function hence requires to measure the total correlation function for two orthogonal phases. From Eq. (7.15) we deduce the relations

$$g_0^{(1.5)}(\tau) = \frac{1-V}{2V} [g_0^{\text{total}}(\tau) - g_{\pi}^{\text{total}}(\tau)] \quad (7.16)$$

and

$$g_{\pi/2}^{(1.5)}(\tau) = \frac{1-V}{2V} \left\{ 2g_{\pi/2}^{\text{total}}(\tau) - [g_0^{\text{total}}(\tau) + g_{\pi}^{\text{total}}(\tau)] \right\}. \quad (7.17)$$

Thus, by according post-selective subtraction of the measured data points presented in Fig. 7.4 we deduce the intensity-field correlation function at the phases 0 and $\pi/2$. The results are pictured in Fig. 7.5 along with the theoretical model of Eq. (7.15). The variances are obtained from error propagations from the data in Fig. 7.4. The

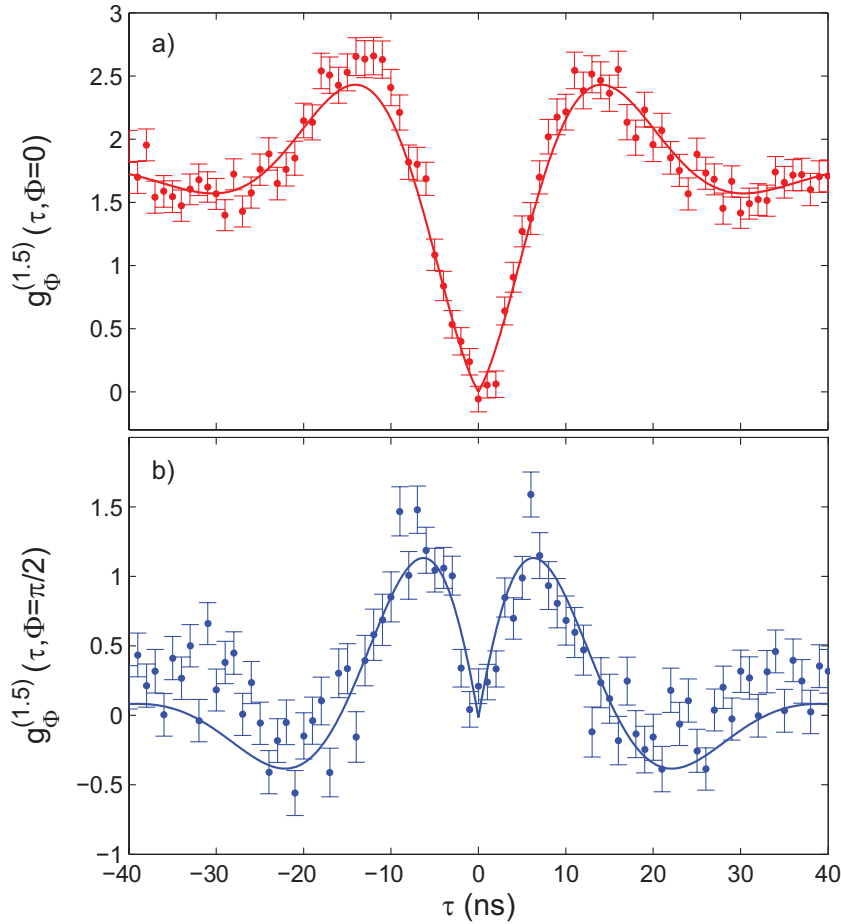


Figure 7.5: Intensity-field correlation function $g_{\Phi}^{(1.5)}(\tau)$ with the LO phase set to a) $\Phi = 0$ and b) $\Phi = \pi/2$, deduced from the data in Fig. 7.4 using Eq. (7.16) and Eq. (7.17), respectively. The solid lines represent the theoretical model using Eq. (7.14).

data reveal the time evolution of the resonance fluorescence field as it evolves after its initialization by an emitted photon into equilibrium via damped Rabi oscillations. These oscillations are both visible in the real and imaginary part of the $g^{(1.5)}(\tau)$. In the latter this indicates the energy transfer between the laser field and the atomic dipole before reaching steady-state with an asymptotic value of zero. Comparing Fig. 7.2 with Fig. 7.5 a) we identify a linear growth with τ around the point $\tau = 0$ for the $g^{(1.5)}(\tau)$ correlation while the $g^{(2)}(\tau)$ grows quadratically with τ . This structure clearly indicates that in the intensity-field correlation the field rather than

the intensity is measured.

Further we see, that in this experiment of an intensity-field correlation function the wave-particle duality aspect of light is inherently invoked since a detection of a photon at the PMT-start conditions the PMT-stop events by measuring the homodyne signal of two interfering fields, i.e. we have a clear particle-picture directly linked to a wave-like picture. Thus, the intensity detection that triggers the correlation measurement may be explained by merely a particle property of light where the wave properties of the fluorescence light are visible in the interfering homodyne signal at the stop PMT.

Limitations

The limitation for the visibility in the homodyne signal is mainly determined by the temporal overlap of two-photon wave packets impinging at the mixing mirror. This overlap is then limited by the coherence time and the flux of the fluorescence photons with respect to the LO photons, where the coherence time of the laser is known to be $T = 1/\Delta\nu \approx 50 \mu s$ [95]. The fluorescence count rate of 10 kcps is hereby predetermined by the collected fraction given by solid angle and the fiber-coupling efficiency. While the temporal overlap would benefit from a higher LO intensity (smaller r), this would make the phase uncertainty bigger and the phase drift compensation more difficult. Thus, optimizing the experiment resulted in a reduced visibility of $V = 17.5\%$ and an intensity ratio of $r = 0.31$.

To additionally estimate the effect of the ion motion on the visibility we assume the ion to be near the Lamb-Dicke regime under Doppler-cooling condition (see Sec. 5.3.3). In this respect, the cooling laser intensity is adjusted below saturation to combine efficient laser cooling of the motion with a large emission rate of fluorescence photons. For these parameters the ion is at a mean motional state of $\langle n \rangle \sim 15$ after Doppler cooling. The Lamb-Dicke parameter is then given by $\eta = (\hbar \vec{k}^2 / 2m\omega)^{1/2} = 0.077$ and the effective Lamb-Dicke parameter, defined by $\eta^2(2n + 1) = 0.184$ is still much smaller than 1. As discussed in Sec. 2.2.2 the coupling strength on the carrier is here well approximated by $\Omega_{n,n} = \Omega(1 - \eta^2 n)$, where η denotes the overall coupling strength. Hence, we expect that $\sim 92\%$ of the fluorescence intensity appears on the carrier transition and the ionic motion at the Doppler limit has no significant influence on the reduction of the visibility.

Summary

In summary, the measurement of an intensity-field correlation function of the resonance fluorescence from a single $^{138}\text{Ba}^+$ ion was shown with the aid of a homodyne detector. In this experiment a photon detection from the ion prepared the correlation measurement in a well defined state from where the evolution back into

equilibrium via Rabi oscillations is observed. The $g^{(1.5)}$ correlation function was deduced from acquired data collected at three different phases of the LO.

The intensity-field correlation and thus monitoring the resonance fluorescence field could be further used to develop a tool to investigate and monitor the emission of a single-photon field under the influence of boundary conditions, such as mirrors, cavities or other atoms, with even the possibility of applying feedback onto the radiating dipole [31, 69, 96, 97].

This measurement technique further allows a detailed investigation of the non-classical statistical behavior of the atomic dipole. The third-order correlation function is in principle suited to observe the effect of squeezed resonance fluorescence light [91, 92, 98]. However for such properties to become visible the single ion must be driven in the weak excitation regime, which was not the case in the present experiment. A higher collection efficiency of the fluorescence or even a cavity enclosing the ion would be required to reach this regime and might be subject for further investigations.

Chapter 8

Interference of fluorescence in a half cavity

This chapter discusses experiments performed with Ba^+ ions situated in a half cavity system. Such a setup was first realized by Ch. Raab [52], where the resonance fluorescence of a trapped ion was reflected back onto itself using a $\text{NA}=0.4$ objective inside the vacuum apparatus and a distant mirror situated about 30 cm away from the ion. In this regime, where the mirror distance is much farther away than the observed wavelength, only far field effects can be investigated. Nevertheless, due to the high numerical aperture of the objective the focus spot is relatively small ($\sim 1 \mu\text{m}$) and the mode density at the position of the ion is significantly altered enabling an efficient way to investigate QED effects.

The self-homodyne interference along the mirror channel was first studied by J. Eschner et al. [31]. A maximal interference visibility of 72% along with a small change of $\sim 1\%$ in the atomic decay rate was observed. The system was further addressed in detail in various studies including investigations of the vacuum-induced level shift of the ion, first theoretically by U. Dorner et al. [97] and then experimentally by M. A. Wilson et al. [99]. Here the associated radiation force in the standing wave was detected, which manifests itself in a small shift of the trap frequency. In addition, F. Dubin et al. [100] observed the time resolved evolution of a single photon interference at different positions of the standing wave pattern by employing intensity correlation functions.

In another experimental approach the motional state of the ion can be retrieved by Fourier analysis of the self-homodyne photocurrent. First investigated by P. Bushev et al. [69] they showed that the motional state could be influenced by phase-locking an external local oscillator to the ion motion and feeding back a phase-shifted signal to one of the trap electrodes. With this technique of electro-mechanical feedback action it was then possible to cool the motional quanta of the ion to 30% below the Doppler limit as presented in [54].

This chapter follows the line of experiments performed with this half-cavity system

starting with an introductory theoretical and experimental description of the system. In the following, the self-homodyne signal is analyzed in Fourier space which gives access to the motional sidebands. This part is followed by an experiment, where the shape of the first order coherence is determined from the interference signal up to large mirror-ion distances. At last, a system of two ions situated in the same trap and interacting over the mirror channel is discussed and characterized by visibility measurements and the use of second-order correlation functions.

8.1 Half cavity setup

The experimental setup to achieve high resolution single photon interference is based on a half cavity design implemented first in the ring trap apparatus (see Sec. 5.1.2) and is depicted in Fig. 8.1. The ion is addressed with all lasers from the left side using a $f=250$ mm lens (not shown) to create a focus at the trap center. The fluorescence emitted from the ion is collected and collimated along the direction l with the objective L_1 (NA=0.4) and sent to a Piezo mounted mirror¹. In this notation the ion is located at the position $l = 0$ and the mirror position is at $l = D$. The light emitted into the detection channel is then superimposed with the backreflected light from the mirror and is collected by the objective L_2 . The round-trip time a photon needs to cover the distance ion-mirror-ion is denoted with $\tau = 2D/c$. The interfering fields can now be alternatively guided to a CCD camera, to a HBT-setup or coupled into a single mode optical fiber and detected at a PMT.

The mirror itself can be shifted over several μm by feeding a slowly varying triangular signal (1 mHz, 0.5 Vp-p) to its supporting Piezo stage. The stability of the experimental setup is hereby found to be phase-stable for several tens of seconds. However, slow phase drifts can be continuously monitored by the amplitude of the interference signal and fed back to the Piezo mounted mirror using a PID controller² to within 5-10 nm accuracy.

With a photon emission rate of 15 MHz on the green transitions and a mirror distance of a few ten centimeters we can assume that only one photon is present at a time between the mirror and the ion. Thus, the observed interference effect arises from a single fluorescence photon interfering with itself. Figure 8.2 hereby sketches the temporal evolution of the light field emitted along the mirror and detection channel axis. The indistinguishability of the directly emitted and back reflected light on the detector side then yields an interference of the two fields at the position of the ion. After the time $\tau = 2D/c$ a standing wave pattern has formed with the ion in this case illustrated at a node position. The time evolution of this single

¹Physical Instruments, P-762-TL

²SRS, SIM960

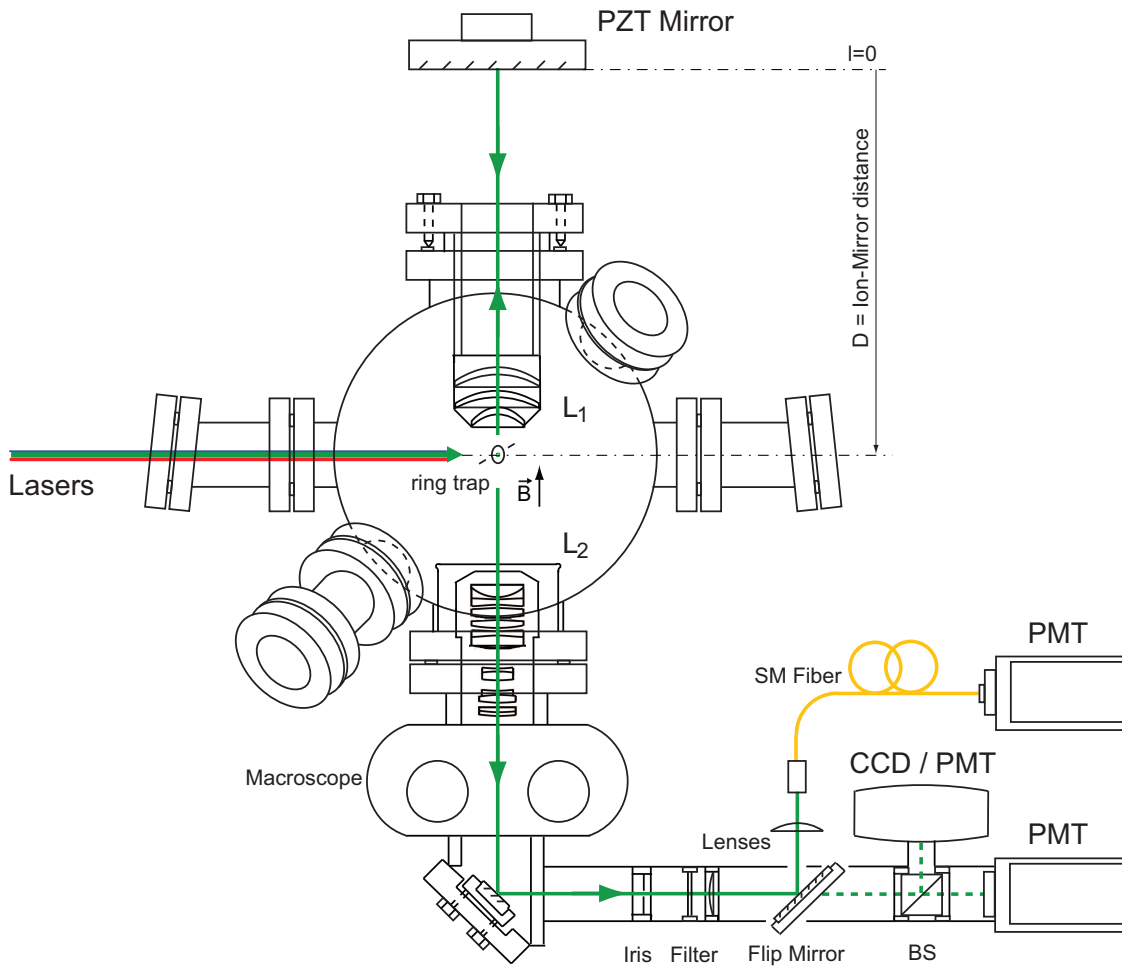


Figure 8.1: Experimental setup of the ring trap apparatus with the Piezo mounted mirror. The ion-mirror distance is denoted by D .

photon interference and the build-up process of the standing wave pattern was first measured in [100] by recording correlation functions at three different positions within one interference fringe.

Intuitively, the backreflected light from the mirror focused onto the ion further creates a modification of the resonant electromagnetic vacuum modes at the ion's position. Since the resonant mode density at the position of the ion directly influences the spontaneous emission rates a change in the excited state populations in steady state follows. With the experimental limitation of the objective's collected solid angle this effect is expected to be a few percent and was observed in [31] while looking at the green and red count rate in the mirror channel simultaneously.

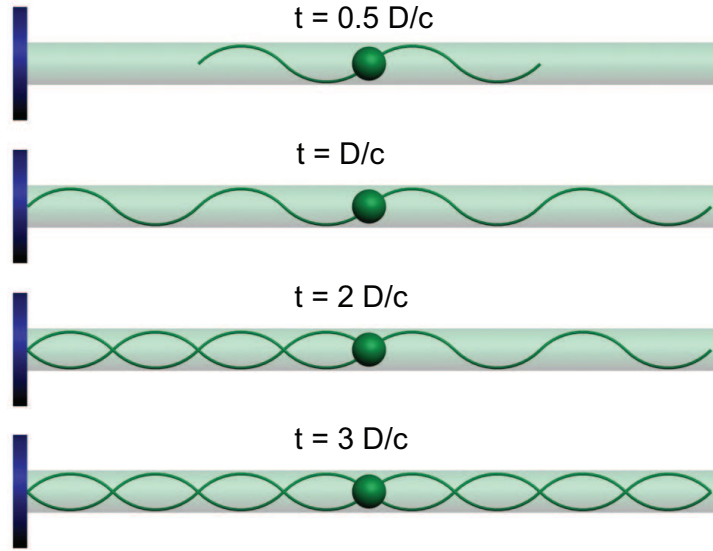


Figure 8.2: Sketch of the time evolution of the resonance fluorescence light field emitted by an ion during a round-trip into a standing wave pattern, where D is the distance ion-mirror.

To qualitatively describe the half cavity system we start by writing the light field emitted by the ion along the mirror and detection channel in terms of the electric field operator as:

$$\hat{E}^+(t, \tau) = \sqrt{\epsilon \Gamma_L} \exp[-i\omega_L t + i\vec{k}_L \hat{r}_i(t)] \left(\hat{\sigma}^-(t) + \exp[i\omega_L \tau + i\vec{k}_L \hat{r}_i(\tau)] \hat{\sigma}^-(t + \tau) \right). \quad (8.1)$$

Here τ denotes the delay time as $\tau = 2D/c$ and ϵ represents the collected fraction of solid angle. The Pauli lowering operator $\hat{\sigma}^-$ from the $|P_{1/2}\rangle$ to the $|S_{1/2}\rangle$ state is given by Eq. (3.25). Γ_L is the spontaneous emission rate and ω_L and \vec{k}_L are the associated transition frequency and wave vector along the mirror direction.

Note that in Eq. (8.1) the secular motion of the ion has been included by the ionic position operator as elaborated in Sec. 5.3.4 as $\hat{r}_i(t) = r_0(\hat{a}_i e^{-i\omega_i t} + \hat{a}_i^\dagger e^{i\omega_i t})$. \hat{a}_i and \hat{a}_i^\dagger are then the bosonic creation and annihilation operator of one motional quantum. Since the frequency of the secular motion $\omega_i \ll 1/\tau = c/2D$ we can assume $\hat{r}_i(t + \tau) \approx \hat{r}_i(t)$.

The measured intensity I of the interfering fields as recorded in the photocurrent

of the homodyne signal is then given by

$$I = \langle \widehat{E}^+(t, \tau) \widehat{E}^-(t, \tau) \rangle, \quad (8.2)$$

which can be expanded using Eq. (8.1) as

$$\begin{aligned} I &= \epsilon \Gamma_L (\langle \hat{\sigma}^+(t) \hat{\sigma}^-(t) \rangle + \langle \hat{\sigma}^+(t + \tau) \hat{\sigma}^-(t + \tau) \rangle + \langle \hat{\sigma}^+(t + \tau) \hat{\sigma}^-(t) e^{-i[\omega_L \tau + 2\vec{k}_L \hat{r}_i(t)]} \\ &+ \hat{\sigma}^+(t + \tau) \hat{\sigma}^-(t) e^{i[\omega_L \tau + 2\vec{k}_L \hat{r}_i(t)]} \rangle). \end{aligned} \quad (8.3)$$

Here, the first two terms of the one-time expectation values can be associated by the count rate $2\langle n \rangle$, whereas the two-time expectation values can be identified as the sum of the first order correlation functions $\langle G^{(1)*}(t, t + \tau) \exp[-i\omega_L \tau - i2\vec{k}_L \hat{r}_i(t)] + G^{(1)}(t, t + \tau) \exp[i\omega_L \tau + i2\vec{k}_L \hat{r}_i(t)] \rangle$. Here, $e^{i\omega_L \tau}$ indicates the modulation according to the phase delay caused by the mirror channel. Additionally, the motion of the ion leads to a further modulation of the interference signal represented by $e^{i2\vec{k}_L \hat{r}_i(t)}$.

To obtain the expectation value of the homodyne intensity the motional term can be evaluated by describing the ion at the Doppler cooling limit within the Lamb-Dicke regime with $\eta = (\hbar k_L^2 / 2m\omega)^{1/2} = 0.077 \ll 1$. The intensity in the motional sidebands is then reduced by the Lamb-Dicke parameter η compared to the intensity in the carrier and we can further neglect higher order sideband transitions. Hence, in this regime the motion of the ion can be described by a harmonic oscillator $r_i(t) = r_0 \sin(\omega_i t)$ with small amplitude r_0 . This amplitude is then derived by considering the ion's motion under the statistic process of laser cooling, where the motional occupation has to be characterized with a thermal state and integrated over all possible harmonic oscillation amplitudes. The expectation value of the position operator \hat{r}_i of a thermal state is given by $\langle \hat{r}_i \rangle = \text{Tr}[\hat{r}_i \hat{\rho}_{\text{th}}]$, where $\hat{\rho}_{\text{th}} = \sum_n e^{-E_n/kT} |n\rangle \langle n|$ is the density matrix of a statistical mixture with states $|n\rangle$. This yields that the ion is not oscillating with a fixed amplitude r_0 , but rather with a sum over all harmonic oscillation amplitudes weighted by a Gaussian distribution.

Looking at the last term of Eq. (8.3) the now weighted harmonic oscillator in the exponent can be rewritten as a weighted zeroth-order Bessel function $J_0(\eta_{\text{th}}^2) \exp(-\eta_{\text{th}}^2)$ of a thermal state. The thermal spread of the excitation of the ion η_{th}^2 is then given by $\eta_{\text{th}} = \sqrt{\langle k_L^2 r_0^2 \rangle}$.

Combining all terms the measured homodyne intensity hence simplifies to

$$I = 2I_0 [1 + \text{Real}(g^{(1)}(\tau) e^{i\omega_L \tau}) J_0(\eta_{\text{th}}^2) e^{-\eta_{\text{th}}^2}]. \quad (8.4)$$

Rewriting the first part of the intensity as $2I_0 [1 + |g^{(1)}(\tau)| \cos(\omega_L \tau + \phi)]$ we can then deduce a simple expression for the homodyne visibility as

$$V = \frac{I_{\text{max}} - I_{\text{min}}}{I_{\text{max}} + I_{\text{min}}} = |g^{(1)}(\tau)| J_0(\eta_{\text{th}}^2) e^{-\eta_{\text{th}}^2}. \quad (8.5)$$

Thus, the visibility is directly proportional to the absolute value of the first-order coherence. In the experiment the visibility is then obtained by slowly varying the mirror distance $D = 2c\tau$ over several wavelengths while recording the count rate.

As seen from Eq. (8.5) the ion's motion enters the visibility as a decreasing factor depending on the population of the motional states. For the ground state extension this yields a maximally reachable visibility of 93% and will further reduce for experimental conditions with continuous laser excitation. The dependence of the visibility on the thermal spread and on the green laser intensity is elaborated in detail in [52]. At the Doppler limit the maximally reached visibility was then measured to be 72% [31]. For the course of the following $g^{(1)}(\tau)$ -measurement we can consider the motional dependence as a constant factor and are hence only concerned with the reduced visibility

$$V' = |g^{(1)}(\tau)|. \quad (8.6)$$

Note that to access any information about the phase of the fluorescence field a phase reference has to be implemented, as it was performed in the intensity-field correlation measurement in chapter 7.

8.2 Visualization of sidebands

The self-homodyne signal can be further used to visualize the motional sidebands in the frequency domain. Starting from Eq. (8.3) we can rewrite the expectation value of the motional term in an exponential series as $e^{i\vec{k}_L \hat{r}_i} \simeq 1 + i\eta(\hat{a}_i + \hat{a}_i^\dagger)$. This directly reflects an intensity in the motional sidebands with strength η compared to the intensity in the carrier. The homodyne intensity can hence, and alternatively to Eq. (8.4), be expressed as

$$I = 2I_0 [1 + \text{Real}(g^{(1)}(\tau)e^{i\omega_L\tau})(1 + 2\eta(\hat{a}_i + \hat{a}_i^\dagger) + O(\eta^2))], \quad (8.7)$$

which now contains the explicit information of the ion's motion over the position operator $\hat{x}_i \sim \hat{a}_i + \hat{a}_i^\dagger$. Its real-time observation becomes accessible when analyzing the Fourier transform of the photocurrent. In the experiment this is realized by sending the monitored count rate to the spectrum analyzer³, which is operated with a set of fitted parameters that can be found in [58]. The sidebands become well visible at a typical count rate of ~ 50 kcps and a fringe visibility of about 30%. For a fixed location of the ion at the maximum gradient of the interference fringe i.e. $\omega_L\tau = \pi(n + 1/4)$, the average intensity of the homodyne signal from Eq. (8.7)

³Rohde&Schwarz, Spectrum Analyzer

deduces then, shown by V. Steixner et al. [101], to:

$$\begin{aligned}
 I &= \frac{\gamma}{2}[1 + 2\eta(\hat{a}_i + \hat{a}_i^\dagger)] \\
 \gamma &= \epsilon\Gamma_L \frac{\Omega_L^2}{4\Delta_L^2 + \Gamma_L^2}
 \end{aligned}
 \tag{8.8}$$

with the parameter γ being the optical pumping rate into the mirror channel, Ω_L defining the Rabi frequency and Δ_L the laser detuning.

Figure 8.3 depicts the measurement of the radial x- and y-sideband for an applied rf power of 5 W and a drive frequency of 19.3 MHz using the ring trap apparatus. The top graph depicts both sidebands with an amplitude of ~ 3 dBm above the Poissonian noise. The z-sideband is not shown and is expected to be located at ~ 2.2 MHz. In the bottom graph the x-sideband is recorded with a higher resolution. Here, the sideband appears as a resonance with a Lorentzian profile 4 dBm above the Poissonian noise level. The solid line represents a Lorentzian fit with a FWHM of $\Gamma = 713 \pm 33$ Hz. The central peak hereby corresponds to the ion's mean secular oscillation frequency in the pseudo-potential. The height is then related to the amplitude of the ion's oscillation, whereas the width of the sideband corresponds to the cooling rate and thus to the mean phonon number of the motional excitation [67, 102]. The small asymmetry of the sidebands towards lower frequencies arises due to the laser cooling process of the ion [103].

An alternative access to the sideband information can be found in a $g^{(2)}(\tau)$ measurement. While this method requires more time for data acquisition than the direct Fourier analysis of the photocurrent, it yields a higher sensitivity of the ion's motion and thus requires a smaller signal-to-noise ratio. In [60] the x- and y-sideband have been observed taking the FFT of a $g^{(2)}(\tau)$ integrated over 30 min. As described in Sec.5.3.2 this method also finds use to determine the suitable voltage parameters for the micromotion compensation of a trapped ion.

In the work of Ch. Raab et al. [102] the spectrum of resonance fluorescence was further investigated with high resolution using a heterodyne detection method of the resonance fluorescence and a LO, which was frequency shifted tens of MHz with respect to the excitation laser field. The spectrum showed the resolved sidebands and the carrier transition with its elastically scattered photon peak.

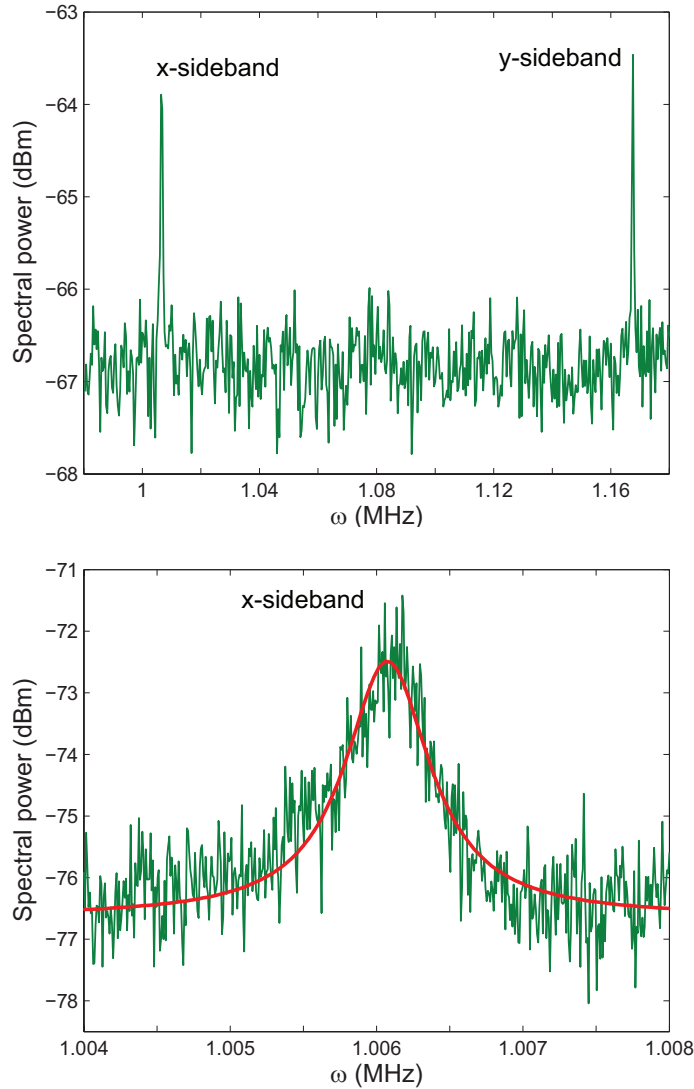


Figure 8.3: Spectrum of the homodyne signal of the resonance fluorescence with the ion position in the middle of the fringe for top graph: both radial x- and y-sidebands and bottom graph: x-sideband with Lorentzian fit.

8.3 First order correlation measurement

In this section the first-order coherence of a single radiating ion is measured up to a delay time τ of 29.6 ns. This is performed by successively increasing the mirror-ion distance and observing the variation of the homodyne visibility. As indicated by Eq. (8.5) the visibility then directly represents the absolute value of the $g^{(1)}(\tau)$ -

function of the resonance fluorescence.

An illustration of the experimental apparatus is presented in Fig. 8.4. A part of the

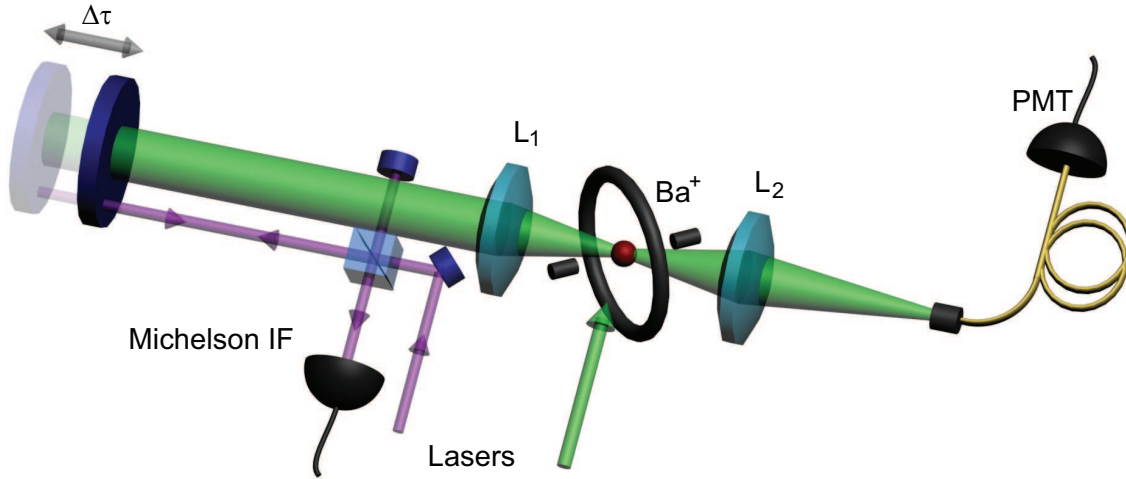


Figure 8.4: Sketch of the experimental setup for the first order correlation measurement along with the auxiliary laser interferometer placed into the mirror channel (see text for detail).

ion's fluorescence is collected by the objective L_1 and sent to a distant Piezo mounted mirror, from where the light is reflected back onto the ion. The back-reflected and the directly emitted light fields are then collected by the objective L_2 and guided to a PMT. In order to achieve an identical degree of mode matching, when measuring at different mirror-ion positions, the light along the detection channel is coupled to a single-mode fiber before being detected on the PMT, i.e. the fiber guarantees a reproducible spatial matching of the Gaussian modes of the directly emitted and back-reflected light path.

In order to deduce the phase stability of the mirror channel a Michelson interferometer is placed right behind the vacuum apparatus using the Piezo mirror as one arm. The interferometer is operated with 493 nm laser light. Monitoring the intensity at the output port with an oscilloscope we still record a visibility of 94% for the farthest mirror distance of 4.45 m away from the ion with a phase stability on the order of tens of seconds. The stability remains despite the necessity to fold the mirror-channel with two additional mirrors at this distance.

Due to this measurement we can neglect decreases in the visibility for the fluorescence $g^{(1)}(\tau)$ -measurement due to additional acoustic vibrations of the breadboard when the mirror-ion distance is increased.

In a next calibration step we record and fit a $g^{(2)}(\tau)$ -function of the ion's fluorescence. From this measurement we retrieve the dominant experimental parameters,

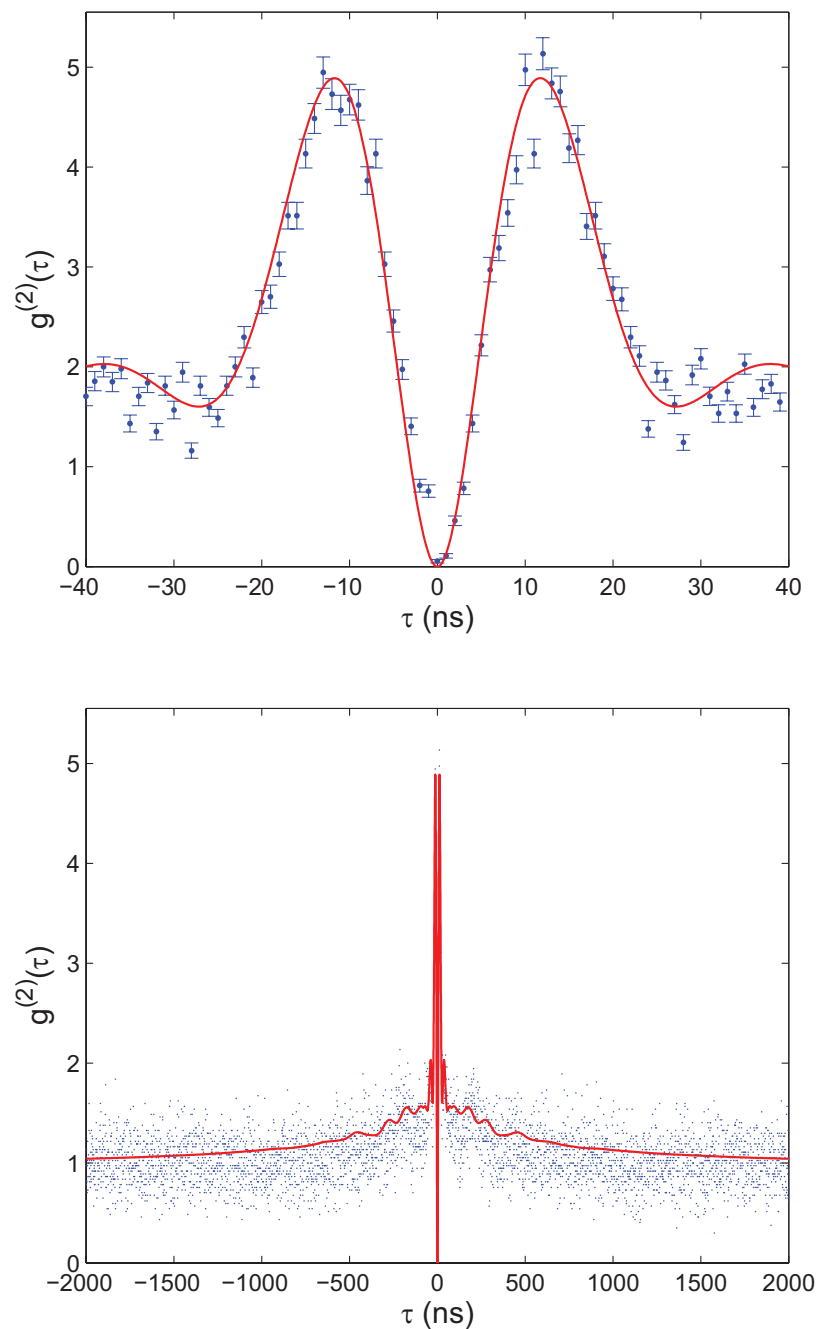


Figure 8.5: Measured second order correlation function when the mirror channel is blocked for smaller τ values (top graph) and longer τ values (bottom graph). The solid line shows the theoretical fit using 8-level Bloch equations.)

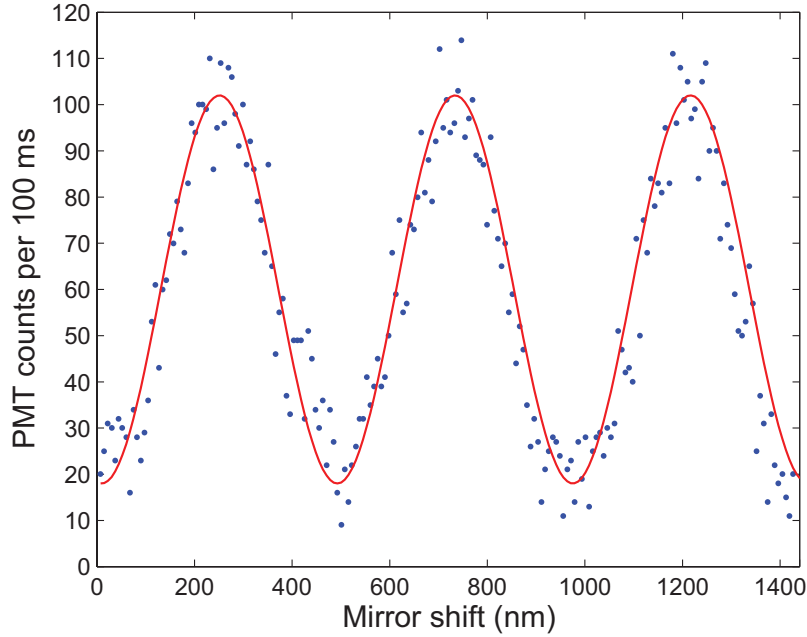


Figure 8.6: Sinusoidal dependence of the homodyne count rate after the fiber for a mirror shift of several wavelengths measured for a mirror round trip time of 2.3 ns. The fitted visibility is $V = 70.4(1.8)\%$

such as intensities and detunings of the lasers. The intensity correlation is obtained with the mirror channel blocked and is presented in Fig. 8.5 for an integration time of 2 h. The top graph depicts $g^{(2)}(\tau)$ in the vicinity of $\tau = 0$, while the bottom graph shows the same curve for longer τ values. The solid line represents the fitted curve using the 8-level Bloch model.

The evolution of the $|g^{(1)}(\tau)|$ is then gained by successively acquiring the visibility values of the homodyne intensity at various mirror-ion distances.

Starting well in the Markovian regime $\tau = 2D/c \ll 1/\Gamma_L$ with a closest mirror distance of 35 cm the visibility is recorded for eight points up to a mirror distance of 4.45 m. The last point corresponds then to a round-trip time of the light field in the mirror channel of 29.6 ns. Figure 8.6 hereby shows the obtained interference fringe for the closest measured distance of 35 cm (2.3 ns round trip time). The mirror is shifted linearly over several wavelengths and the sinusoidal dependence of the homodyne signal is recorded after the fiber. The fitted curve reveals a visibility of $V = 70.4(1.8)\%$. As indicated in Eq. (8.5) this value is mainly limited by non-optimal cooling conditions and thus an extended motional wavepacket of the ion. Further

limitations can arise due to diffraction at the aperture of objective L_1 leading to imperfect phase-front curvatures between the back-reflected and the directly emitted light towards the detector. Nevertheless, since all parameters are kept constant over the duration of the entire experiment, the non-interfering fraction of the homodyne signal can be assumed to be identical for all measured mirror distances.

The visibility values for the other mirror distances are then evaluated by sinusoidal fits of the recorded interference fringes similarly to Fig. 8.6. The extracted values are then presented in Fig. 8.7 with error bars indicating the respective standard deviations of the fits.

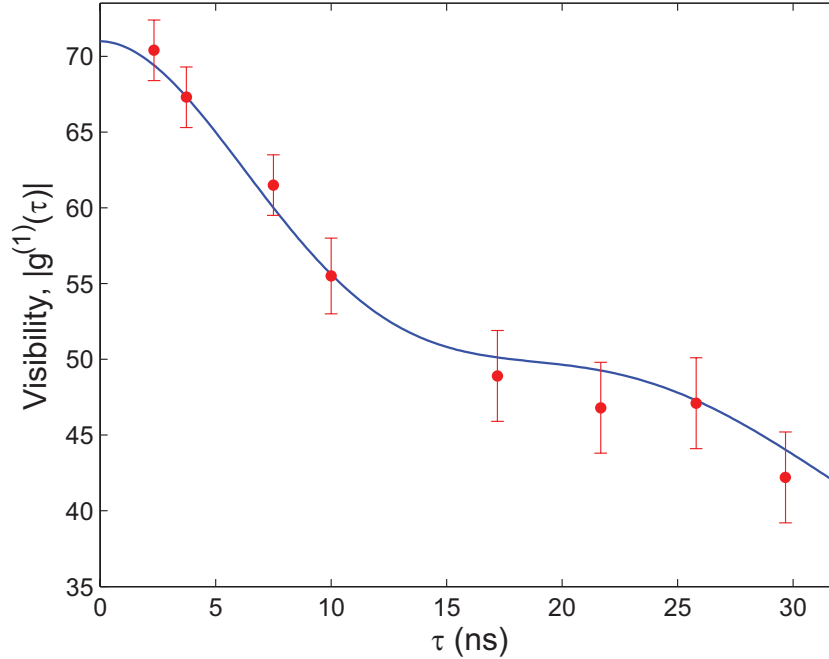


Figure 8.7: Obtained visibility values for various mirror-ion times delay τ . The solid line represent the theoretical scaled $|g^{(1)}(\tau)|$ -function as described by Eq. (8.5).

The solid line shows the scaled theoretical solution of the $|g^{(1)}(\tau)|$ correlation function using Bloch equations and the laser settings obtained from the preceding $g^{(2)}(\tau)$ measurement of Fig. 8.5. The scaling factor of the calculated curve is chosen to best match the data points.

From this graph we can now immediately infer that the first-order coherence of the fluorescence light drops steadily with the mirror-ion distance to about 60% of its initial value at a delay time τ of ~ 28 ns. The obtained data points of the $|g^{(1)}(\tau)|$ are herewith well reproduced by the theoretical model.

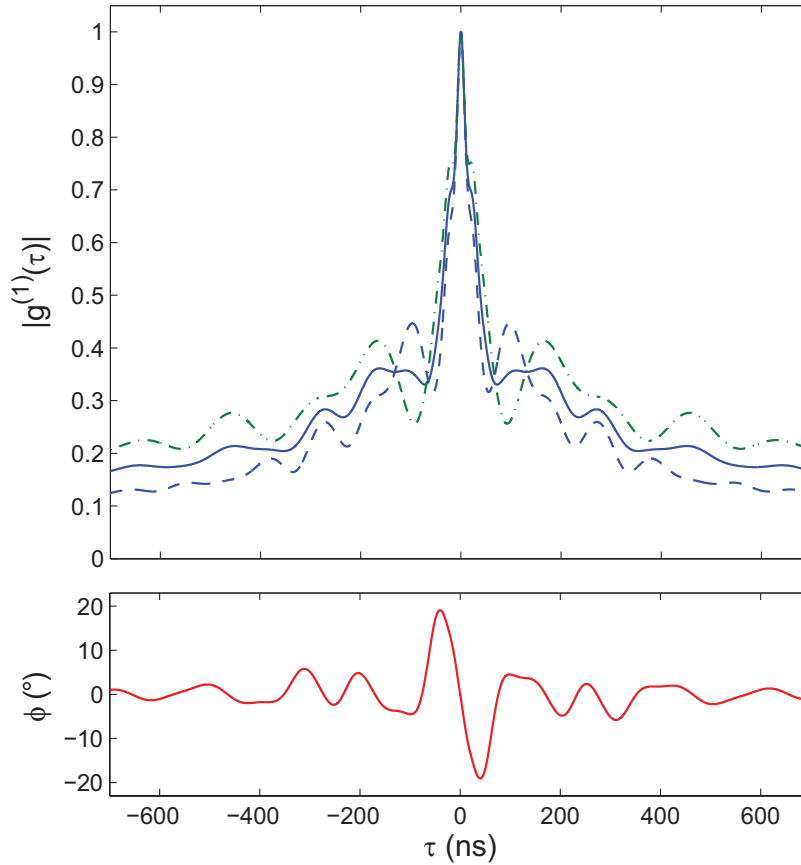


Figure 8.8: *Top graph:* Absolute value of the $g^{(1)}(\tau)$ -functions for different $|P_{1/2}\rangle \rightarrow |S_{1/2}\rangle$ transitions as described in the text. *Bottom graph:* Phase ϕ between the interfering fields obtained from the phase argument of $g^{(1)}(\tau)$.

To gain further information about the coherence properties of the emitted light we show the fitted $|g^{(1)}(\tau)|$ -function for even longer time delays. Its theoretical prediction is plotted in Fig. 8.8 for positive and negative τ values. In the top graph the solid lines represent the $|g^{(1)}(\tau)|$ -function for the present experimental situation, where we observe both $|P_{1/2}\rangle \rightarrow |S_{1/2}\rangle$ dipole transitions as discussed in Chap. 2. The absolute value is proportional to the amplitude of the interference as measured by a detector. For comparison, in the top graph the dashed line shows only $|g^{(1)}(\tau)|$ for the $|P_{1/2}, m = -1/2\rangle \rightarrow |S_{1/2}, m = +1/2\rangle$ transition, whereas the dashed-dotted line represents the $|g^{(1)}(\tau)|$ for the $|P_{1/2}, m = +1/2\rangle \rightarrow |S_{1/2}, m = -1/2\rangle$ transition. As described in the theoretical part of this thesis the individual first-order correlations are then given for positive and negative delay times τ by Eq. (3.29) and Eq. (3.30),

respectively. Furthermore, the solid line deduces then as the normalized incoherent sum of the two individual transition curves given by Eq. (3.29). Note that the small difference in the curves between the two involved $\Delta m \pm 1$ transitions originates from the different frequency shifts of the Zeeman splitting, and along with that the different laser detuning, the two transitions are exposed to (see Eq. (2.4)).

The bottom graph of Fig. 8.8 depicts ϕ as given by the phase argument of the complex $g^{(1)}(\tau)$ -function considering both dipole transitions. ϕ then represents the phase relation at different delay times between the two fluctuating fields constituting the homodyne signal.

From this theoretical plot we hence deduce that $\sim 65\%$ of coherence is lost within the first 100 ns before the coherence smoothes out slowly at a positive value of $|g^{(1)}(\tau = 0.7\mu\text{s})| \simeq 0.15$. The coherence then stabilizes at the value of 8%, as given by the first order coherence obtained at steady state as

$$g^{(1)}(\infty) = \lim_{\tau \rightarrow \infty} \frac{\langle \hat{\sigma}^- e^{\mathcal{L}\tau} (\hat{\rho}_{ss} \hat{\sigma}^+) \rangle}{\langle \hat{\sigma}^- \hat{\sigma}^+ \hat{\rho}_{ss} \rangle}. \quad (8.9)$$

Recalling Eq. (3.20) together with Eq. (8.6) we note that this asymptotic value of $|g^{(1)}(\tau \rightarrow \infty)|$ directly yields the ratio of the elastically scattered intensity to the total scattered intensity. Thus, from the theoretical plot we can deduce, for the present set of experimental parameters, that the elastically scattered intensity of the fluorescence is about 8%. At the same time this finding indicates that the major contribution of the fluorescence light is incoherently scattered.

From the first-order correlation function we can further derive the power spectral density $F(\omega)$ of the fluorescence as discussed in Sec. 3.1. This is performed by taking the Fourier-transform of the $g^{(1)}(\tau)$ -function, which is discussed above. The result is plotted in Fig. 8.9, where ω_L is the incident laser frequency. Due to the laser detunings the inelastically scattered part of the spectrum exhibits an asymmetry towards lower frequencies. In addition, the elastically scattered components are directly proportional to $\delta(\omega - \omega_L)$.

Conclusion

In summary we have successfully measured the absolute value of the first order coherence of the resonance fluorescence up to a delay time of 29.6 ns. This is performed by directly recording the visibility values of the interference fringe between a radiating single ion and its mirror image. The $|g^{(1)}(\tau)|$ is found in good agreement with the theoretical prediction. The laser parameters entering the theoretical model are deduced from the fit of a $g^{(2)}(\tau)$ correlation function.

From the shape of the $|g^{(1)}(\tau)|$ we were able to infer the temporal coherence of the

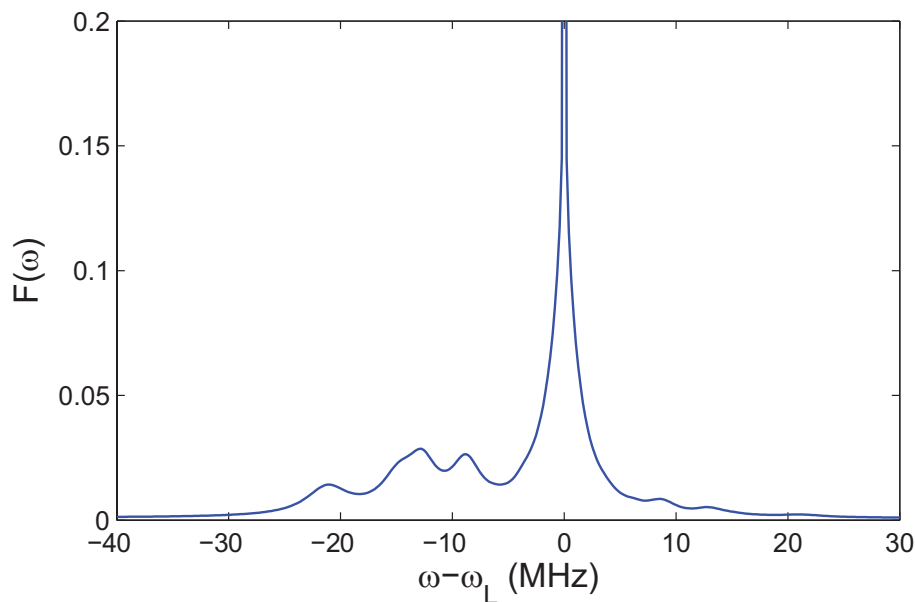


Figure 8.9: Power spectral density $F(\omega)$ obtained by taking the Fourier transformation of the theoretical $g^{(1)}(\tau)$ correlation function.

emitted light under observed experimental conditions. Additionally we estimated the contribution of elastically scattered photons in the fluorescence to be 8%.

8.4 Two ions in front of a mirror

The main motivation of the following chapter is the future goal to observe super- or subradiance effects on the joint fluorescence of two or more ions. The coupling from one atomic system to the other is realized with via a photonic channel. A well suited system to investigate this concept consists of two ions located in the same trap and interacting with each other via the mirror channel as described above. In general, one would expect to observe a change in the collective fluorescence intensity together with an enhancement or decrease in the individual spontaneous emission rates depending on the photonic mode density between the ions and their mirror images. Since the emission rates go hand in hand with the excited state populations one possible method to examine this system is via second-order correlation functions. This problem was recently approached theoretically by [104]. An alternative approach to gain access to the excited state population is by simultaneous observation of the red and green fluorescence in a similar way as performed in [31,99]. In [31] an experiment with a single ion in front of a mirror showed a variation of the excited

state population of 0.9% indicated by the red fluorescence fringe in anti-correlation with the green fluorescence fringe. The latter fringe visibility was measured there to be 47% during this experiment. While this method is not pursued here this investigation points towards a high requirement for the green visibility in order to be able to observe effects on the excited state populations.

In this section we show a first experimental characterization of two ions in front of a mirror. Using the linear trap apparatus we implement spatial filtering of the fluorescence for only one ion. We then observe the visibility for the cases, where the fluorescence is back-reflected onto the same ion and onto the other ion.

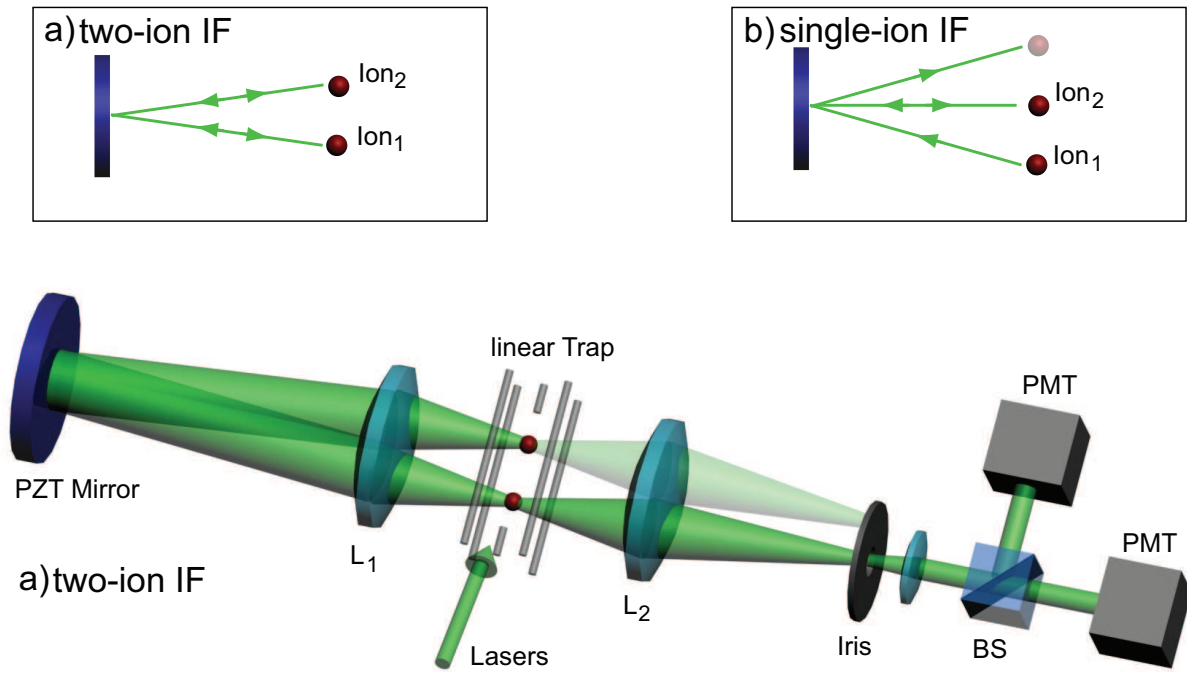


Figure 8.10: Sketch of the experimental setup of two ions, 1 and 2, situated in the linear trap, where the light scattered into the mirror channel is a) back-reflected onto each other resulting in a two-ion interference and is b) backreflected onto the same ion resulting into a single-ion interference.

Figure 8.10 depicts the two mentioned situations with a detailed sketch showing the two-ion interference. Two objectives L_1 and L_2 collect the fluorescence on the left and right side of the trap with a numerical aperture of 0.4 each (see Sec. 5.1.1). For the situation Fig. 8.10 a) a single PMT or a HBT-setup in the detection channel records the light directly emitted from ion 1 overlapped with the back-reflected light

from ion 2. The directly emitted light from ion 2 is filtered out using a slit iris⁴ at the focus of L_2 . In this situation we have to consider the geometrical fact that, in addition to the mirror-ion distance D , the two ions are located at different positions within the driving laser fields. Thus, the atomic dipoles from the ions oscillate with a certain phase shift with respect to each other given by l/λ , where l is the ion distance along the laser propagation direction. In the linear trap this length is on the order of $4 \mu\text{m}$. When we now consider the case where the two ions emit into the same spatial mode along the mirror channel their electric field operators, describing the radiation processes, will therefore exhibit different time evolutions. One ion will have an initial time offset d/c with respect to the other with d denoting the ions distance perpendicular to the mirror axis. The effective mirror channel round trip time of ion 2 is then given by $\tau = 2D_{\text{eff}}/c$ with $D_{\text{eff}} = \sqrt{D^2 + (d/2)^2}$. Nevertheless, since $d \ll D$ we can assume for the following analysis that $D_{\text{eff}} = D$.

For the case as pictured in Fig. 8.10 a) electric fields can hence be expressed as $\hat{E}_1^+(t)$ and $\hat{E}_2^+(t+d/c+\tau)$ for ion 1 and 2, respectively. For simplicity we will further define τ as $\tau = d/c + 2D/c$.

Note that in principle this phase-shift in dependence of the ion separation distance could be observable in the linear trap by recording a variation of the interference fringe as a function of the tip voltages. But in doing so the cooling conditions and trap frequencies would heavily alter as well, making this task demanding.

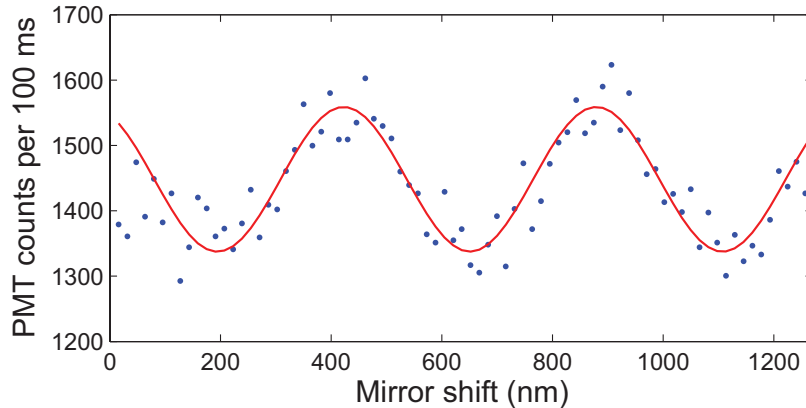


Figure 8.11: Recorded fringe of two-ion interference as illustrated in Fig. 8.10 a). The solid line shows a sinusoidal fit with $V = 7.8(2)\%$

To compare the following results of two-ion interference, we first concentrate onto the situation of the single-ion interference as illustrated in Fig. 8.10 b). Here, we

⁴Owis, SP 60

observe a maximally reached visibility of about 32%. This number does not rise notably when only one ion is loaded into the trap. This indicates that we can neglect higher motional occupations and thus have to include a stronger micromotion for the case of two ions in the linear trap. We also notice that this reached visibility is considerably lower than the single-photon interference reached with the ring trap apparatus. Comparing at this point the reached $\sim 32\%$ with the findings of [31, 52] as mentioned above (change of the excited state decay rates of $\sim 0.9\%$ at a visibility of 47%) we can assume for now to have a negligible small variation of the ion's decay rates for the current experiment.

Figure 8.11 depicts the intensity fringe when the mirror is scanned for the case of the two-ion interference from Fig. 8.10 a). A sinusoidal fit reveals a visibility of $V = 7.8(2)\%$. This drop from $\sim 32\%$ for the case of the single-ion interference is understood, when we calculate the expected homodyne signal. Here, we start by denoting the collective electric field operator as

$$\widehat{E}_{ges}^+(t, \tau) = \widehat{E}_1^+(t) + \widehat{E}_2^+(t + \tau), \quad (8.10)$$

which yields an intensity at the detector as

$$\begin{aligned} I &= \langle \widehat{E}_{ges}^+(t, \tau) \widehat{E}_{ges}^-(t, \tau) \rangle \\ &= \langle \widehat{E}_1^+(t) \widehat{E}_1^-(t) \rangle + \langle \widehat{E}_2^+(t + \tau) \widehat{E}_2^-(t + \tau) \rangle \\ &\quad + \langle \widehat{E}_1^+(t) \widehat{E}_2^-(t + \tau) \rangle + \langle \widehat{E}_2^+(t + \tau) \widehat{E}_1^-(t) \rangle. \end{aligned} \quad (8.11)$$

Considering Eq. (3.24) and Eq. (3.25) the electric fields can be expressed in terms of Pauli lowering operators as $\widehat{E}_i^+(t) = \eta_i e^{i\omega_L t} [\hat{\sigma}_{i,+}^-(t) \vec{e}_{i,+} + \hat{\sigma}_{i,-}^-(t) \vec{e}_{i,-}]$. This leads to an intensity I of

$$\begin{aligned} I &= \eta e^{i\omega_L t} \left[\langle \hat{\sigma}_{1,+}^-(t) \hat{\sigma}_{1,+}^+(t) \rangle + \langle \hat{\sigma}_{1,-}^-(t) \hat{\sigma}_{1,-}^+(t) \rangle \right. \\ &\quad + \langle \hat{\sigma}_{2,+}^-(t + \tau) \hat{\sigma}_{2,+}^+(t + \tau) \rangle + \langle \hat{\sigma}_{2,-}^-(t + \tau) \hat{\sigma}_{2,-}^+(t + \tau) \rangle \\ &\quad + \langle \hat{\sigma}_{1,+}^-(t) \hat{\sigma}_{2,+}^+(t + \tau) e^{-i\omega_L(\tau)} \rangle + \langle \hat{\sigma}_{1,-}^-(t) \hat{\sigma}_{2,-}^+(t + \tau) e^{-i\omega_L(\tau)} \rangle \\ &\quad \left. + \langle \hat{\sigma}_{2,+}^-(t) \hat{\sigma}_{1,+}^+(t + \tau) e^{i\omega_L(\tau)} \rangle + \langle \hat{\sigma}_{2,-}^-(t) \hat{\sigma}_{1,-}^+(t + \tau) e^{i\omega_L(\tau)} \rangle \right], \end{aligned} \quad (8.12)$$

where η denotes a constant amplitude incorporating the overall collection and detection efficiency. The first four terms represent the measured intensities of the individual ions, where the remaining four terms indicate the possible interaction between the ions. Note that since the two involved $|P_{1/2}\rangle \rightarrow |S_{1/2}\rangle$ transitions have orthogonal polarizations cross terms as $\langle \hat{\sigma}_{1,+}^-(t) \hat{\sigma}_{2,-}^+(t + \tau) e^{-i\omega_L(\tau)} \rangle$ are identical zero. Only cross terms with identical polarization contribute to the interference. However, in those cases we have to additionally incorporate the individual phases of the radiated fields of ion 1 and ion 2. Since the homodyne intensity is recorded under steady state conditions of the ions with an integration time

much greater than the lifetime of the excited state, the phase difference between the atomic dipoles of ion 1 and ion 2 has to be averaged over all possible values. This is then expressed, similarly as in Eq.(3.19), by rewriting the cross terms as $\langle \hat{\sigma}_{1,+}^-(t) \hat{\sigma}_{2,+}^+(t + \tau) e^{-i\omega_L(\tau)} \rangle = \langle \hat{\sigma}_{1,+}^-(t) \rangle \langle \hat{\sigma}_{2,-}^+(t + \tau) e^{-i\omega_L(\tau)} \rangle$. Hence, only the elastically scattered fraction of the fluorescence, with a phase inherited by the excitation laser, will interfere and contribute to the measurement process.

Assuming now identical emission properties for ion 1 and ion 2 the expected homodyne intensity simplifies to

$$I = 2[I + \cos(\omega_L \tau) I_{elas}], \quad (8.13)$$

where the elastically scattered intensity I_{elas} is given in accordance to Eq.(3.20).

Conclusion

Summarizing, we studied the system of 2 ions in front of a distant mirror using the linear trap apparatus. By implementing spatial filtering we could select for the light of one ion, while blocking the other.

In this setup we found a visibility for the case of the single-ion interference of 32% and 7.8% in the case of the two-ion interference. In the latter case this value directly represents the elastically scattered intensity of the ion's fluorescence.

Future investigations along this line of experiments to visualize super- and sub-radiance effect place the need for higher visibility values. This could, for example, be realized by combining a pulsed operation scheme of the lasers together with an increase of the numerical aperture of the fluorescence objectives. On a longer time scale a new experimental setup is planned with a miniaturized linear trap design that could house higher NA objectives with estimated NA of 0.75 when optimized for the 493 nm fluorescence.

Chapter 9

Summary and Outlook

This thesis presents a variety of experiments characterizing the resonance fluorescence emitted by single barium ions. The ions were stored in a ring trap or a linear Paul trap apparatus, where they were excited with continuous lasers and Doppler-cooled to the Lamb-Dicke regime. Their resonance fluorescence on the $|S_{1/2}\rangle \rightarrow |P_{1/2}\rangle$ transition was collected and investigated. Using this system fundamental quantum optic experiments were carried out obtaining statistical information from the fluorescence light by measuring time-like correlation functions.

The expounded work started by describing the fundamental theoretical tools for the experimental situation of a trapped ion interacting with a coherent laser field. This part was followed by a discussion of the laboratory setups and experimental methodologies and routines.

Subsequently, a series of conducted experiments was presented starting with the measurement of the two-photon interference at a beam splitter in chapter 6. Here, the indistinguishability of the two-photon interference place an essential role for the experimental implementation of several entanglement protocols [21,85,86]. Towards this line the two-photon interference for the situation of two radiating ions situated in distinct trap was quantitatively treated. The system was investigated by a Houg-Ou and Mandel type interference by correlating the arrival times of the emitted photons from the two ions. Yielding an indistinguishability of 89(2)% this experiment directed towards the application of atom-photon interfaces using barium ions as a candidate for the realization of quantum networks.

In chapter 7 the first experimental realization of recording the conditioned time evolution of the source field of the radiating dipole of a single trapped atom was presented. This was conducted by recording an intensity-field correlation function, which combined the techniques of a homodyne detector and an intensity correlator. Here, a photon detection from the ion prepared the correlation measurement in a well defined state. From there the temporal evolution of the electromagnetic wave with respect to a local oscillator back to equilibrium via Rabi oscillations was observed. The real and imaginary contribution of this correlation function were then deduced from acquired data collected at three different phases of the local oscillator.

The temporal coherence of the fluorescence, thus its ability to interfere, is accessible by the first-order auto-correlation function. As an important characterization of the emitted light of an ion, this quantity was obtained up to delay times of 29.6 ns with a system consisting of an ion in front of a distant mirror equivalent to a half-cavity setup. This setup was discussed in chapter 8 and implemented a Michelson type interferometer, where the self-homodyne signal measured the first-order coherence of the fluorescence. Thus, by increasing the ion-mirror distance we directly recorded the absolute value of the first order correlation function of the scattered light. In addition, this setup was adopted to study the situation of two ions located in the same trap interacting via the photonic mirror channel. Here, the interference signal yielded the elastically scattered fraction of the ion's fluorescence. As such a system enables the possibility to observe super- and subradiance effects of the joint fluorescence further investigations along this line of experiments are planned.

Whereas in this last chapter the ion was studied with an experimental boundary condition that was provided by a mirror that back-reflects part of the fluorescence, a future approach would be to study the environmental influence on the ion extended to movable boundary conditions. The homodyne setup with a fast oscillating mirror or a phase modulating electro-optical modulator in the mirror-channel path seems to be a suitable setup to implement this scheme [105]. In this approach it is expected that the reflected Stokes and anti-Stokes shifted sideband photons from the mirror will have an appreciable effect on the center of mass motion of the ion, especially in the non-Markovian regime. For such a system cooling or heating effects are anticipated with even the possibilities to include motional degrees of freedom of the mirror in the sense of a micro-mechanical oscillator. Additionally, a possible extension along this line would be to take into account Casimir-photons, created by the oscillating mirror, where their effects could be investigated on the motional state of the trapped ion.

For all these planned and performed experiments, however, an intrinsic limitation is determined by the collected solid angle of the resonance fluorescence. In this respect estimations indicate that a miniaturized ring or linear Paul trap could house close-by objectives with a NA in the order of 0.75, when optimized for low wavefront distortion of the $S_{1/2} \rightarrow P_{1/2}$ fluorescence. Hence, they would cover a factor of 4 more solid angles as compared with the objectives in the current apparatuses. With a higher collection efficiency along the mirror channel setup the influence of the back-reflected light onto the ion and its internal dynamics would greatly benefit considering the current limitation of the change in decay rates on the order of one percent [31]. In addition, the enhanced fluorescence signals would open new directions of observing an ion under weak laser excitation. Entering this regime would allow us to visualize squeezing effects e.g. in the Fourier transform of an

intensity-field correlation function. Here, squeezing of the fluorescence modulated at the Rabi frequency could be observed [32, 33]. Besides this the observation of squeezing of one light quadrature below the shot noise would be possible e.g. at a beam splitter with a local oscillator at one input port [106].

Bibliography

- [1] J. Fraunhofer, *Bestimmung des Brechungs- und Farbzerstreuungsvermögens vers. Glasarten, in Bezug auf die Vervollkommnung achromatischer Fernrohre*, Gilbert's Ann. **56**, 264 (1817).
- [2] R. Bunsen, G. Kirchhoff, *Untersuchung über das Sonnenspektrum und die Spektren in Chemischen Elementen*, Abh. königl. Akad. Wiss. (1861).
- [3] J. C. Maxwell, *A Treatise on Electricity and Magnetism*, Clarendon Press, Oxford (1873).
- [4] M. Planck, *Zur Theorie des Gesetzes der Energieverteilung im Normalspektrum*, Verh. Dtsch. Phys. Ges. **2**, 237 (1900).
- [5] N. Bohr, *On the Constitution of Atoms and Molecules*, Philos. Mag. **26**, 1 (1913).
- [6] T. H. Maiman, *Stimulated Optical Radiation in Ruby*, Nature **187**, 493 (1960).
- [7] W. Neuhauser, M. Hohenstatt, P. Toschek, and H. Dehmelt, *Optical-Sideband Cooling of Visible Atom Cloud Confined in Parabolic Well*, Phys. Rev. Lett. **41**, 233 (1978).
- [8] W. Paul, *Ein neues Massenspektrometer ohne Magnetfeld*, Z. Naturforsch. **A8**, 448 (1953).
- [9] D. J. Wineland and W. M. Itano, *spectroscopy of a single Mg^+ ion*, Phys. Rev. A, **82**, 75 (1981).
- [10] D. J. Wineland, and H. Dehmelt, *Proposed $1014 \Delta\nu < \nu$ laser fluorescence spectroscopy on Tl^+ mono-ion oscillator III*, Bull. Am. Phys. Soc. **20**, 637, (1975).
- [11] R. Feynman, *Quantum mechanical computers*, Opt. News **11**, 11 (1985).
- [12] P. Benioff, *Quantum mechanical models of Turing machine that dissipate no energy*, Phys. Rev. Lett. **48**, 1581 (1982).

- [13] J. I. Cirac and P. Zoller, *Quantum Computations with Cold Trapped Ions*, Phys. Rev. Lett. **74**, 4091 (1995).
- [14] J. I. Cirac, P. Zoller, H. J. Kimble, and H. Mabuchi, *Quantum State Transfer and Entanglement Distribution among Distant Nodes in a Quantum Network*, Phys. Rev. Lett. **78**, 3221 (1997).
- [15] H. Häffner, W. Hansel, C. F. Roos, J. Benhelm, D. Chek-al-kar, M. Chwalla, T. Korber, U. D. Rapol, M. Riebe, P. O. Schmidt, C. Becher, O. Guhne, W. Dur, and R. Blatt, *Scalable multiparticle entanglement of trapped ions*, Nature **438**, 643 (2005).
- [16] F. Schmidt-Kaler, H. Häffner, M. Riebe, S. Gulde, G. P. T. Lancaster, T. Deuschle, C. Becher, C. F. Roos, J. Eschner, and R. Blatt, *Realization of the Cirac-Zoller controlled-NOT quantum gate*, Nature **422**, 408 (2003).
- [17] D. Leibfried, B. DeMarco, V. Meyer, W. M. Itano, B. Jelenkovic, C. Langer, T. Rosenband and D. Wineland, *Experimental demonstration of a robust, high-fidelity geometric two ion-qubit phase gate*, Nature **422**, 412 (2003).
- [18] R. Ursin, F. Tiefenbacher, T. Schmitt-Manderbach, H. Meier, T. Scheidl, M. Linderthal, B. Blauensteiner, T. Jennewein, J. Perdigues, P. Trojek, B. Oemer, M. Fuerst, M. Meyenburg, J. Rarity, Z. Sodnik, C. Barbieri, H. Weinfurter and A. Zeilinger, *Entanglement-based quantum communication over 144 km*, Nat. Phys. **3**, 481 (2007).
- [19] I. Marcikic, H. de Riedmatten, W. Tittel, H. Zbinden, M. Legre and N. Gisin, *Distribution of time-bin entangled qubits over 50 km of optical fiber*, Phys. Rev. Lett. **93**, 180502 (2004).
- [20] C. Cabrillo, J. I. Cirac, P. Garcia-Fernandez and P. Zoller, *Creation of entangled states of distant atoms by interference*, Phys. Rev. A **59**, 1025 (1999).
- [21] C. Simon, W. T. M. Irvine, *Robust long-distance entanglement and a loophole-free Bell test with ions and photons*, Phys. Rev. Lett. **91**, 110405 (2003).
- [22] D. L. Moehring, P. Maunz, S. Olmschenk, K. C. Younge, D. N. Matsukevich, L. M. Duan and C. Monroe, *Entanglement of single-atom quantum bits at a distance*, Nature **449**, 68 (2007).
- [23] T. Wilk, S. C. Webster, A. Kuhn and G. Rempe, *Single-atom single-photon quantum interface*, Science **317**, 27 (2007).

-
- [24] A. D. Boozer, A. Boca, R. Miller, T. E. Northup, and H. J. Kimble, *Reversible state transfer between light and a single trapped atom*, Phys. Rev. Lett. **98**, 193601 (2007).
- [25] J. M. Raimond, M. Brune, and S. Haroche, *Manipulating quantum entanglement with atoms and photons in a cavity*, Rev. Mod. Phys. **73**, 565 (2001).
- [26] R. Hanbury Brown, and R. Q. Twiss, *Question of correlation between photons in coherent light rays*, Nature (London) **177** 27 (1956).
- [27] R. Hanbury Brown, and R. Q. Twiss, *A Test of a New Type of Stellar Interferometer on Sirius*, Nature (London) **178** 1046 (1956).
- [28] H. J. Kimble, M. Dagenais, and L. Mandel, *Photon Antibunching in Resonance Fluorescence*, Phys. Rev. Lett. **39**, 691 (1977).
- [29] R. Short and L. Mandel, *Observation of Sub-Poissonian Photon Statistics*, Phys. Rev. Lett. **51**, 5 (1983).
- [30] A. A. Michelson and E. W. Morley, *On the Relative Motion of the Earth and the Luminiferous Ether*, Am. J. Sci. **34**, 333 (1887).
- [31] J. Eschner, Ch. Raab, F. Schmidt-Kaler and R. Blatt, *Light interference from single atoms and their mirror images*, Nature **413**, 495 (2001).
- [32] H. J. Carmichael, H. M. Castro-Beltran, G. T. Foster, and L. A. Orozco, *Giant Violations of Classical Inequalities through Conditional Homodyne Detection of the Quadrature Amplitudes of Light* Phys. Rev. Lett **85**, 1855 (2000).
- [33] G. T. Foster, L. A. Orozco, H. M. Castro-Beltran, and H. J. Carmichael, *Quantum State Reduction and Conditional Time Evolution of Wave-Particle Correlations in Cavity QED*, Phys. Rev. Lett **85**, 3149 (2000).
- [34] C. K. Hong, Z. Y. Ou and L. Mandel, *Measurement of Subpicosecond Time Intervals between Two Photons by Interference*, Phys. Rev. Lett. **59**, 2044 (1987).
- [35] H. Oberst, *Resonance fluorescence of single Bariumions*, Diploma Thesis, University of Innsbruck (1999).
- [36] NIST, *Basic atomic and spectroscopic data*, Online database, <http://physics.nist.gov/PhysRefData/ASD/index.html>
- [37] D. R. Lide, *Handbook of chemistry and physics, 78th edition*, CRC Press (1997-1998).

- [38] R. Loudon, *The Quantum Theory of Light*, Clarendon Press, Oxford (1983).
- [39] P. A. M. Dirac, *The Quantum Theory of the Emission and Absorption of Radiation*, Proc. R. Soc. Lond. A **114**, 243 (1927).
- [40] S. M. Tan, *A computational toolbox for quantum and atomic optics*, Journal of Optics B: Quantum and Semiclassical Optics **1**, 424 (1999).
- [41] M. Born and E. Wolf, *Principles of Optics*, Pergamon Press, Reprint (1993).
- [42] Marlan O. Scully and M. Suhail Zubairy, *Quantum Optics*, Cambridge University Press, Cambridge (1997).
- [43] H. Carmichael, *An open systems approach to quantum optics*, Springer Press (1993).
- [44] B. R. Mollow, *Power Spectrum of Light Scattered by Two-Level Systems*, Phys. Rev. **188**, (1969).
- [45] C. Cohen-Tannoudji, *Atom-photon interaction*, A Wiley-interscience publication, New York, (1992).
- [46] Y. Stalgies, I. Siemers, B. Appasamy, T. Altevogt and P. E. Toschek, *The spectrum of single-atom resonance fluorescence*, Europhys. Lett. **35**, 259 (1996).
- [47] L. Mandel, E. Wolf, *Optical Coherence and Quantum Optics* (Cambridge University Press, Boston, 1995).
- [48] J. H. Kimble, M. Dagenais, and L. Mandel, *Photon Antibunching in Resonance Fluorescence*, Phys. Rev. Lett **39**, 691 (1977).
- [49] F. Diedrich, and H. Walther, *Nonclassical radiation of a single stored ion*, Phys. Rev. Lett **58**, 203 (1987).
- [50] M. Schubert, I. Siemers, R. Blatt, W. Neuhauser, and P. E. Toschek, *Photon antibunching and non-Poissonian fluorescence of a single three-level ion*, Phys. Rev. Lett **68**, 3016 (1992).
- [51] D. Leibfried, R. Blatt, C. Monroe, and D. Wineland, *Quantum dynamics of single trapped ions*, Rev. Mod. Phys. **75**, 281 (2003).
- [52] Ch. Raab, *Interference experiments with the fluorescence light of Ba⁺ ions*, Ph.D Thesis, University of Innsbruck (2001).
- [53] Ch. Roos, *Controlling the Quantum State of Trapped Ions*, Ph.D Thesis, University of Innsbruck (2000).

-
- [54] D. Rotter, *Quantum feedback and quantum correlation measurements with a single Barium ion*, Ph.D Thesis, University of Innsbruck (2008).
- [55] J. Bolle, *Spektroskopie und nichtklassische Fluoreszenzeigenschaften von einzelnen gespeicherten Barium-Ionen*, Ph.D Thesis, University of Innsbruck (1998).
- [56] R. W. P. Drever, J. L. Hall and F. V. Kowalski, *Laser phase and frequency stabilization using an optical resonator*, Appl. Phys. B **31**, 97 (1983).
- [57] L. S. Ma, Ph. Courteille, G. Ritter, W. Neuhauser and R. Blatt, *Spectroscopy of Te_2 with modulation transfer: Reference lines for precision spectroscopy in Yb^+ at 467 nm*, Appl. Phys. B **57**, 683 (1993).
- [58] P. Bushev, *Interference experiments with a single Barium ion: From QED towards quantum feedback*, Ph.D Thesis, University of Innsbruck (2004).
- [59] D. Berkeland, J. D. Miller, J. C. Bergquist, W. M. Itano, and D. J. Wineland, *Minimization of ion micromotion in a Paul trap*. J. Appl. Phys. **83**, 5025 (1998).
- [60] D. Rotter, M. Mukherjee, F. Dubin and R. Blatt, *Monitoring a single ion's motion by second-order photon correlations*, New J. Phys. **10**, 043011 (2008).
- [61] J. D. Weinstein, R. deCarvalho, T. Guillet, B. Friedrich and J. M. Doyle, *Magnetic trapping of calcium monohydride molecules at millikelvin temperatures* Phys. Rev. A **66**, 030702 (1998).
- [62] H. Gilhaus, Th. Sauter, W. Neuhauser, R. Blatt and P. E. Toschek, *On the light force upon a single trapped three-level ion*, Opt. Commun. **69**, 25 (1988).
- [63] S. van der Meer, *Stochastic cooling and the accumulation of antiprotons*, Rev. Mod. Phys. **57**, 689 (1985).
- [64] J. I. Cirac, L. J. Garay, R. Blatt, A. S. Parkins and P. Zoller, *Laser cooling of trapped ions: The influence of micromotion*, Phys. Rev. A **49**, 421 (1993).
- [65] C. Monroe, D. M. Meekhof, B. E. King, S. R. Jefferts, W. M. Itano, and D. J. Wineland, *Resolved-Sideband Raman Cooling of a Bound Atom to the 3D Zero-Point Energy*, Phys. Rev. Lett. **75**, 4011 (1995).
- [66] S. Stenholm, *The semiclassical theory of laser cooling*, Rev. Mod. Phys. **58**, 699 (1986).
- [67] J. I. Cirac, R. Blatt, A. S. Parkins, and P. Zoller, *Spectrum Of Resonance Fluorescence From A Single Trapped Ion*, Phys. Rev. A **48**, 2169 (1993).

- [68] M. Lindberg, *Resonance Fluorescence Of A Laser-Cooled Trapped Ion In The Lamb-Dicke Limit*, Phys. Rev. A **34**, 3178 (1986).
- [69] P. Bushev, D. Rotter, A. Wilson, F. Dubin, Ch. Becher, J. Eschner, R. Blatt, V. Steixner, P. Rabl, and P. Zoller, *Feedback cooling of a single trapped ion*, Phys. Rev. Lett. **96**, 043003 (2006).
- [70] T. Legero, T. Wilk, A. Kuhn and G. Rempe, *Time-resolved two-photon quantum interference*, Appl. Phys. B **77**, 8 (2003).
- [71] S. Nußmann, M. Hijlkema, B. Weber, F. Rohde, G. Rempe, and A. Kuhn, *Submicron Positioning of Single Atoms in a Microcavity*, Phys. Rev. Lett. **95**, 173602 (2005).
- [72] M. Keller, B. Lange, K. Hayasaka, W. Lange, H. Walther, *Continuous generation of single photons with controlled waveform in an ion-trap cavity system*, Nature **431**, 1075 (2004).
- [73] B. Dayan, A. S. Parkins, T. Aoki, E. P. Ostby, K. J. Vahala, and H. J. Kimble, *A Photon Turnstile Dynamically Regulated by One Atom*, Science **319**, 1062 (2008).
- [74] D. N. Matsukevich, T. Chaneliere, M. Bhattacharva, S. Y. Lan, S. D. Jenkins, T. A. B. Kennedy, and A. Kuzmich, *Entanglement of a photon and a collective atomic excitation*, Phys. Rev. Lett **95**, 040405 (2005).
- [75] J. K. Thompson, J. Simon, H. Loh, and V. Vuletic, *A high-brightness source of narrowband, identical-photon pairs*, Science **313**, 74 (2006).
- [76] M. D. Eisaman et al., A. Andra, F. Massou, M. Fleischhauer, A. S. Zibrov and M. D. Lukin, *Electromagnetically induced transparency with tunable single-photon pulses*, Nature **438**, 837 (2005).
- [77] T. Chanelière, D. N. Matsukevitch, S. D. Jenkins, S. Y. Lan, T. A. B. Kennedy and A. Kuzmich, *Storage and retrieval of single photons transmitted between remote quantum memories*, Nature **438**, 833 (2005).
- [78] F. Dubin, D. Rotter, M. Mukherjee, S. Gerber, and R. Blatt, *Single-ion two-photon source*, Phys. Rev. Lett. **99**, 183001 (2007).
- [79] B. B. Blinov, D. L. Moehring, L. M. Duan, and C. Monroe, *Observation of entanglement between a single trapped atom and a single photon*, Nature **428**, 153 (2004).

-
- [80] J. Beugnon, M. P. A. Jones, J. Dingjan, B. Darquiére, G. Messin, A. Browaeys, and P. Grangier, *Quantum interference between two single photons emitted by independently trapped atoms*, *Nature* **440**, 779 (2006).
- [81] P. Maunz, D. L. Moehring, S. Olmschenk, K. C. Younge, D. N. Matsukevich, and C. Monroe, *Entanglement of single-atom quantum bits at a distance*, *Nat. Phys.* **3**, 538 (2007).
- [82] U. Eichmann, J. C. Bergquist, J. J. Bollinger, J. M. Gilligan, W. M. Itano, D. J. Wineland, and M. G. Raizen, *Young's Interference Experiment with Light Scattered from Two Atoms*, *Phys. Rev. Lett* **70**, 2359 (1993).
- [83] D. N. Matsukevich, P. Maunz, D. L. Moehring, S. Olmschenk and C. Monroe, *Bell inequality violation with two remote atomic qubits*, *Phys. Rev. Lett.* **100**, 150404 (2008).
- [84] B. B. Blinov, D.L. Moehring, L.-M. Duan, and C. Monroe, *Observation of entanglement between a single trapped atom and a single photon*, *Nature* **428**, 153 (2004).
- [85] X.-L. Feng, Z.-M. Zhang, X.-D. Li, S.-Q. Gong, and Z.-Z. Xu, *Entangling distant atoms by interference of polarized photons*, *Phys. Rev. Lett.* **90**, 217902 (2003).
- [86] L.-M. Duan, H. J. Kimble, *Efficient engineering of multiatom entanglement through single-photon detections*, *Phys. Rev. Lett.* **90**, 253601 (2003).
- [87] S. Gerber, D. Rotter, M. Hennrich, R. Blatt, F. Rohde, C. Schuck, M. Al-mendros, R. Gehr, F. Dubin, J. Eschner, *Quantum interference from remotely trapped ions*, *New. J. Phys.* **11**, 013032 (2009).
- [88] F. Rohde, *Remote ion traps for quantum networking: Two-photon interference and correlations*, Ph.D Thesis, ICFO Barcelona (2009).
- [89] U. Leonhard, *Measuring the quantum state of light*, Cambridge University Press, Cambridge (1997).
- [90] Z. Y. Ou and L. Mandel, *Relation between input and output states for a beam splitter*, *Optics Comm.* **63**, 118 (1987).
- [91] W. Vogel, *Squeezing and anomalous moments in resonance fluorescence*, *Phys. Rev. Lett.* **67**, 2450 (1991).
- [92] G. T. Foster, W. P. Smith, J. E. Reiner, and L. A. Orozco, *Time-dependent electric field fluctuations at the subphoton level*, *Phys. Rev. A*, **66**, 033807 (2002).

- [93] E. R. Marquina-Cruz and H. M. Castro-Beltran, *Nonclassicality of resonance fluorescence via amplitude-intensity correlations*, Laser Physics **18**, 157 (2008).
- [94] S. Gerber, D. Rotter, L. Slodicka, J. Eschner, H. J. Carmichael, and R. Blatt, *Intensity-Field Correlation of Single-Atom Resonance Fluorescence*, Phys. Rev. Lett. **102**, 183601 (2009).
- [95] Ch. Raab, J. Bolle, H. Oberst, J. Eschner, F. Schmidt-Kaler, and R. Blatt, *Diode laser spectrometer at 493 nm for single trapped Ba⁺ ions*, Appl. Phys. B **67**, 683 (1998).
- [96] P. Bushev, A. Wilson, J. Eschner, Ch. Raab, F. Schmidt-Kaler, Ch. Becher, and R. Blatt, *Forces between a single atom and its distant mirror image*, Phys. Rev. Lett. **92**, 223602 (2004).
- [97] U. Dorner and P. Zoller, *Laser-driven atoms in half-cavities*, Phys. Rev. A **66**, 023816 (2002).
- [98] L. Mandel, *Squeezed States and Sub-Poissonian Photon Statistics*, Phys. Rev. Lett. **49**, 136 (1982).
- [99] M. A. Wilson, P. Bushev, J. Eschner, F. Schmidt-Kaler, C. Becher, U. Dorner, and R. Blatt, *Vacuum-Field Level Shifts in a Single Trapped Ion Mediated by a Single Distant Mirror*, Phys. Rev. Lett. **91**, 213602 (2003).
- [100] F. Dubin, D. Rotter, M. Mukherjee, C. Russo, J. Eschner, and R. Blatt, *Photon correlation versus interference of single-atom fluorescence in a half-cavity.*, Phys. Rev. Lett. **98**, 183003 (2007).
- [101] V. Steixner, P. Rabl, and P. Zoller, *Quantum feedback cooling of a single trapped ion in front of a mirror*, Phys. Rev. A **72**, 043826 (2005).
- [102] Ch. Raab, J. Eschner, J. Bolle, H. Oberst, F. Schmidt-Kaler, R. Blatt, *Motional sidebands and direct measurement of the cooling rate in the resonance fluorescence of a single trapped ion*, Phys. Rev. Lett. **85**, 538 (2000).
- [103] M. Lindberg, *Resonance fluorescence of a laser-cooled trapped ion in the Lamb-Dicke limit*, Phys. Rev. A **34**, 3178 (1986).
- [104] S. Rist, J. Eschner, M. Hennrich, and G. Morigi, *Photon-mediated interaction between two distant atoms*, Phys. Rev. A **78**, 013808 (2008).
- [105] A. W. Glaetzle, K. Hammerer, A. J. Daley, R. Blatt, and P. Zoller, *A single trapped atom in front of an oscillating mirror*, Opt. Comm. **283**, 758 (2010).

- [106] D. F. Walls and P. Zoller, *Reduced Quantum Fluctuations in Resonance Fluorescence*, Phys. Rev. Lett. **47**, 709 (1981).

An dieser Stelle möchte ich mich bei allen Personen bedanken, die zum Gelingen dieser Dissertation beigetragen haben. Zu allererst gilt ein großes Dankeschön Rainer Blatt für die Möglichkeit in seiner Arbeitsgruppe mit einem hohen Maß an Entscheidungsfreiheit an sehr interessanten und spannenden Themenstellungen zu arbeiten. Die hervorragenden wissenschaftlichen und finanziellen Ressourcen seiner Gruppe boten ein ideales Umfeld für einen Experimentalphysiker.

Weiters möchte ich mich bei allen Mitgliedern der Arbeitsgruppe bedanken, ohne deren Zusammenarbeit und Gespräche solche Experimente nicht möglich gewesen wären. Besondern Dank gebührt dabei den Kollegen rund ums Barium-Projekt: Daniel Rotter, François Dubin, Manas Mukherjee, Lukas Slodička und Gabriel Hëtet für die tolle Teamarbeit, das große Engagement und die freundschaftliche Atmosphäre im Labor.

Vor allem möchte ich mich bei Markus Hennrich bedanken für die zahlreichen Diskussionen bei der Auswertung von Messungen sowie für seine Unterstützung beim Verfassen dieser Arbeit. Jürgen Eschner und Howard Carmichael danke ich für die großartige Unterstützung auf Seiten der Theorie und für die vielen Diskussionen, die zum Zustandekommen dieser Arbeit beigetragen haben.

Ebenfalls bedanke ich mich bei Patricia Moser und Karin Köhle für ihre Hilfe bei der Abwicklung von Formalitäten, sowie bei sämtlichen Mitarbeiterinnen und Mitarbeitern der Mechanik- und Elektronikwerkstätten und der IT-Verwaltung.

Zu guter Letzt möchte ich mich bei meiner wunderbaren Familie für die ständige Unterstützung während meiner Promotionszeit bedanken, sowie ganz besonders bei meiner lieben Jade für die glückliche Zeit in Innsbruck und auf Reisen.

Vielen Dank!